

DISS. ETH NO. 24560

Connecting the Dots
*tensor network algorithms for two-dimensional
strongly-correlated systems*

A thesis submitted to attain the degree of
DOCTOR OF SCIENCES of ETH ZURICH
(Dr. sc. ETH Zurich)

presented by

JUAN CAMILO OSORIO IREGUI

MSc. Physics, ETH Zurich

born on 14.02.1985

citizen of
Colombia

accepted on the recommendation of
Prof. Dr. Matthias Troyer, examiner
Prof. Dr. Philippe R. Corboz, co-examiner

2017

Juan Camilo Osorio Iregui

Connecting the Dots: tensor network algorithms for two-dimensional strongly-correlated systems

Diss. ETH No. 24560

E-mail osorio@itp.phys.ethz.ch

Contents

Abstract	v
Zusammenfassung	vii
1 Introduction	1
2 A prelude on notation	5
2.1 Conventions	6
2.2 Examples	7
3 Renormalization of classical partition functions	9
3.1 Partition functions	9
3.2 Mapping to a tensor network	10
3.3 Contraction schemes	12
3.3.1 Corner transfer matrix (CTM)	12
3.3.2 Tensor renormalization group (TRG)	13
3.3.3 Tensor network renormalization (TNR)	15
3.4 TNR characterization of the Blume-Capel model	17
3.4.1 Phase diagram	18
3.4.2 Conformal data	20
3.5 Discussion	26
4 Tensor network algorithms for quantum many-body systems	29
4.1 An entanglement-based approach	30
4.2 Matrix product states (MPS)	32
4.2.1 Definition	32
4.2.2 Some key properties	33
4.2.3 Matrix product operators (MPO)	36
4.2.4 The density matrix renormalization group (DMRG)	37
4.3 Projected entangled-pair states (PEPS)	40
4.3.1 Definition	40
4.3.2 Some key properties	41
4.3.3 Projected entangled-pair operators (PEPO)	44

4.3.4	Contraction schemes	45
4.3.5	Imaginary-time evolution	48
4.3.6	Variational optimization	51
4.4	Multi-scale entanglement renormalization Ansatz (MERA)	52
4.5	Conserved quantum numbers	53
4.6	Fermionic systems	55
4.6.1	Matrix product states	55
4.6.2	Higher-dimensional tensor networks	57
5	iPEPS study of the Kitaev-Heisenberg model	59
5.1	Kitaev’s honeycomb model	60
5.1.1	Exact Results	61
5.1.2	iPEPS Benchmarks	62
5.2	Kitaev-Heisenberg model	65
5.2.1	Previous work	65
5.2.2	iPEPS approach	66
5.2.3	Results	67
5.3	Discussion	73
6	Infinite projected entangled-pair states on cylinders	75
6.1	Previous work	77
6.2	Contraction schemes	78
6.2.1	Width-reduction scheme	79
6.2.2	OBC-MPS scheme	79
6.2.3	Local PBC-MPS schemes	80
6.2.4	Global PBC-MPS scheme	82
6.3	Benchmarks	82
6.3.1	Transverse field Ising model	82
6.4	iMPS vs iPEPS comparison	88
6.4.1	Heisenberg model	89
6.4.2	Hubbard model	92
6.5	Discussion	95
7	Conclusions & Outlook	97
A	Supplementary material for chapter 6	99
A.1	Diagrams for the construction of projectors P_b and P_t	99
A.2	Loop Quantum Monte Carlo Simulations of the Heisenberg Model	99
A.3	iPEPS Simulations	101
A.4	iMPS Simulations	103
	Acknowledgements	119
	Curriculum Vitae	121

Abstract

Tensor network algorithms (TNAs) represent one of the most recent developments in the field of numerical methods for the simulation of *strongly-correlated many-body* systems. Arising as a natural consequence of an improved understanding of the entanglement structures intrinsic to the ground-state manifolds of many-body Hilbert spaces, they correspond to algorithms exploiting entropic constraints expected to arise in various classes of many-body ground states.

In this work we apply and develop TNAs for the simulation of various strongly-correlated lattice models.

Concretely, we apply *tensor network renormalization* (TNR) to the study of the classical *Blume-Capel model* (BCM). We propose to exploit the RG features specific to TNR to obtain an indicator for the vicinity of (multi-)critical points. We show that in the case of the BCM it leads to a location of its tricritical point matching the accuracy of state-of-the-art Monte Carlo approaches. This allows us to characterize the underlying $c = 7/10$ conformal field theory with an excellent accuracy.

We then present a self-contained introduction to the most widely used techniques for the simulation of one- and two-dimensional quantum systems, where we cover *matrix product states* (MPS) and *projected entangled-pair states* (PEPS) in detail. We briefly discuss the *multi-scale entanglement renormalization Ansatz* (MERA).

We apply *infinite* PEPS (iPEPS) to the simulation of the *Kitaev-Heisenberg* (KH) model, proposed as an effective low-energy theory for the so-called *Iridate* compounds of the form $A_2\text{IrO}_3$ ($A = \text{Na}, \text{Li}$). We show the ability of iPEPS to accurately encode the complex ground-state physics of Kitaev's honeycomb model. When considering the KH model we confirm the existence of all previously found phases, locate all phase transitions in the phase diagram, finding good agreement with previous studies, and provide estimates for the survival regions of the spin-liquid phases in the thermodynamic limit. We briefly discuss the nature of these transitions.

We conclude this work with a study of various formulations of iPEPS on cylindrical geometries. We benchmark the proposed formulations by studying the transverse-field Ising model and find good performance for a subset of the formulations stud-

ied. We then carry out a comparison between iPEPS and iMPS methods for the Heisenberg and Hubbard models and find a range of cylinder widths over which both methods exhibit comparable performance. We find evidence for the potential of iPEPS simulations on cylinders and argue that our findings provide support for future studies employing both MPS and PEPS methods in conjunction.

Zusammenfassung

Tensornetzwerkalgorithmen (TNAs) stellen eine der jüngsten Entwicklungen auf dem Gebiet der numerischen Methoden zur Simulation von *stark korrelierten Mehrkörpersystemen* dar. Als eine natürliche Konsequenz eines verbesserten Verständnisses der Verschränkungsstrukturen, die den Grundzustandsräumen von Mehrkörper-Hilbert-Räume innewohnen, entsprechen sie Algorithmen, die entropische Beschränkungen ausnutzen, die in verschiedenen Klassen von Mehrkörper-grundzuständen erwartet werden.

In dieser Arbeit verwenden und entwickeln wir TNAs für die Simulation verschiedener, stark korrelierter Gittermodelle.

Wir wenden die *tensor network renormalization* (TNR) auf die Forschung des klassischen *Blume-Capel-Modells* (BCM) an. Wir schlagen vor, die für TNR spezifischen RG-eigenschaften zu nutzen, um einen Indikator für die Nähe von (multi-)kritischen Punkten zu bekommen. Damit zeigen wir, dass es im Falle des BCM zu einer Lokalisierung des trikritischen Punktes führt, der sich in seiner Genauigkeit *state-of-the-art* Monte-Carlo-methoden annähert. Dies ermöglicht uns, die zugrunde liegende $c = 7/10$ konforme Feldtheorie mit einer exzellenten Genauigkeit zu charakterisieren.

Wir stellen dann eine eigenständige Einführung in die am weitesten verbreiteten Techniken für die Simulation von ein- und zweidimensionalen Quantensystemen vor, in denen wir im Detail auf *matrix product states* (MPS) und *projected entangled-pair states* (PEPS) eingehen. Wir diskutieren kurz den *multi-scale entanglement renormalization Ansatz* (MERA).

Wir wenden *infinite* PEPS (iPEPS) auf die Simulation des *Kitaev-Heisenberg-Modells* (KHM) an, das als effektive Niedrigenergie-Theorie für die sogenannten *Iridaten* der Form $A_2\text{IrO}_3$ ($A = \text{Na, Li}$) vorgeschlagen wurde. Wir zeigen die Fähigkeit von iPEPS, die komplexe Grundzustandsphysik des Kitaev Modells genau zu representieren. Bei der Betrachtung des KHM bestätigen wir die Existenz aller bisher gefundenen Phasen, lokalisieren alle Phasenübergänge im Phasendiagramm und liefern Schätzungen für die Überlebensregionen der Spinflüssigkeitsphasen im thermodynamische Grenzfall. Wir diskutieren kurz die Natur dieser Übergänge.

Wir schlieSSen diese Arbeit mit einer Untersuchung verschiedener Formulierungen von iPEPS für zylindrische Geometrien ab. Wir bewerten die vorgeschlagenen Formulierungen durch die Untersuchung des Ising-Modells im transversalen Feld und finden gute Ergebnisse für eine Teilmenge der untersuchten Formulierungen. Wir führen dann einen Vergleich zwischen iPEPS und iMPS Methoden für die Heisenberg und Hubbard Modelle durch und finden einen Bereich von Zylinderbreiten, in dem beide Methoden vergleichbare Leistungen bringen. Wir finden Beweise für das Potenzial von iPEPS-Simulationen auf Zylinder und argumentieren, dass unsere Erkenntnisse Unterstützung für zukünftige Studien liefern, die sowohl MPS- als auch PEPS-Methoden zusammen verwenden.

Chapter 1

Introduction

One of the greatest challenges faced by modern science pertains the understanding of so-called *strongly-correlated many-body* systems, *i.e.*, the class of systems made up of extensively many constituents in regimes in which the interactions between them are by no means negligible. As their name suggests the reliable treatment of such systems generically precludes an understanding based solely on information related to its constituents in isolation or minor modifications thereof. As P. W. Anderson craftfully described it, these are systems for which truly *more is different* [1].

A few of the most notorious examples include systems close to *criticality*, in which correlations spread over all length scales in the system, *quantum spin-liquid* phases, in which *quantum fluctuations* preclude the formation of long-range order, even as the system is brought to absolute zero temperature, or high-temperature superconductors, like, *e.g.*, the so-called *cuprates*, in which the superconducting state survives at temperatures far higher than expected within a BCS [2] picture.

For critical systems the presence of a diverging correlation length is nothing more than a reflection of their *scale invariance* in which microscopic quantities, like, *e.g.*, the lattice constant, become *irrelevant* features and so-called *conformal symmetry* typically emerges. For these systems the concept of a *universality class* appears as a direct consequence of their scale invariance, allowing for a very elegant classification in terms of little more than a few properties like the dimensionality of space and global symmetries [3, 4]. Even more, the emergence of conformal symmetry in two-dimensional systems brings about an incredibly rich structure for critical partition functions allowing them to be organized into so-called *conformal blocks* and enabling the exact computation of critical exponents and multi-point correlation functions [5, 6]. In practice, however, the precise characterization of a theory's critical properties is far from being a straightforward matter and, even with the aid of elaborate theoretical tools, such as the *renormalization group* (RG) of Kadanoff and Wilson [7–9], questions remain.

Originally proposed by Anderson as the ground state of a Heisenberg antiferromagnet on the triangular lattice [10], the quantum spin liquid (QSL) provides one of the most peculiar specimens in the zoo of exotic phases arising in strongly-interacting systems. Unlike in a conventional magnet and as a consequence of strongly frustrated interactions, *quantum fluctuations* in a QSL phase are so strong that, even as the system is driven to zero temperature, the only clear feature of the system is its complete lack of features [11–13]! In other words, the system may not be characterized in terms of a *local* order parameter, as typically done within the usual paradigm of Landau theory [14, 15]. These phases have attracted significant interest as they are known to host *fractionalized* excitations obeying *anyonic* statistics, making them a very attractive framework for the implementation of so-called *topological quantum computing* [16, 17]. Among the various candidate materials for hosting a QSL phase, the family of *Iridate* compounds has recently received particular attention owing to their potential for hosting spin-liquid phases arising in a paradigmatic model proposed by Kitaev [18]. Even though all the basic ingredients required to realize Kitaev’s spin liquid appear to be available, the precise conditions under which this might happen are still unknown and so the search for the elusive phase continues.

The potential applications for superconducting materials operating at room temperature are innumerable and thus high-temperature superconductivity embodies one of the most exciting problems in modern condensed-matter physics. However, a thorough understanding of the mechanism stabilizing superconductivity at unusually large temperatures remains a major challenge [19, 20]. Interestingly, the relevant degrees of freedom in the cuprates, given by copper orbitals living in CuO_2 square lattice planes inside a complex lattice structure, can be described by a low-energy effective theory known as the (single-band) *Hubbard model* [21], *i.e.*, the simplest lattice model describing electrons in a crystal subject to their mutual Coulomb repulsion. This model is, indeed, known to exhibit some of the basic qualitative features present in the phase diagram of the cuprates, however, and in spite of its deceiving simplicity, reaching a consensus on the nature of the ground state in the so-called *underdoped* regime has required titanic efforts which only until recently, and employing a combination of several state-of-the-art techniques, appear to have converged on a ground state exhibiting stripe order [22, 23].

Despite the considerable progress made towards the understanding of strongly-correlated systems, much work remains to be done and, as is perhaps to be expected, the broad nature of the problems encountered means that no single approach is likely to be applicable in every circumstance.

From a numerical perspective a wide variety of techniques have been developed over time. Of these, the most accurate is *exact diagonalization* (ED) which, as its name indicates, attempts to partially diagonalize the Hamiltonian operator. However, owing to the exponential growth of Hilbert space dimension as the system size is increased, this method rapidly becomes inapplicable. Indeed, even when targeting

the ground-state manifold, this method is typically constrained to systems of no more than 30-50 particles and is often known to suffer from significant finite-size corrections.

Series expansions methods correspond to the evaluation of observables in terms of an expansion in powers of some perturbation parameters. Even though these methods are extremely reliable at high temperatures or close to expansion points where the expected phase is simple to represent, the radius of convergence for the series is usually quite limited. In order to overcome this limitation, an analytic continuation in terms of Padé approximants is often used and thus one is forced to introduce uncontrolled approximations. Also, owing to their perturbative nature, studying systems close to criticality becomes challenging [24].

Quantum Monte Carlo (QMC) methods correspond to a class of algorithms in which a stochastic sampling is employed in order to obtain statistical estimates for observables of interest. Among the most widely used techniques are *diagrammatic* QMC, in which a sampling over Feynman diagrams of certain orders and topologies is carried out directly in the thermodynamic limit [25–27], or *determinantal* QMC, in which the introduction of auxiliary fields allows to decompose density-density interactions into non-interacting terms [28–32]. Whenever applicable, QMC methods are known to be among the most reliable approaches, however, notable limitations do arise. For example, in diagrammatic QMC the introduction of uncontrolled approximations is typically necessary and, similar to series expansions above, the study of critical systems can be significantly hampered. In the case of determinantal QMC the appearance of weights of varying sign in the partition sum gives rise to the so-called *sign problem*, in which the noise-to-signal ratio grows exponentially fast with the system size and temperature [33]. Since this sign problem often arises in systems with fermionic degrees of freedom or frustrated spin interactions the method is of limited applicability in these very interesting cases.

More recently, a new avenue on the path towards the understanding of strongly-correlated systems emerged with the advent of *quantum information theory* (QIT). By providing insights into the subtle entanglement structures present in the ground states of local Hamiltonians, it has enabled important progress towards taming the exponential complexity of the many-body Hilbert space, *i.e.*, by driving the discovery of so-called *area laws* for entanglement entropy, it has made it clear that, in a large class of problems, it is only a zero-measure subspace of the exponentially growing Hilbert space which is relevant for the search of ground-state physics [34–36].

The class of algorithms exploiting this new understanding of ground-state entanglement is generically referred to as *tensor network algorithms* (TNAs). Their basic idea is to employ a tensor decomposition of the many-body wave function in order to design Ansätze exhibiting well-defined entanglement properties. Some of the most notorious examples go under the name of *matrix product states* (MPS) [37–40] and *projected entangled-pair states* (PEPS) [41–44] and correspond to wave

functions obeying so-called *area laws* for entanglement entropy. These *Ansätze* are designed to provide *efficient* and *variational* representations of ground states for gapped and local Hamiltonians.

Rather surprisingly, TNAs have also been employed for the development of tools suitable for the study of systems at criticality, where one of the best-known examples receives the name of *multi-scale entanglement renormalization Ansatz* (MERA) and is designed to encode the logarithmic corrections to the area law arising in critical one-dimensional systems [45–48].

Importantly, the class of TNAs represents one in which *controlled* approximations are employed and thus, by introducing a quantity known as the *bond dimension*, a handle with which to systematically improve the accuracy of the algorithms is effectively obtained.

Even though these are all interesting properties making TNAs very appealing, as we shall elaborate below, the numerical implementation of some of these algorithms can bring about important challenges and so we shall also discuss these in detail.

In what follows it will be our focus not only to present a self-contained introduction to various methods within the class of TNAs, but also to explore the physics of a number of strongly-correlated systems. Along the way we shall probe the accuracy and reliability with which the methods may be employed as well as present proposals for extending their range of applicability.

We shall begin our discussion in Ch. 2 by providing an introduction to the graphical notation employed in the field of TNAs. In Ch. 3 we will illustrate how partition functions of classical lattice models may be brought into a form reflecting an underlying tensor network structure, thus making them amenable to a TNA treatment. There we shall present a few of the techniques employed for their evaluation and apply one of the most recently developed, known as *tensor network renormalization*, to characterize the classical *Blume-Capel model* on the square lattice. In Ch. 4, we shall present a self-contained introduction to the most important techniques for the simulations of quantum systems in one and two dimensions. There we shall introduce *matrix product states* (MPS), *projected entangled-pair states* (PEPS) as well as the *multi-scale entanglement renormalization Ansatz* (MERA). Chapter 5 presents an application of infinite PEPS to the simulation of a frustrated spin model known as the *Kitaev-Heisenberg* model, recently proposed as an effective description of the low energy degrees of freedom in the so-called *iridate* compounds. Finally, in Ch. 6 we study extensions of the PEPS algorithms to cylindrical geometries and evaluate their performance by considering the transverse-field Ising, Heisenberg and Hubbard models on the square lattice.

Chapter 2

A prelude on notation

A recurrent issue in the field of tensor network algorithms is the appearance of expressions, later referred to simply as *tensor networks*, in which an unmanageably large number of indices arise.

To illustrate the issue, consider the following expression

$$O = \sum_{\{m_i, n_i, s_i, s'_i\}} A_{s_1}^{[1]m_1} O_{s_1 s'_1}^{[1]n_1} A_{s'_1}^{[1]*m'_1} A_{s_2}^{[2]m_1 m_2} O_{s_2 s'_2}^{[2]n_1 n_2} A_{s'_2}^{[2]*m'_1 m'_2} \\ A_{s_3}^{[3]m_2 m_3} O_{s_3 s'_3}^{[3]n_2 n_3} A_{s'_3}^{[3]*m'_2 m'_3} A_{s_4}^{[4]m_3} O_{s_4 s'_4}^{[4]n_3} A_{s'_4}^{[4]*m'_3}. \quad (2.1)$$

A very unnerving one to write, not to mention the huge potential for error in the proper assignment of indices as well as the intrinsic staleness of a long unintuitive equation. It turns out, as we shall explain later, that this expression corresponds to the evaluation of an observable using a so-called *matrix product state* representation on a system of 4 sites. Not precisely the system size we will be aiming at in practice!

In order to avoid this problem, we shall begin by introducing a very practical graphical notation which is widely used in the field of tensor network algorithms. This notation will allow us to represent rather complex mathematical expressions in a very neat and intuitive way.

2.1 Conventions

Since the core of our work will be concerned with mathematical expression involving various objects like: vectors, matrices or, more generally, arbitrary rank tensors as well as the summation of numerous indices, one may develop a simple set of rules building up a mapping that leads to graphical expressions which are quite easy to read.¹ We will summarize the notation using the following set of rules:

- I) Arbitrary rank tensors shall be represented by circles or squares. Which one is chosen depends largely on the context.
- II) Indices attached to any object are represented by lines. If the line style is to be understood as denoting a specific type of index, this shall be mentioned explicitly.
- III) Summation over indices shared by any two objects is indicated by a line joining both objects.
- IV) Outer products between tensors are represented by adjacent tensors with no lines joining them. Additional visual aid, *e.g.*, shading, may be provided to emphasize this structure.

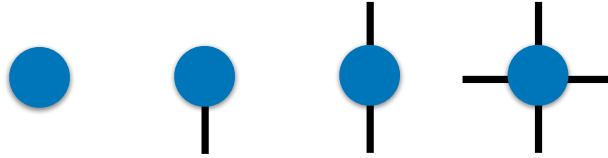


Figure 2.1: Examples illustrating the notation used for tensor network simulations. Left most: a scalar, left-center: a vector, right-center: a matrix, right most: a rank-4 tensor.

As with any set of rules, a corresponding set of exceptions entail:

- E-I)** The identity operator shall be represented simply by continuous lines.
- E-II)** Tensors satisfying an isometric constraint (or an inverse relation), *e.g.*, isometric matrices satisfying either AA^\dagger or $A^\dagger A$, shall be represented by triangles.

¹Even though there is, to this date, no standard making these conventions precise, they are very widely spread so the reader will be able to use them when dealing with most works on tensor network algorithms.

2.2 Examples

In order to get a better feeling for how the notation works, let us consider a few simple applications. Figure 2.1, shows a few examples for low-rank objects. In Fig. 2.2 we show the tensor network corresponding to the trace over a product of three matrices, where as in Fig. 2.3 we illustrate how one may obtain a rank-1 tensor, *i.e.*, a vector, by contracting common indices on a couple of matrices and a rank-3 tensor.

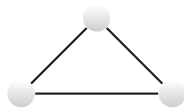


Figure 2.2: Graphical notation for the trace over the product of 3 matrices.

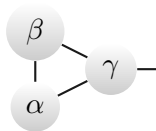


Figure 2.3: Graphical notation for the contraction of common indices on rank-2 (α, β) and rank-3 (γ) tensors into a rank-1 tensor, *i.e.*, a vector.

Finally, with these rules in place we may now recast the evaluation in Eq. (2.1) into the simple, yet elegant, form of Fig. 2.4.

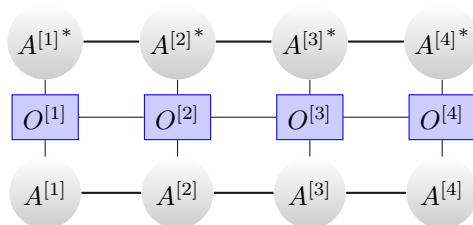


Figure 2.4: Tensor network corresponding to the evaluation of an observable on a four site system using matrix product state and matrix product operator representations of the state and operator, respectively.

Even though these rules cover the basic notions required to understand most works, depending on the context it might also be assumed that tensors of the same shape reflected about some axis, *e.g.*, the horizontal axis, correspond to complex conjugates of each other. Had we chosen to use this convention all complex conjugation symbols in Fig. 2.4 could have been simply removed.

2.2 Examples

We hope that these examples have made it clear how the graphical notation allows for a very systematic scaling up of the complexity of expressions, while preserving readability by remaining very intuitive. We shall make extensive use of it in the remainder of this work.

Chapter 3

Renormalization of classical partition functions

In order to begin our discussion on tensor networks we shall start off with a relatively simple scenario in which they arise quite naturally, *i.e.*, in the computation of partition functions of classical lattice models.

In this chapter we shall also introduce the concept of a *contraction scheme*, a notion which will play a central role in the simulation of quantum systems, as we shall see later on. We begin by introducing contraction schemes in the classical setting because this will allow us to highlight the key components of each scheme in a very transparent way. In order to illustrate the accuracy achievable by means of such contraction schemes we shall close the chapter with a study of the so-called *Blume-Capel model*, where we will see how it is possible to obtain results matching the accuracy of state-of-the-art Monte Carlo studies while at the same time providing a comprehensive characterization of its critical properties.

3.1 Partition functions

To begin the discussion let us briefly recall some basic concepts of statistical mechanics. For the sake of simplicity we shall constrain the discussion to spin systems in a canonical ensemble exhibiting only nearest-neighbor interactions. Extensions to more generic settings can be achieved employing minor modifications.

Consider a system described by the Hamiltonian

$$H = \sum_{\langle i,j \rangle} h_{i,j} + \sum_i h_i, \quad (3.1)$$

where $\langle i,j \rangle$ stands for a summation over the links of a graph \mathcal{G} , $h_{i,j}$ interaction terms coupling the spins at neighboring sites, and on-site terms h_i . To obtain a

3.2 Mapping to a tensor network

description of the statistical properties of such a system one defines the *partition function*

$$Z = \sum_{\{S_i\}} \exp(-\beta H[\{S_i\}]), \quad (3.2)$$

where the sum runs over all spin configurations and $\beta = 1/k_B T$, with k_B Boltzmann's constant and T the temperature. The partition function of a system plays a central role in its statistical description as most relevant physical quantities may be obtained from it. For example the internal energy may be obtained simply as

$$U := \langle E \rangle = -\frac{\partial \log Z}{\partial \beta}, \quad (3.3)$$

whereas the Helmholtz free energy may be computed as

$$F = -\frac{1}{\beta} \log Z, \quad (3.4)$$

and correlators may be computed by introducing infinitesimal fields at different locations and then differentiating with respect to these fields.

Below we shall present an approach in which by exploiting the underlying tensor network structure of partition functions, and performing a *controlled* approximation, one gains access to numerous quantities of interest.

3.2 Mapping to a tensor network

From now on let us focus on the case where \mathcal{G} corresponds to a square lattice, since any other case follows in a straightforward way. There are a number of different ways in which one may make the tensor network structure arising in a partition function Z explicit. One of these proceeds by defining the rank-4¹ tensor $A^{[i]}$ with entries

$$A_{\tilde{s}_l \tilde{s}_b \tilde{s}_r \tilde{s}_t}^{[i]} = \sum_s \left(\mathcal{S}_{s,s}^{[i]} \prod_{j=\{l,b,r,t\}} \sqrt{\mathcal{B}^{[i,j]}_{s\tilde{s}_j}} \right) \quad (3.5)$$

with j running over the left, bottom, right and top neighbors of site i , respectively, and in terms of the matrices $\mathcal{B}^{[i,j]}$ and $\mathcal{S}^{[i]}$ defined as

¹The rank of the tensor will in general be given by the number of neighboring sites, *i.e.*, by the coordination number in the case of regular lattices.

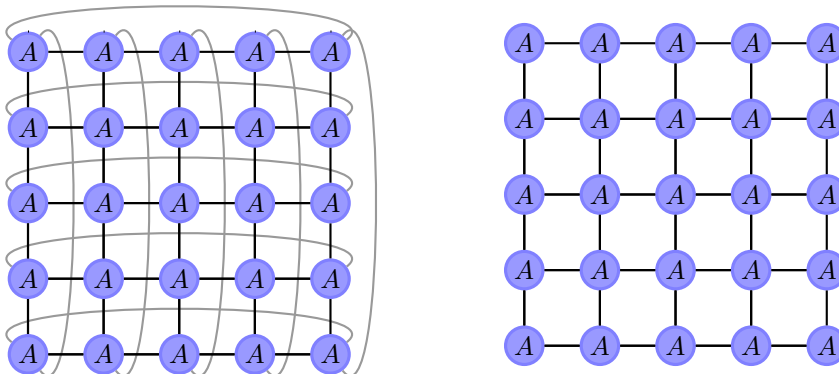


Figure 3.1: Tensor networks representing partition functions of systems on 5x5 lattices with (left) and without (right) periodic boundary conditions.

$$\mathcal{B}_{s,s'}^{[i,j]} = e^{-\beta h_{i,j}(s,s')} \quad (3.6)$$

$$\mathcal{S}_{s,s'}^{[i]} = e^{-\beta h_i(s)} \delta_{s,s'}. \quad (3.7)$$

The partition function Z may then be reformulated in terms of the tensors $A^{[i]}$ as

$$Z = tTr[A^{[1]}A^{[2]} \dots A^{[N_x*N_y]}], \quad (3.8)$$

with $N_{x(y)}$ the linear system sizes and tTr representing the so-called *tensor trace*, *i.e.*, a summation over all indices corresponding to the tensors in the set $\{A^{[i]}\}$. Thus a partition function may be generically expressed as the tensor networks in Fig. 3.1.

The exact evaluation of this expression is, rather unsurprisingly, seldom possible in practice. In fact, by reformulating the computation of the partition function Z in terms of the tensor network in Fig. 3.1, it is not hard to convince oneself that its evaluation entails a computational cost growing exponentially fast with the smallest system dimension, *i.e.*, $\mathcal{O}((2S+1)^{\min(N_x, N_y)})$, for a spin- S system.

Thus, in order to reach system sizes representative of the thermodynamic limit one is forced to evaluate Eq. (3.8) in an approximate way. It is the precise formulation of this approximate evaluation what has been dubbed as a *contraction scheme*. As we shall show in the following chapter, this concept also plays a central role in the simulation of quantum systems.

3.3 Contraction schemes

As mentioned above the notion of a contraction scheme refers to a specific, possibly approximate, procedure with which to carry out the summation over tensor indices in Eq. (3.8). In practice most of these proposals correspond to heuristic procedures which are, at times, motivated by developments in the understanding of entanglement properties of quantum states or employ well-known data compression techniques, *e.g.*, principal component analysis as effected via the so-called singular value decomposition (SVD) or higher dimensional generalizations thereof [49–54].

Most (if not all) of these schemes are laid out by introducing a control parameter traditionally denoted by χ . As we will see, this control parameter can be generically understood as parametrizing the dimensionality of the configuration space over which the approximation is performed, so that by allowing it to become sufficiently large one eventually reaches the full dimensionality of the original problem, *i.e.*, all approximations involved are *controlled* in that they become exact in the asymptotic limit $\chi \rightarrow \infty$.

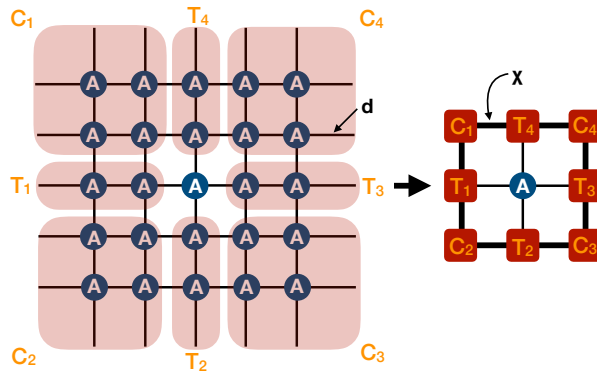


Figure 3.2: Description of unit cell environments employing environment tensors employed in the CTM scheme.

3.3.1 Corner transfer matrix (CTM)

The *corner transfer matrix* (CTM) scheme was introduced by Nishino and Okunishi in Refs. [49, 50] and later generalized by Orús and Vidal in Refs. [51, 52]. The algorithm acquires its name due to its close connection to Baxter’s corner transfer matrix construction for classical systems [55–57].

The algorithm proposed in the *directional* CTM approach from Ref. [51] proceeds by introducing effective environment tensors meant to describe, possibly infinite,

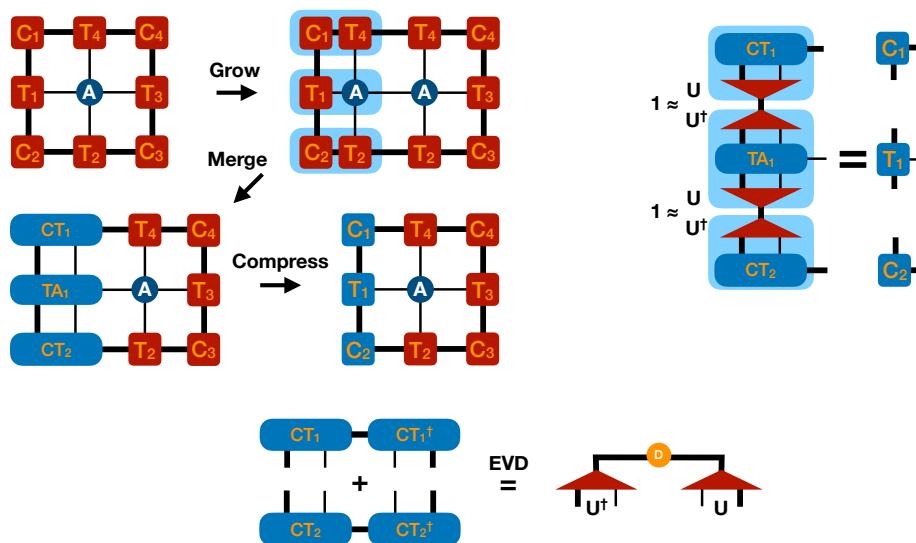


Figure 3.3: Top left: left CTM growing move. The procedure may be broken into 3 steps: in the first one the left boundary is grown, then the corresponding tensors are merged and finally the new combined tensors are compressed by inserting approximate resolutions of the identity on the auxiliary bonds. Top right: definition of new objects upon compression. Bottom: construction of the isometries U employed for the truncation of auxiliary bonds.

subportions of the system's unit cell environment, see Fig. 3.2. These environment tensors are grown by means of iterative absorption steps, in which one contracts a boundary tensor together with a bulk tensor describing the partition function. After each growing step one keeps the number of degrees of freedom within computational limits by inserting approximate resolutions of identity in between the grown tensors and keeping a maximum of χ basis states on their auxiliary indices, see Fig. 3.3. By repeating such moves along all directions of the system one may systematically approach the thermodynamic limit.

This algorithm may be formulated with a computational complexity scaling as $\mathcal{O}(d^2\chi^3)$, with d the dimension of the original tensors $A^{[i]}$.

3.3.2 Tensor renormalization group (TRG)

This approach was originally proposed by Levin and Nave in [53], and it is inspired in the density matrix renormalization group method that we shall encounter later on in Sec. 4.2.

The TRG scheme consists of a series of SVDs of the tensors in Eq. (3.5), see Fig. 3.4, and subsequent reconnection of the resulting objects in such a way that after each step a tensor network on a lattice dual to the original one is obtained. In carrying out this procedure the lattice size is reduced by a factor of 2 after every iteration, *i.e.*, the effective lattice size decreases exponentially fast with the number of coarse-graining iterations.² It is thus often possible to reach fixed points after only a few dozen iterations. In order to keep the computational cost under control a truncation of each SVD decomposition is performed at every step, where the largest χ singular values are kept. The precise sequence of operations proposed by Levin and Nave is summarized in Fig. 3.5.

The computational complexity of this method scales as $\mathcal{O}(\chi^6)$ for fixed χ , however, as discussed already in the original publication [53], in fixing χ one effectively introduces a cut-off in the correlation length which can be encoded. Thus to achieve a fixed level of accuracy as one grows the system at a critical point, the refinement parameter χ must be permanently increased. In other words, the algorithm does *not* provide a *sustainable* approach at criticality.

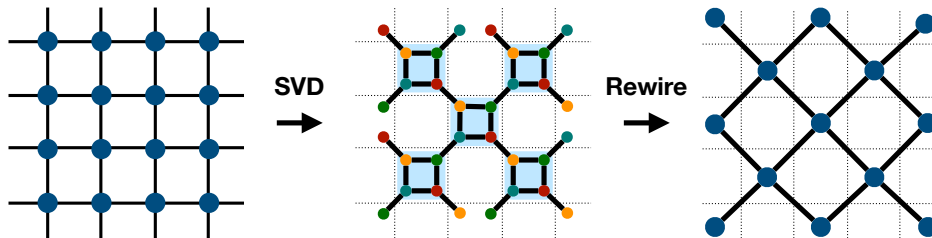


Figure 3.5: Sequence of operations defining the TRG contraction scheme proposed in [53]. After a step has been concluded one obtains a tensor network on the dual lattice with half the number of tensors.

In spite of their inability to provide efficient descriptions at criticality, both the CTM as well as the TRG algorithms are known to provide good accuracy for values of χ reachable without exceedingly large computational resources, *i.e.*, employing a personal computer, see Refs [53, 58] for more detailed discussions.

²As the method does not explicitly incorporate global information, one may just as well think of it as *growing* the lattice.

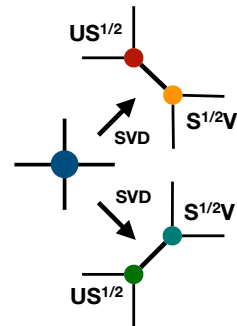


Figure 3.4: Two possible SVDs of the original tensor A . By performing an SVD, $A = USV$, and grouping into the objects $US^{1/2}$ and $S^{1/2}V$, one obtains two possible decompositions.

3.3.3 Tensor network renormalization (TNR)

One of the most recent developments in the field has been proposed by Evenbly and Vidal [59, 60] and goes under the name of *tensor network renormalization* (TNR). This is a contraction scheme inspired by the so-called *multi-scale entanglement renormalization Ansatz* [46–48, 61–63], a type of *Ansatz* state which is designed to encode wave functions of one-dimensional (1D) systems at criticality, *i.e.*, it efficiently encodes the amount of entanglement typical of 1D critical points, see Sec. 4.4.

A central point to this algorithm, as in the TRG above, is the notion of a *local replacement*, *i.e.*, the idea of introducing modifications to a network’s local motifs that, combined with some approximation, allows its coarse graining by employing a local cost function as a figure of merit.

In the case of the TRG above, the most straightforward approach is used in that employing the SVD provides an optimal reduced-rank approximation to the various matricizations of the original tensors A . In the TNR algorithm the notion of a *projective truncation* was introduced as a generalization of the SVD-based approximation [60]. The idea consists of performing a local replacement by taking a tensor motif N and attaching an isometric projector P to it, *i.e.*, $N \mapsto \tilde{N} = NP = Nww^\dagger$, with $P^2 = P$, see Fig. 3.6. Once this insertion has been carried out the cost function

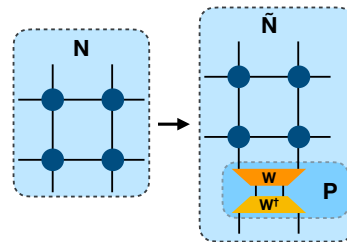


Figure 3.6: Example of a local replacement in terms of the insertion of a projector P .

$$\epsilon = \|N - \tilde{N}\| \quad (3.9)$$

is minimized while preserving the isometric character of w .

As Fig. 3.7 shows, this can be achieved by maximizing $\|\tilde{N}\|$ with respect to the isometry w , which in turn can be done via SVD of the tensor $\Gamma_w = USV$, see Fig. 3.7, and setting $w = V^\dagger U^\dagger$ which explicitly satisfies the isometric constraint in Fig. 3.7 (green box). TNR employs this idea to optimize the objects u , v , w in Fig. 3.8(e).

This is the only contraction scheme for which there is compelling evidence of it providing a *sustainable* approach at criticality, *i.e.*, one in which it is possible to achieve a fixed error as the algorithm coarse grains the system without indefinitely increasing the parameter χ . Furthermore, it is the only contraction scheme which appears to be capable of representing proper renormalization group (RG) trans-

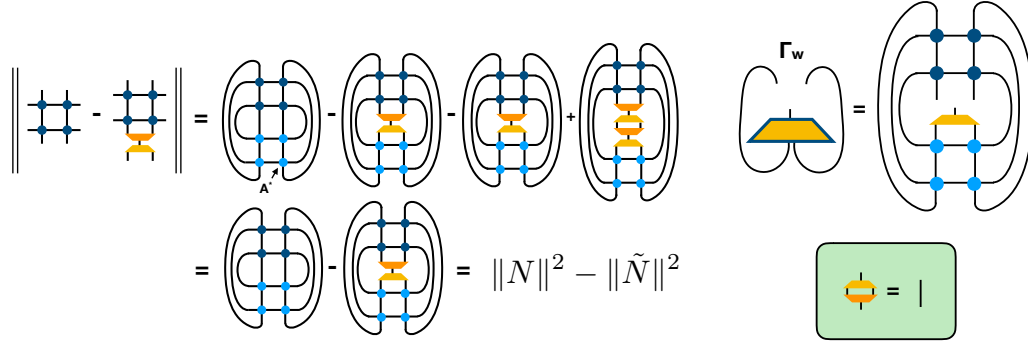


Figure 3.7: Left: cost function for the projective truncation approach. The isometric structure of the projector allows for a convenient cancellation of terms. The final expression shows that the end goal is to maximize $\|\tilde{N}\|$. Right top: definition of tensor Γ_w . Right bottom: isometric constraints imposed on w (yellow tensor), see Fig. 3.6. Light and blue tensors indicate complex conjugates of each other.

formations, making it a very interesting approach from a conceptual perspective. See [59, 60, 64] for a more detailed discussion. We shall exploit these features in the following section.

The algorithm is typically implemented introducing *two* control parameters χ and χ' , corresponding to the dimensions of the outer indices in Figs. 3.8(e) and 3.8(g), respectively. In practice a combination $\chi' \sim \chi$, with a prefactor 1.5-2, appears to work quite well. Using this set-up TNR can be implemented with a computational cost scaling as $\mathcal{O}(\chi^7)$, although additional controlled approximations may be employed to reduce this scaling to $\mathcal{O}(\chi^6)$ as in the TRG scheme, albeit at the expense of introducing an additional control parameter χ'' . In practice, even when employing the lower cost variant, the prefactors involved are found to be substantially larger than those in the TRG scheme, *i.e.*, of the order of 10^{2-3} .

From a purely numerical perspective TNR provides a very interesting alternative as it may achieve errors as low as $\Delta f \sim 10^{-7}$ at the *critical point* of the Ising model for

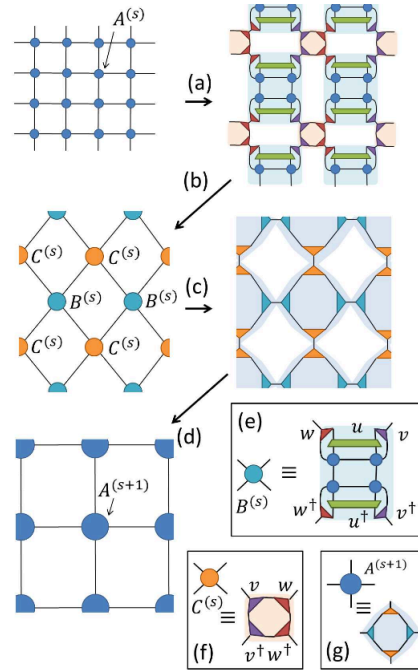


Figure 3.8: Summary of the TNR algorithm. Figure taken from Ref. [59].

a modest value of $\chi = 10$. This is an improvement of almost *two* orders of magnitude compared to TRG. Away from criticality the accuracy of the algorithms increases quite rapidly.

Additional developments of the algorithm have been discussed in Refs. [65, 66].

3.4 TNR characterization of the Blume-Capel model

Having presented a few of the possibilities proposed in the literature for obtaining approximate representations of classical partition functions, in this section we shall illustrate how, exploiting key properties of the TNR algorithm above, it is possible to combine all the information readily available in the tensor network language to obtain very accurate and comprehensive characterizations of classical spin models.

All results presented below represent original work carried out by the author, unless otherwise stated.

To illustrate the approach we shall focus on the so-called *Blume-Capel model*, *i.e.*, an extension of the classical two-dimensional (2D) Ising model on the square lattice in which non-localized, or *annealed*, vacancies are introduced.³ The model is defined by the Hamiltonian

$$H = -J \sum_{\langle i,j \rangle} \sigma_i \sigma_j + D \sum_i \sigma_i^2, \quad (3.10)$$

where $\langle i, j \rangle$ and i represent the bonds and sites of a square lattice and $\sigma \in \{-1, 0, 1\}$, with $\sigma = 0$ representing a vacancy. From now on we fix the coupling constant $J = 1$, so that the only remaining parameters are D and the temperature T . It is straightforward to verify that this model inherits the \mathbb{Z}_2 spin-flip symmetry, $\sigma \rightarrow -\sigma$, present in the Ising model. We assume periodic boundary conditions along both lattice axes throughout the entire discussion.

One may get an overall idea of the phase diagram by looking at the limiting cases $D \rightarrow \pm\infty$ and $T = 0$. Below we follow the discussion presented by Cardy in Ref. [4].

In Eq. (3.10) above the first term represents the typical Ising coupling between neighboring spins whereas the second term may be thought of as a chemical potential term for the vacancies. Indeed, in the limit of $D \rightarrow -\infty$ the presence of vacancies is completely suppressed and the system may be effectively described

³The Blume-Capel model is also interpreted as having degrees of freedom representing spin-1 Ising variables instead. In this context the model is then typically referred to as the *Tricritical Ising model*.

by the classical 2D Ising model where, according to temperature, one finds an ordered (ferromagnetic) phase separated from a disordered (paramagnetic) phase by a second-order phase transition. In the opposite case, *i.e.*, $D \rightarrow \infty$, the system is completely devoid of spins.

Going to the limit $T \rightarrow 0$ one finds (up to symmetry transformations) two types of possible ground states: the first one, owing to the ferromagnetic nature of the coupling, corresponds to ordered states with $\sigma_i = \pm 1, \forall i$, and an energy per site of $e = D - 2$; the second one, corresponding to a fully depleted system, has an energy per site $e = 0$. Which ground state is found depends then entirely on the value of D , where for $D > 2$ the ground state will be completely devoid of spins whereas in the opposite case $D < 2$ a fully polarized state is found. Thus, in this limit, we find a first-order phase transition separating an ordered phase from a depleted "disordered" phase.⁴ Since this first-order phase boundary should be found for a finite range of temperatures above $T = 0$, we find that somewhere in the phase diagram the line of first-order phase transitions *must* become a line of second-order phase transitions. The point at which this happens is a so-called *tricritical point*.⁵

Even though its existence can be deduced from basic renormalization group (RG) arguments [4], the actual location of the tricritical point cannot be found by exact means and there have been numerous numerical studies of this model with the goal of obtaining an accurate characterization [67–71]. Perhaps more interesting than the location of the tricritical point itself is the characterization of its critical properties which, by now, are known to be described by a conformal field theory (CFT) with a central charge $c = 7/10$.

In what follows we shall show how it is possible to employ the TNR algorithm to not only obtain a very accurate location of the tricritical point but also an essentially unambiguous identification of the underlying CFT.

3.4.1 Phase diagram

In order to obtain the relevant thermodynamic data for the characterization of the phase diagram we begin by obtaining accurate representations of its partition function at numerous locations (D, T) in parameter space. As explained in Sec. 3.1 when employing a tensor network approach we have direct access to approximations of the partition function and thus of the system's free energy density f . Via numerical differentiation we may readily extract quantities like the internal energy (u), the entropy (s) and the specific heat (c), see Fig. 3.9. These quantities provide a direct means of characterizing the phase diagram, *e.g.*, the peaks in c hint at the

⁴The first-order nature of this transition follows directly from the discontinuity in the first derivative of the energy as a function of D .

⁵The fact that this is indeed a tricritical point only becomes apparent under the inclusion of a magnetic field term $h \sum_i \sigma_i$ to the Hamiltonian where additional critical lines emerge.

existence of phase transitions between the ordered (low entropy) and disordered (high entropy) phases. Depending on the value of D these transitions appear to be of either first- or second-order type.

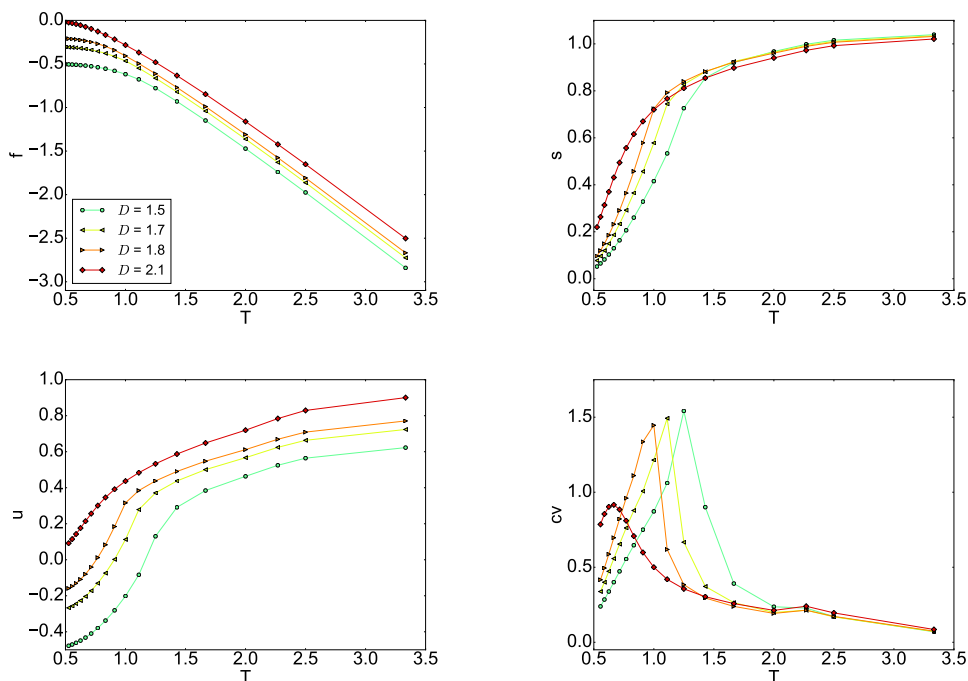


Figure 3.9: Thermodynamic data for the Blume-Capel model obtained using the TNR algorithm with a bond dimension $\chi = 6$. Top left: Helmholtz free energy, top right: entropy, bottom left: internal energy, bottom right: specific heat. The steep increase in the u and s curves together with peaks of the specific heat c hint at the existence of various phase transitions.

In Fig. 3.11 we show an overview of the phase diagram over a relatively wide parameter range which was obtained using this approach. As we illustrate in the inset once one approaches the location of the tricritical point enough it starts to become increasingly difficult to determine the precise nature, *i.e.*, first- vs second-order, of the phase transition by the evaluation of numerical derivatives. The reason being the complex interplay between all parameters in the simulation, *i.e.*, D , T , the discretization steps δD , δT as well as the bond dimension χ .

In practice not only will the location of a phase transition depend on the value of χ but also its precise nature. Indeed, as we illustrate in Fig. 3.10, what might appear to be a clear first-order phase transition at a small value of χ can evolve into a phase transition with an extremely weak discontinuity (potentially generated by

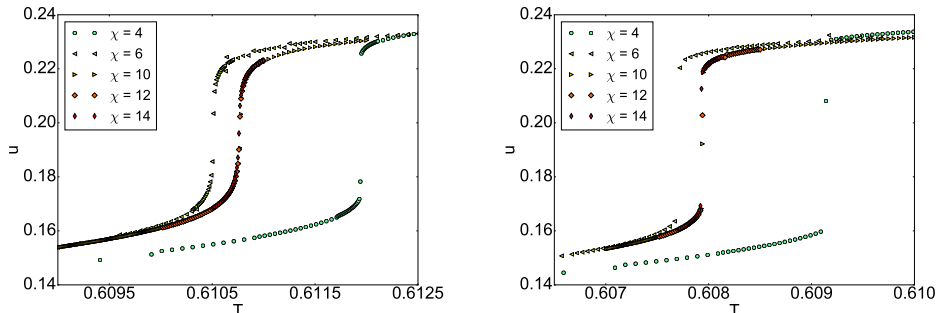


Figure 3.10: Left/right: internal energy per site u in the vicinity of the phase transition at $D = 1.9652/D = 1.9660$ for a few values of χ . On the left side the jump in internal energy is rapidly suppressed as one increases χ , on the right side the jump appears to remain finite.

our finite discretization) at a larger value. Thus in order to obtain true insights into the nature and location of a phase transition one must monitor their behavior as a function of χ .

By carefully monitoring the behavior of the various thermodynamic quantities we have been able to locate the tricritical point to good accuracy. However, to obtain the parameters D_t and T_t corresponding to the location of the tricritical point, as quoted in Tab. 3.1, we have relied on additional input from the behavior of the system's conformal data. We explain our procedure below. Our final estimate for the location of the tricritical point is shown as the yellow diamond in Fig. 3.11.

	MC [67]	FSS [68]	WL-I [69]	WL-II [70]	TNR
D_t	1.965(5)	1.9655(5)	1.966(2)	1.9660(1)	1.9658(1)
T_t	0.609(4)	0.610(5)	0.609(3)	0.6080(1)	0.6086(4)

Table 3.1: Estimates for the location of the tricritical point in the Blume-Capel model by means of various methods: Monte Carlo (MC), finite-size scaling (FSS), Wang-Landau MC (WL) and TNR.

3.4.2 Conformal data

As we mentioned in the beginning of this section, in the case of conformally invariant systems, the classification of a critical point may be carried out via the identification of its underlying CFT. It should be emphasized that such a characterization provides more comprehensive information than, for example, the characterization

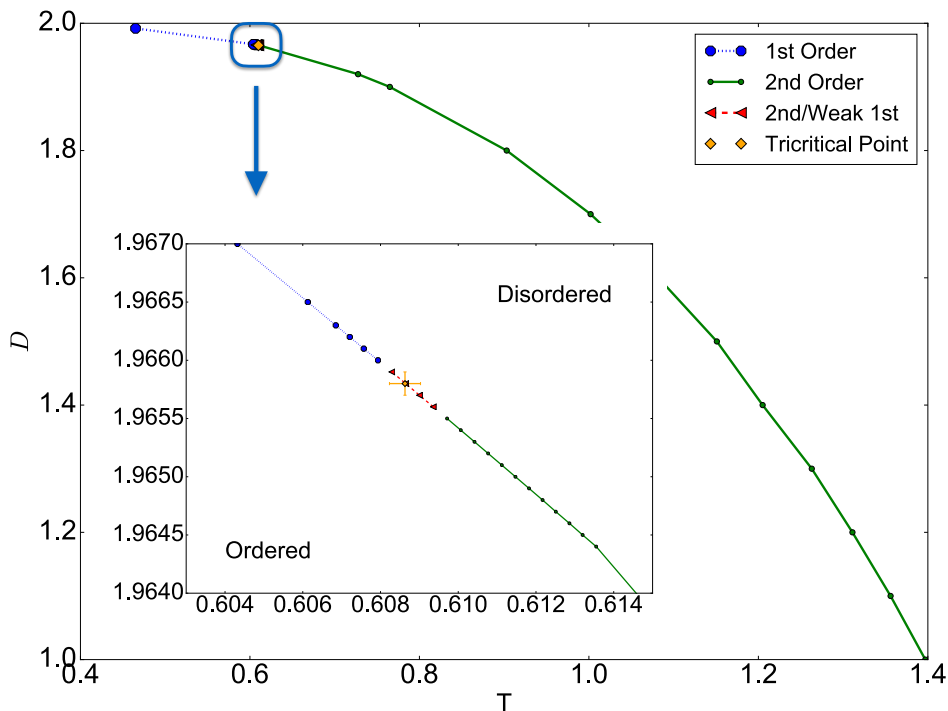


Figure 3.11: Main figure: Phase diagram of the Blume-Capel model obtained with a value of $\chi = 6$. Inset: phase diagram in the vicinity of the tricritical point obtained with a value $\chi = 12$. Red dashed (triangles) data corresponds to parameter values for which a conclusive determination of the type of transition was not possible via numerical differentiation.

of a universality class via a few critical exponents. Indeed, even though the latter may be obtained from the former, the converse does not necessarily hold.

For critical systems of finite size the partition function can be arranged in terms of the theory's so-called *scaling dimensions* $\{\Delta_\alpha\}$ and *central charge* c as

$$Z^{(L_x, L_y)} = e^{\beta f L_x L_y} \sum_{\alpha} e^{-2\pi \frac{L_y}{L_x} (\Delta_\alpha - \frac{c}{12}) + \dots} \quad (3.11)$$

where we have assumed a system of dimensions L_x and L_y using periodic boundary conditions at inverse temperature β [6, 72]. In the previous expression the ellipsis stands for higher-order corrections. This is a consequence of the fact that, in the continuum limit, the theory effectively corresponds to a conformally invariant theory.

Noting that in the TNR approach each tensor represents a system of $2^s \times 2^s$ sites after s coarse-graining iterations, and partially evaluating the tensor trace in Eq. (3.8), we may readily write

$$Z^{(2^s, 2^s)} = \text{Tr} \left(T^{(s)} \right) \quad (3.12)$$

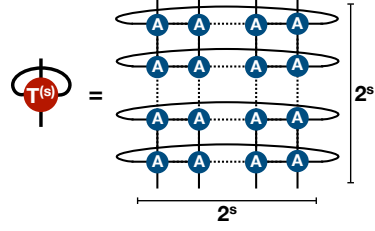


Figure 3.12: TNR tensor after s iterations.

with $T^{(s)}$ the transfer matrix defined in Fig. 3.12, *i.e.*, we may gain access to the theory's spectrum of scaling dimensions by looking at the spectrum of the transfer matrix $T^{(s)}$ [4, 6]. More precisely, one finds that⁶

$$\Delta_\alpha = \frac{1}{2\pi} \log(\lambda_\alpha / \lambda_0) \quad (3.13)$$

with λ_α the α^{th} eigenvalue of $T^{(s)}$.⁷

The extraction of the central charge c can be carried out in a number of ways. Here we employ a procedure in which by normalizing the tensor $T^{(0)} = A$ to remove the non-universal contribution $e^{\beta f L_x L_y}$, one may readily read out the value of c at each iteration from the leading eigenvalue of $T^{(s)}$. An alternative approach could have employed a fitting of the lowest eigenvalue as a function of system size.

We note that a nontrivial structure in Eq. (3.11) is only expected in the case of nontrivial fixed points. In the particular case of a critical fixed point the spectrum of scaling dimensions should remain invariant under RG transformations. It is this observation which we exploit to gain further insights when locating and characterizing the tricritical point. As the TNR algorithm has been shown to be capable of achieving (approximate) scale invariance at criticality, we make use of this to judge the vicinity of the tricritical point, *i.e.*, by looking for the parameter set for which the best scale invariance is achieved we obtain direct evidence of critical behavior. In addition, should we have a good hint for the spectrum of scaling dimensions expected, as we do here, one may use this as additional complementary information.

To obtain a quantifiable notion of scale invariance, which is adapted to our approach, we define the vector $\tilde{\alpha}^{(s)}$ as

⁶In writing this expression we rely on the assumption that the so-called *identity field* has the lowest lying scaling dimension $\Delta_0 = 0$. This is a justified assumption in the case of minimal unitary CFTs.

⁷Often it pays off to consider transfer matrices corresponding to wider cylinders, *i.e.*, one may often obtain more accurate spectra by staking several $T^{(s)}$ tensors along the horizontal direction. In that case one needs to adjust Eq. (3.13) to account for the difference between L_x and L_y .

$$\tilde{\alpha}_i^{(s)} = \frac{1}{\tilde{\Delta}_i^{(s)}} \quad (3.14)$$

with $\tilde{\Delta}_i^{(s)}$ the i^{th} scaling dimension as estimated from the spectrum of $T^{(s)}$ in (3.12) at scale s , for the lowest-lying scaling dimensions.⁸ Then, by computing

$$\tilde{F}(s) = \frac{\tilde{\alpha}^{(s)T} \cdot \tilde{\alpha}^{(s+1)}}{\|\tilde{\alpha}^{(s)}\| \|\tilde{\alpha}^{(s+1)}\|} \quad (3.15)$$

we obtain a direct *gauge-independent* measure of scale invariance.⁹ Since, in this case, we know what spectrum to expect, we may analogously define $F(s)$ by substituting $\tilde{\alpha}^{(s+1)}$ with the exact values α . In defining $\tilde{\alpha}^{(s)}$ above, we choose to use the inverse of the estimated scaling dimensions in order to give a larger weight to the lowest lying primary fields and their descendants in Eq. (3.15).

We show sample data in Fig. 3.13 for several values of D and scales. There it is possible to see how for the shortest scales all values of D result in an almost identical spectrum. This nicely reflects the fact that, for such short scales, we do not yet expect to see any proper signatures of universal behavior. That the spectra are nearly identical offers a very tempting interpretation in terms of the lattice giving the leading (RG *irrelevant*) contribution. Then for intermediate scales, *i.e.*, the fifth scale

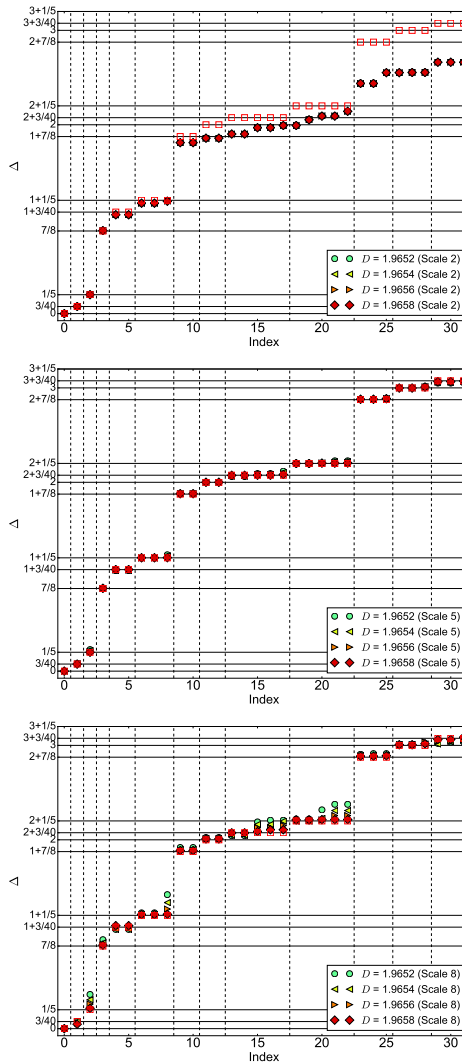


Figure 3.13: Lowest-lying scaling dimensions for the second (top), fifth (mid) and eighth (bot) scales, for a subset of D s at T_c . Exact CFT data is given by hollow squares (red).

⁸We leave out the lowest scaling dimension, corresponding to the identity field, since this would give a divergent contribution.

⁹See Ch. 4 for an explanation of the notion of gauge-invariance in tensor networks.

in the middle plot, the microscopic information has been effectively integrated out and the universal properties emerge, thus showing a very good agreement with the expected values (red hollow squares). Once coarse graining continues, the distance to the tricritical point (or numerical errors) leads to a flow away from the expected values.

Importantly, once we enter this final regime a hierarchy emerges, in which as we move away from the values D_t and T_t , see Tab. 3.1, the disagreement with the expected values builds up more rapidly. This exactly matches what would be expected from an RG point of view. In principle this flow could either lead to some (trivial) stable fixed point or, in the case in which we are sitting *exactly* on top of the line of second-order phase transitions, to the Ising fixed point.¹⁰ Here we find that the values never reproduce the Ising spectrum (data not shown), thus telling us that insufficient accuracy or numerical errors take the system away from the critical line.

In Fig. 3.14 we show sample curves illustrating the behavior of the quantity $|1 - F(s)|$ as a function of coarse-graining step (scale) s . There it can be seen how for the smallest value of χ shown no clear notion of scale invariance arises, as the curves increase monotonically. As we move to larger values of χ , some curves begin to flatten for the intermediate scales, reflecting proper scale invariance. Importantly, a subset of these curves develops dips showing improved invariance over all neighboring curves. It is these dips which we interpret as signatures of the close vicinity of the tricritical point. Interestingly the same hierarchy which was observed in Fig. 3.13 arises here in that the depth of the dips in the curves depends on the distance to the values D_t and T_t .

On the inset of Fig. 3.15 we show the values of the central charge c as a function of scale (iteration) evaluated at the estimated location of the tricritical point. There it can be clearly seen that a good degree of scale invariance is obtained between the scales 3 to 7, away from which we find values differing strongly from the expected value $c = 7/10$. The shape of this curve can be understood in a matter analogous to Fig. 3.13, as explained above.

On Fig. 3.15 we show the lowest 32 scaling dimensions at the estimated critical values D_t and T_t . As can be readily seen the agreement between the values computed and those expected is excellent with the largest deviation on the order of 0.8%.

To the best of our knowledge, this is the first time that so many scaling dimensions

¹⁰This is because of the fact that the whole line of critical points differs only by an RG irrelevant perturbation from the Ising fixed point.

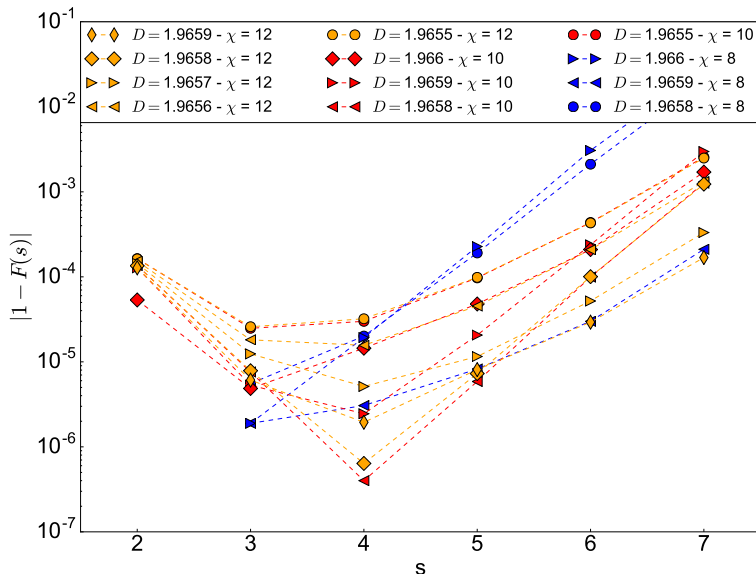


Figure 3.14: Scale invariance of the spectrum at various values of D_c , T_c and χ , as measured by the quantity $1 - F(s)$. See main text for definition of $F(s)$.

have been obtained from the Blume-Capel model with such a level of accuracy. The same holds for the central charge c where we obtain a deviation of about 0.07% with respect to the expected value $c = 7/10$. See Tab. 3.2 for a comparison with previous estimates.

	FSS [67]	WL [71]	TNR
c	0.698(9)	0.73(5)	0.7005

Table 3.2: Various estimates for the central charge c of the tricritical point in the Blume-Capel model.

We end the characterization of the tricritical point by showing the lowest lying set of scaling dimensions resolved by momentum and \mathbb{Z}_2 symmetry sector. This allows us to identify all (but one) of the so-called *primary fields* present in the expected CFT.¹¹ The data is shown in Fig. 3.16.

It should be emphasized that most of the computations we discuss here may be

¹¹The so-called ϵ'' field which, even though expected in the local \mathbb{Z}_2 even sector, having a scaling dimension $\Delta = 3$ is too far up in the spectrum to be unequivocally resolved from other descendant fields. The procedure for computing the scaling dimensions corresponding to non-local fields in a CFT was presented by Hauru *et al.* in Ref. [73].

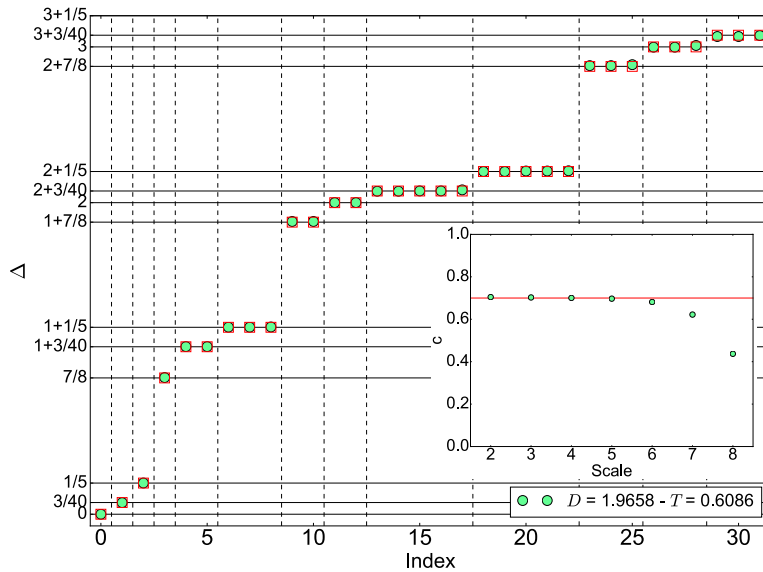


Figure 3.15: Estimated scaling dimensions at D_t and T_t using TNR with $\chi = 12$. Red hollow squares represent exact CFT data. Horizontal lines show exact values. Vertical lines show expected degeneracies. Inset: central charge c as a function of scale. Horizontal (red) line shows the exact value.

readily carried out, for instance, employing exact diagonalization techniques. The main advantage of the tensor network approach lies on two points: first, on the ability to reach larger system sizes, for which finite-size corrections become negligible and, second, to do so employing a coarse-graining transformation capable of preserving all relevant information to good accuracy. The latter is confirmed by our results.

3.5 Discussion

In this section we have rephrased the notion of a partition function within the tensor network language and have illustrated how the exponentially growing complexity of its exact evaluation may be circumvented by means of introducing the concept of a *contraction scheme* with which one may obtain a (approximate) compact representation efficiently, *i.e.*, in a time growing polynomially with a refinement parameter typically denoted as χ .

In the later parts of the chapter we have applied one of the most recently developed algorithms, namely the TNR algorithm, to the study of the so-called Blume-Capel

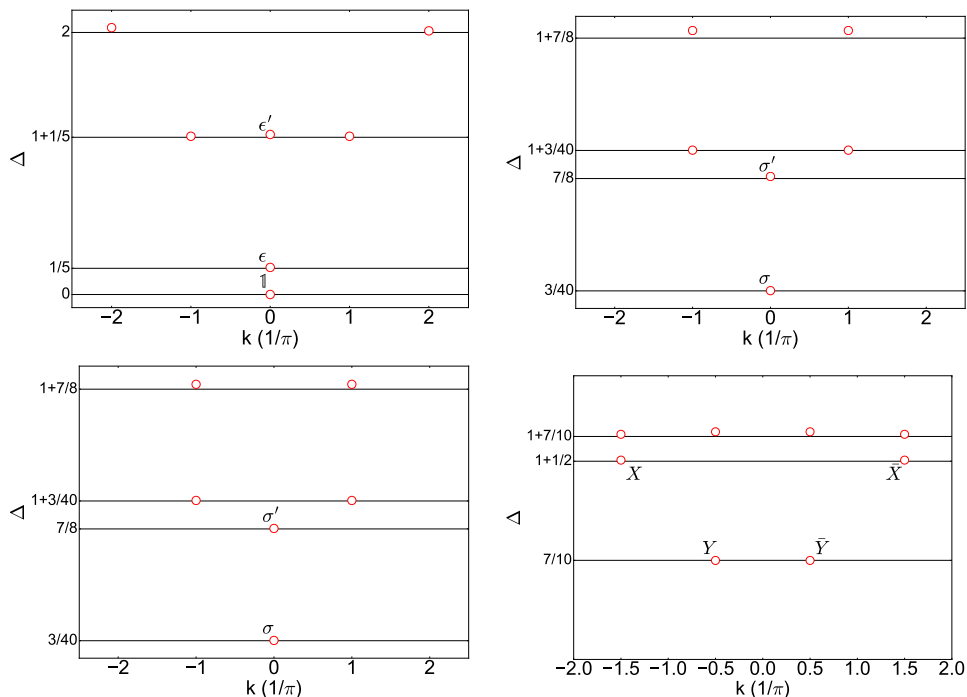


Figure 3.16: TNR estimates of the lowest lying scaling dimensions (red circles) at D_t and T_t , see Tab. 3.1, resolved according to symmetry sector, with primary fields labeled according to their usual names in the literature. Top left: local fields in the \mathbb{Z}_2 even sector, Top right: local fields in the \mathbb{Z}_2 odd sector, bottom left: nonlocal fields in the \mathbb{Z}_2 even sector, bottom right: nonlocal fields in the \mathbb{Z}_2 odd sector. Horizontal lines show the exact values.

model. We have used this model to illustrate a procedure which combines the accuracy of the TNR algorithm with its ability to generate proper RG flows in order to achieve a highly accurate characterization of the model's critical properties, a task which previously required input from multiple approaches. We believe this procedure to be rather generic, in that it relied on relatively basic RG considerations, and thus applicable to a broad class of models potentially exhibiting (multi-)critical points.

Given the level of accuracy achieved, we regard this study as setting the stage for even richer studies of the physics at the tricritical point of the Blume-Capel model. Indeed, one of the features which we have not fully exploited here is the ability of the TNR algorithm to produce lattice analogues of a CFT's scaling operators [64]. This is a feature which could lead to very interesting ramifications. For instance, by obtaining explicit lattice representations of the theory's scaling fields one could then study the effect of various RG irrelevant perturbations to the Ising fixed point to better understand the transition between two different CFTs (in this case

between the $c = 1/2$ (Ising) CFT and the $c = 7/10$ (tricritical Ising) CFT) and the mixing of operators in this process. To our knowledge, this is something which has only been done perturbatively in the past, see Refs. [74].

Another interesting aspect of the $c = 7/10$ CFT associated to the Blume-Capel model is that it is one of the simplest examples exhibiting so-called *supersymmetry*, *i.e.*, a type of symmetry connecting fermion-boson partner fields frequently discussed in the context of high-energy physics and extensions of the standard model of particle physics. The explicit construction of such partner fields may also prove to be interesting in studying the emergence of supersymmetry in classical spin models.

Chapter 4

Tensor network algorithms for quantum many-body systems

One of the most prominent challenges in modern day science pertains the understanding of systems made up of extensively many components in regimes where the interactions between them are by no means negligible or even weak. This is the so-called *many-body problem* in the *strongly-correlated* regime in which systems may typically no longer be treated reliably by means of (quasi-)free particle approaches.

Perhaps the largest underlying barrier to the understanding of strongly-correlated many-body systems arises purely because of the properties of the mathematical framework used for their description. Indeed, as one of the basic postulates of quantum mechanics dictates, the description of a composite quantum system is given by the tensor product of the Hilbert spaces associated to each of its constituent degrees of freedom,¹ *i.e.*, the many-body Hilbert space is given by

$$\mathcal{H}^{(N)} = \bigotimes_{i=1}^N \mathcal{H}_i \quad (4.1)$$

with N the number of constituents and \mathcal{H}_i their associated Hilbert spaces. Thus, a basic consequence of the tensor product structure intrinsic to the many-body space is its *exponential* growth in dimensionality as the number of constituents increases, *e.g.*, in the case of $S = 1/2$ spins one has $\dim[\mathcal{H}^{(N)}] = 2^N$.

To see why this constitutes a major roadblock in most cases, one may consider the simple case in which $N = 50$, which is rarely enough to be truly representative of the thermodynamic limit, where one finds $\dim[\mathcal{H}^{(50)}] = 2^{50}$. The relevant

¹For the sake of simplicity we restrict ourselves to *distinguishable* degrees of freedom.

figure for numerical simulations corresponds to the memory required for storing a vector in that (complex) Hilbert space. If one describes this vector in terms of double-precision floating point numbers, a simple calculation yields a total memory requirement of 8 Petabytes, almost ten times the amount of memory available in today's most powerful supercomputer. This tells us that the amount of computational resources required to describe a quantum many-body system exactly will rarely, if ever, be available. Thus major efforts have been invested in developing alternative approaches providing *efficient* descriptions of quantum many-body states, *i.e.*, descriptions involving only polynomially many parameters.

4.1 An entanglement-based approach

Tensor network algorithms (TNAs) constitute one of the most recent of such approaches and rely on the crucial observation that, even though the description of *generic* states in the exponentially growing Hilbert space is beyond reach for the system sizes typically required to obtain results representative of the thermodynamic limit, *ground states* of local Hamiltonians on the other hand appear to be very far from resembling generic states in this Hilbert space.

As a matter of fact one of the main forces driving the area of TNAs stems from a beautiful piece of work by Hastings [34], in which he shows how the ground state of a one-dimensional (1D) local Hamiltonian with a finite energy gap to excitations will necessarily obey what has been dubbed as an *area law* for entanglement entropy. Specifically, given the ground state $|\psi_0\rangle$ of an N -component 1D system, the von Neumann entropy \mathcal{S} of the system under bipartition, *i.e.*, the entanglement entropy, will satisfy

$$\mathcal{S}(\rho_{1,j}) := -\text{Tr}(\rho_{1,j} \log \rho_{1,j}) \leq \mathcal{S}_{max}, \quad (4.2)$$

with $\rho_{1,j} = \text{Tr}_{[j+1,N]}(|\psi_0\rangle\langle\psi_0|)$, the reduced density matrix supported over the first j sites of the chain and \mathcal{S}_{max} a constant satisfying: $\mathcal{S}_{max} < \infty, \forall N$. Just as importantly, Ref. [34] also shows how such a ground state admits an efficient representation in terms of so-called *matrix product states* (MPS) [37–39], thus providing sound footing to the MPS-based *density matrix renormalization group* (DMRG) proposed much earlier by White [40] which, until then, had relied mostly on empirical evidence to justify the validity of the approach.

Further works studying the entanglement properties of local Hamiltonians [35, 36, 75–79] have strengthened the notion that targeting the zero-measure space of states obeying an entanglement area law, see Fig. 4.1, or extensions thereof exhibiting well-defined entanglement properties, indeed constitutes a very promising approach to tackling the many-body problem. This has lent support to the development of

Ansatz wave functions specifically constructed to obey higher-dimensional versions of the area law (and generalizations), *i.e.*, wave functions obeying

$$\mathcal{S}(\rho_A) \sim \partial A, \tag{4.3}$$

with ∂A the surface area of the region enclosed by a subsystem A upon bipartition of the system, *e.g.*, as in Fig. 4.1. In two dimensions, for example, ∂A will represent the perimeter of the area enclosed by subsystem A and a subclass of such states goes under the name of *projected entangled-pair states* (PEPS) [43].

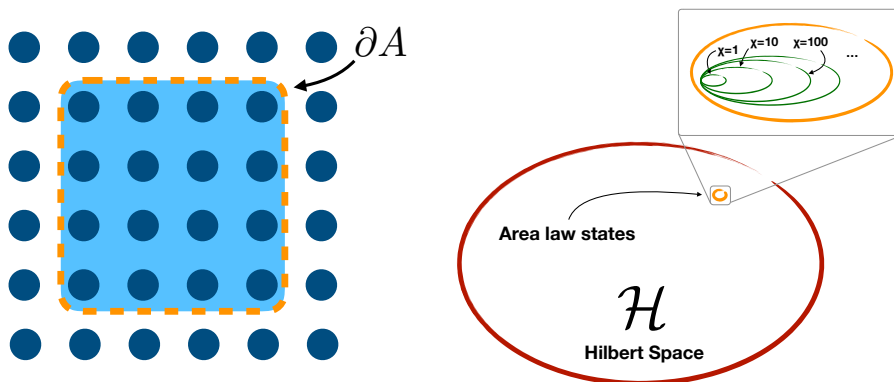


Figure 4.1: Left: schematic representation of a 2D state obeying an area law, where blue circles represent local degrees of freedom and the dashed line represents a bipartition of the system. Right: schematic representation of the many-body Hilbert space and the zero measure space of area law states. The inset illustrates how increasing a refinement parameter referred to as the *bond dimension*, here denoted as χ , allows to access larger portions of this subspace encoding increasingly more highly entangled states.

However, in spite of the considerable amount of evidence supporting approaches specifically targeting area-law states, there is, to date, no mathematical proof showing that gapped and local Hamiltonians in higher dimensions will necessarily satisfy the area-law constraint.² Conversely, it is now well-understood that some of these tensor network states are indeed ground states of gapped and local Hamiltonians, *i.e.*, their so-called parent Hamiltonian [81].

In the following sections we shall provide a broad overview of some basic techniques involved in tensor network simulations.

²On the other hand, examples of states obeying an area law have been found for which it has been proven that PEPS do *not* provide efficient representations [80]. These examples, however, correspond to states which are not expected to be efficiently preparable even by a quantum computer.

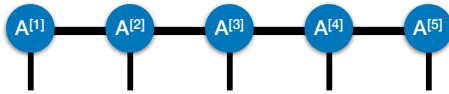


Figure 4.2: Matrix product state on a 5-site chain employing open boundary conditions. The variational parameters in the *Ansatz* are contained in each of the rank-3 A tensors. The horizontal dimensions (bonds) represent virtual degrees of freedom whereas the lower legs represent the physical degrees of freedom.

4.2 Matrix product states (MPS)

By now matrix product states have arguably become the golden standard for the simulation of strongly interacting 1D lattice models, however, even though it was Hastings' work which placed the class of MPS on solid grounds, simulations employing the DMRG had been frequently used starting more than a decade before Hastings' results were published, see Refs. [39, 82–87] and references therein.

Even though the precise historical development of the field is very interesting in itself, here we will fast-forward in time to a formulation which is by now regarded as a *de-facto* standard in the field of TNAs. Namely, we will begin with an introduction of MPS, taking some time to emphasize their most important properties, from which we will be able to formulate the DMRG in a very transparent way. Even though in our presentation we will only be touching upon the most important points, the curious reader is encouraged to consult the excellent review in Ref. [88].

4.2.1 Definition

Consider a system made up of N spins S placed on a 1D open chain.³ The *Ansatz* class of MPS is defined as

$$|\psi\rangle = \sum_{\{S_i\}} [A_{S_1}^{[1]} A_{S_2}^{[2]} \cdots A_{S_N}^{[N]}] |S_1, S_2, \cdots, S_N\rangle, \quad (4.4)$$

where each of the $A^{[i]}$ represents a rank-3 tensor of dimensions $[m_{i-1}, m_i, |S|]$, see Fig. 4.2, where the last dimension is fixed by the physical degree of freedom and m_{i-1}, m_i , represent the number of rows and columns, respectively, of the matrix obtained by fixing a physical state. By construction $m_0 = 1$ and $m_N = 1$ in the

³For the sake of simplicity we will focus the presentation on spin systems for now. Sec. 4.6 explains how the MPS *Ansatz* may be used to simulate fermionic systems.

case of an open chain, whereas periodic chains do not limit these dimensions and will then include a trace over the matrix product. The fact that the amplitude $\psi_{S_1, S_2, \dots, S_N}$, corresponding to a basis state $|S_1, S_2, \dots, S_N\rangle$, is given by (the trace over) a product of matrices motivates the name of the *Ansatz*. The row and column indices of the matrices $A_{S_i}^{[i]}$ are typically referred to as *virtual* indices, or degrees of freedom, and the largest dimension among these virtual spaces, *i.e.*, the largest m_i , is referred to as the *bond dimension*, traditionally denoted by m .

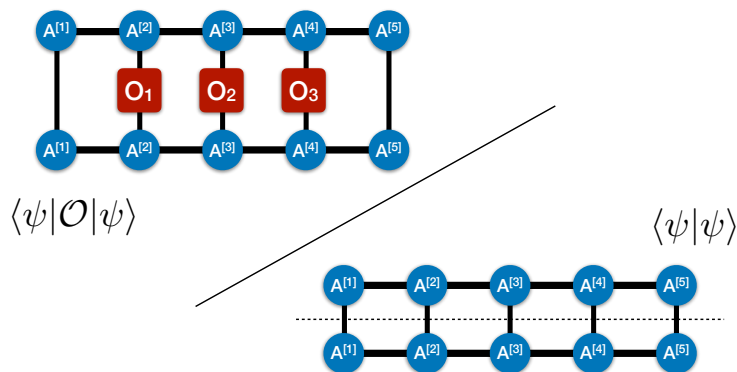


Figure 4.3: Tensor networks representing the expectation value $\langle \psi | \mathcal{O} | \psi \rangle / \langle \psi | \psi \rangle$ of an operator made up of 3 local operators \mathcal{O}_1 , \mathcal{O}_2 , \mathcal{O}_3 , acting on sites 2, 3 and 4, using MPS. The dashed line running through the diagram of the norm emphasizes the convention employed in which the mirror reflection of an MPS tensor corresponds to its complex conjugate.

4.2.2 Some key properties

Several important properties make the class of MPS a very versatile approach for the simulation of quantum systems. Some of the most important ones are:

- ▷ **Efficient encodings:** as is apparent from Eq. (4.4) the number of values required to fully specify the *Ansatz* is given by $\sum_i |A^{[i]}| \sim \mathcal{O}(N)$, with $|A^{[i]}|$ the number of entries in the tensor $A^{[i]}$. Thus one obtains an efficient encoding which scales *linearly* with the system size.
- ▷ **Efficient evaluations:** the evaluation of generic observables can be carried out by constructing tensor networks analogous to that in Fig. 4.3. The contraction of such a tensor network may be carried out as illustrated in Fig. 4.4 with a computational complexity scaling as $\mathcal{O}(Nm^3)$, *i.e.*, scaling *linearly* with system size and *polynomially* with the bond dimension m .

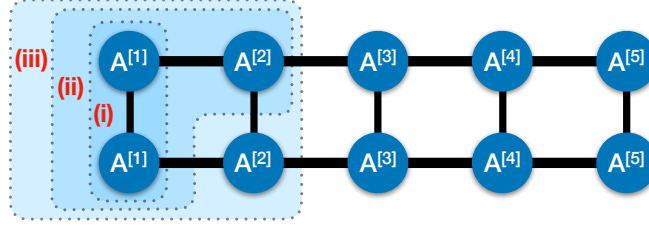


Figure 4.4: Schematic illustrating a possible sequence of contractions giving an optimal computational complexity for the evaluation of the MPS norm $\langle \psi | \psi \rangle$. Assuming m and d to be the values of all virtual and physical dimensions, respectively, one finds the following sequence of computational complexities: (i) $\mathcal{O}(dm^2)$, (ii) $\mathcal{O}(dm^3)$, (iii) $\mathcal{O}(dm^3)$. From this point on one need only repeat steps (ii) and (iii) for as long as required. Insertion of operators can be carried out by precomputing the product of the operator with the corresponding MPS tensor at a subleading cost of $\mathcal{O}(d^2m^2)$.

- ▷ **Intrinsic gauge freedom:** as may be readily verified any MPS state encoded by a set of tensors $\{A^{[i]}\}$ is completely invariant under the introduction of resolutions of identity, RR^{-1} , for any invertible matrix R , at any bond (index) joining the *Ansatz* tensors A , see Fig. 4.5. This gauge freedom plays an important role in the stability of numerical simulations, as we will explain below.

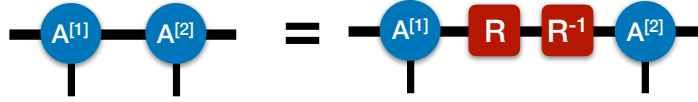


Figure 4.5: Schematic illustrating the gauge freedom intrinsic to MPS.

As is simple to show, provided one does not constrain the bond dimension m , *any* quantum state $|\psi\rangle$ may be decomposed as in Eq. (4.4). This brings about a very convenient numerical framework, where key properties of the wave function may be readily computed while at the same time providing a means to systematically obtain controlled approximations. To see this consider the *Schmidt decomposition* of the state [89] with respect to a bipartition into subsystems A and B

$$|\psi\rangle = \sum_{i=1}^k \lambda_i |i\rangle_A |i\rangle_B, \quad (4.5)$$

where k is upper-bounded by $\min[\dim(\mathcal{H}_A), \dim(\mathcal{H}_B)]$, $|i\rangle_A$ and $|i\rangle_B$ represent basis states on each component of the bipartition and $\{\lambda_i\}$ represents the set of so-called *Schmidt values*. These values are positive definite by construction and the number of them, $k = |\{\lambda_i\}|$, defines the *Schmidt rank* of the state.

Representing a state in its Schmidt form has a number of advantages. For instance a series of approximations may be systematically obtained by the set of states $\{|\tilde{\psi}_m\rangle\}$ with Schmidt rank $m \leq k$ with respect to the given bipartition. For each of these states an error

$$\epsilon_m = \|\psi\rangle - |\tilde{\psi}_m\rangle\|^2 \tag{4.6}$$

$$= \sum_{i=m+1}^k \lambda_i^2, \tag{4.7}$$

satisfying $\lim_{m \rightarrow k} \epsilon_m \rightarrow 0$, is introduced.⁴ Thus providing a handle on the accuracy of the approximation in terms of m . Moreover, the form in Eq. (4.5) allows for a direct computation of the entanglement entropy, *v.s.* Eq. (4.2), with respect to the chosen bipartition, in terms of the Schmidt values as

$$\mathcal{S}_{AB} = - \sum_{i=1}^m \lambda_i^2 \log \lambda_i^2. \tag{4.8}$$

From here it is then straightforward to see how the entanglement entropy is upper bounded by $\mathcal{S}_{AB} = \log m$, which is independent of the number of sites N . This corresponds to the area law mentioned above.

By making use of the gauge freedom intrinsic to MPS, one may impose so-called isometric constraints on the tensors $A^{[i]}$, in order to bring it into its Schmidt form. This may be achieved simply by means of subsequent QR (or SVD) decompositions starting from both ends of the system and working ones way towards a target bond/site, see Fig. 4.6.

An MPS in its Schmidt form is at times also referred to as being in the *unitary gauge* or its *canonical form* with respect to a given bipartition. The name arises due to the fact that all tensors in the MPS (except for the matrix containing the Schmidt values) now obey isometric constraints, *i.e.*, satisfy either $QQ^\dagger = 1$ or $Q^\dagger Q = 1$ when coupling one of the virtual indices to the physical index to form a matrix, see Fig. 4.6.

Crucially, this procedure would not be available should we have chosen to work using periodic boundary conditions, *i.e.*, had we introduced a *loop* into the lattice.

⁴In writing this expression we assume the state $|\psi\rangle$ to be properly normalized, whereas we leave the state $|\tilde{\psi}\rangle$ in its unnormalized form, *i.e.*, it will satisfy $\langle\tilde{\psi}|\tilde{\psi}\rangle = \sum_{i=1}^m \lambda_i^2$.

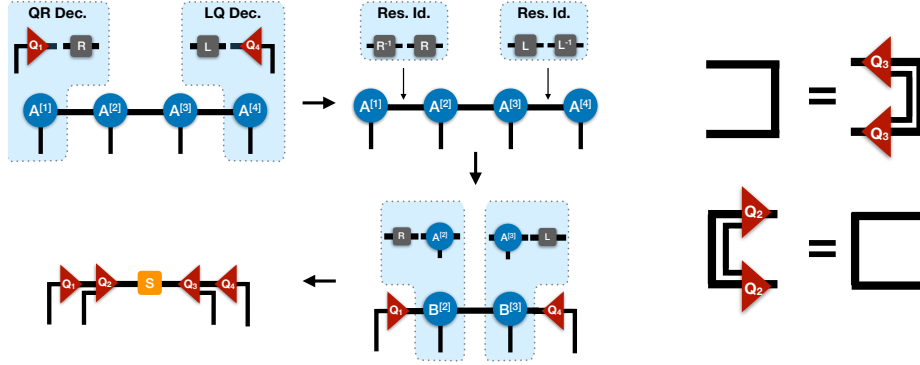


Figure 4.6: Left: MPS canonicalization procedure. By sequential QR/LQ decompositions one may work from the edges of the chain towards the middle to obtain the so-called canonical form of the MPS. In this form the diagonal matrix S in the middle bond contains the Schmidt values of the state. The rest of the tensors are in left/right canonical form, where they obey isometric constraints. Right: illustration of isometric constraints $QQ^\dagger = 1$ or $Q^\dagger Q = 1$ on tensors Q . Tensors Q_1 and Q_2 are said to be in their *left canonical* form whereas tensors Q_3 and Q_4 are said to be in their *right canonical* form.

4.2.3 Matrix product operators (MPO)

The idea of factorizing a state into a product of matrices can be readily extended to operators. Indeed, the definition is entirely analogous to that in Eq. (4.4), with

$$\hat{O} = \sum_{\{S_i, S'_i\}} [\mathcal{O}_{S_1, S'_1}^{[1]} \mathcal{O}_{S_2, S'_2}^{[2]} \cdots \mathcal{O}_{S_N, S'_N}^{[N]}] |S_1, S_2, \dots, S_N\rangle \langle S'_1, S'_2, \dots, S'_N|, \quad (4.9)$$

where $\{\mathcal{O}^{[i]}\}$ now represents a set of rank-4 tensors each of which carries two indices corresponding to the physical degrees of freedom at site i , see Fig. 4.7. As before, in the case with open boundary conditions the tensors at the edges will have one trivial index.

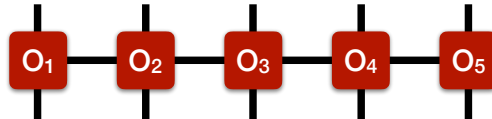


Figure 4.7: Illustration of a matrix product operator on a 5-site system.

Analogously to MPS, any operator acting on a many-body Hilbert space may be written down in the form of Eq. (4.9) [88, 90]. Perhaps more importantly, it has been shown how large classes of physically relevant operators, *e.g.*, Hamiltonians, may be systematically constructed by employing so-called *finite-state machines* [91, 92]. This becomes very handy during the numerical optimization of MPS wave functions, as developing the DMRG algorithm using MPO encodings of Hamiltonians allows for a very generic formulation of the codes employed for the simulations [93–95].

4.2.4 The density matrix renormalization group (DMRG)

As was mentioned above, the whole area of tensor network algorithms essentially came to life with the invention of the so-called Density Matrix Renormalization Group as formulated initially by White [40].

In numerical simulations the manifold of MPS is used as a variational class of states the entries of which are to be optimized in order to obtain accurate approximations of the ground, and low-lying excited, states of a model. To achieve this the DMRG algorithm is formulated as an optimization problem targeting the minimization of the cost functional

$$f[\{A\}] = \langle \psi(\{A\}) | H | \psi(\{A\}) \rangle + \lambda(1 - \langle \psi(\{A\}) | \psi(\{A\}) \rangle) \quad (4.10)$$

with $|\psi\rangle$ given in the MPS form of Eq. (4.4). This cost functional has its global minima in the set of ground states of the Hamiltonian H , on which the variable λ takes the value of the ground-state energy E_0 .

The optimization of the tensors takes place following a sweeping pattern in which a single tensor $A^{[i]}$ is optimized at a time, keeping the rest of the tensors fixed.

More precisely, suppose we would like to optimize the entries of tensor $A^{[i]}$ then, by defining \mathbf{a}_i to be the entries of this tensor in vector form, we may write Eq. (4.10) as

$$f[\mathbf{a}_i^\dagger, \mathbf{a}_i] = \mathbf{a}_i^\dagger \mathcal{H} \mathbf{a}_i + \lambda(1 - \mathbf{a}_i^\dagger \mathcal{N} \mathbf{a}_i), \quad (4.11)$$

with matrices \mathcal{H} and \mathcal{N} defined in Fig. 4.8.

Since \mathbf{a}_i appears twice in each term, *i.e.*, the bra and ket components, this is a quadratic problem with respect to the entries of each tensor the solution of which may be found by computing $\partial_{\mathbf{a}_i^\dagger} f[\mathbf{a}_i^\dagger, \mathbf{a}_i] = 0$. This leads to the generalized eigenvalue problem

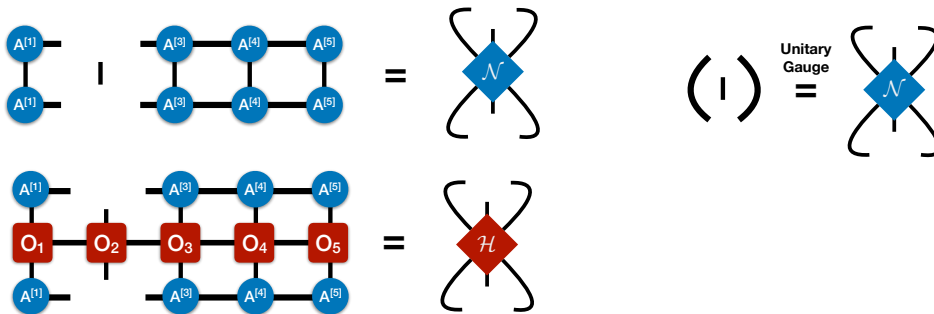


Figure 4.8: Left: definition of tensors \mathcal{N} and \mathcal{H} corresponding to effective single-site norm and Hamiltonian from the DMRG procedure. When interpreting them as matrices we do so by combining bra/ket indices. Right: reduction of norm network to the identity, $\mathcal{N} = 1$, upon switching to the unitary gauge.

$$\mathcal{H}\mathbf{a}_i = \lambda \mathcal{N}\mathbf{a}_i. \quad (4.12)$$

However, one may simplify this expression by imposing the unitary gauge mentioned in the previous section. As Figs. 4.6 and 4.8 illustrate such a choice results in $\mathcal{N} = 1$, so that Eq. (4.12) now becomes a *regular* eigenvalue problem

$$\mathcal{H}\tilde{\mathbf{a}}_i = \lambda \tilde{\mathbf{a}}_i. \quad (4.13)$$

The ability to choose a gauge in which the optimization problem in Eq. (4.10) is translated into a regular eigenvalue problem is not to be underestimated. By getting rid of the matrix \mathcal{N} , one may rely on very stable linear algebra libraries, *e.g.*, LAPACK, for solving the system of equations (4.13). Had we not implemented such a gauge, the stability of an algorithm solving Eq. (4.12) could have depended *heavily* on the conditioning of the matrix \mathcal{N} .

Once a solution $\tilde{\mathbf{a}}_i$ to the problem in Eq. 4.13 has been found, one may regauge this new tensor into canonical form and proceed with the next site.⁵

It should be noted that the DMRG algorithm as originally presented in [40], and discussed here, provides no guarantee of convergence to the true ground state of a given model. Indeed, in practice it is widely known how starting from too large a bond dimension can potentially trap the algorithm in local minima.⁶ A more

⁵Actually, the optimization need not be constrained to this so-called *single-site* optimization. A *two-site* optimization in which, as the name indicates, two sites are optimized simultaneously is also very frequently employed. This two-site approach provides access to the so-called *truncated weight* of Eq. (4.6) and can be used to adjust the bond dimension m at run-time.

⁶For most practical applications, however, a slow ramping up of the bond dimension during the simulation usually works quite well.

recent proposal for a modified version of the original algorithm provides a variant which can be guaranteed to converge to the true ground state of any gapped 1D system [96], albeit at a reduced efficiency.

The infinite density matrix renormalization group

The ideas presented in the previous section can be readily extended to the simulation of infinite size systems. Originally the proposal in Ref. [40] involved a growing procedure broken into steps in which first the system size would be increased by inserting two sites into the middle of a chain and then an effective two-site problem over the newly inserted sites would be solved. In this effective two-site problem the information from previous iterations (scales) would be implicitly contained in two *boundary blocks*, see Fig. 4.9, which could no longer be optimized.

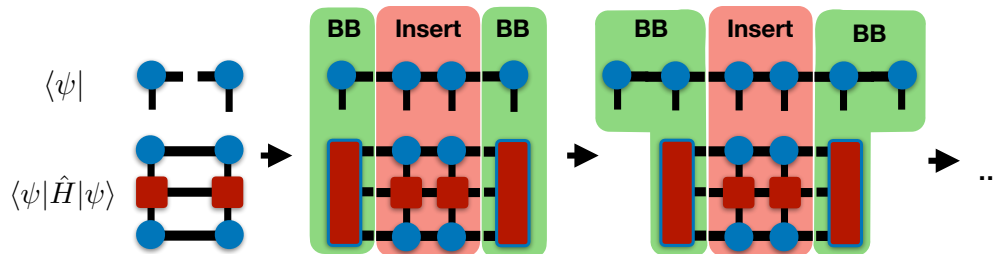


Figure 4.9: Illustration of a 2-site infinite DMRG growing procedure. At each step (scale) the system is grown by inserting 2 additional sites in the middle of the chain (red background). The diagrams in the lower row show the boundary blocks used to represent the energy expectation value (BB - green background). Only the tensors in the middle red area may be optimized.

Employing the new MPS picture it becomes clear that such a growing procedure may be generalized to arbitrary growing patterns while preserving the MPS form of the state during the entire simulation. In this way one obtains greater flexibility while preserving efficiency throughout. Moreover, the MPS picture also provides direct access to a proper measure of convergence to the thermodynamic limit, *i.e.*, by preserving the Schmidt spectrum between scales one may monitor convergence by computing the fidelity between reduced density matrices at subsequent scales [88]. In addition, as shown by Orús and Vidal in Ref. [97], one may again exploit the *Ansatz*' gauge freedom to add a step at the end of the simulation which allows one to use the growing pattern of tensors as the unit cell for an effectively infinite system and thus perform measurements directly in the thermodynamic limit. An illustration of how the proposal in Ref. [97] may be extended to generic growing patterns, potentially including two-dimensional (2D) systems, can be found in Refs. [88, 98].

Given that the only major conceptual modification required for the formulation of the infinite size form of the algorithm is the introduction of *environment blocks*, one may readily make use of all the framework introduced above where, instead of sweeping through the whole system, one simply sweeps over the unit cell of tensors describing the growing pattern while the remaining information, from previous iterations of the growing procedure, stays stored in the environment blocks.

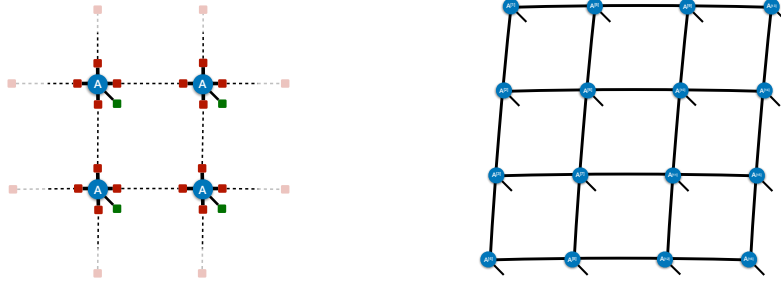


Figure 4.10: Left: illustration of a translation invariant PEPS construction via insertion of PEPS projectors (blue circles) mapping a covering of virtual entangled pairs (red squares/dashed lines) onto the physical space (green squares). Right: final form of the PEPS *Ansatz* on a 4 by 4 square lattice after tracing out of the auxiliary degrees of freedom.

4.3 Projected entangled-pair states (PEPS)

In this section we introduce one of the most well-known generalizations of MPS to higher dimensions. This class of *Ansatz* states was introduced by Verstraete and Cirac in Ref. [43] and goes under the name of *projected entangled-pair states*.

4.3.1 Definition

The class of PEPS targets the manifold of area-law states by employing a construction in which, in a first step, pairs of perfectly entangled states, *i.e.*, states of the form $|\phi\rangle = \sum_i |i\rangle|i\rangle$, of auxiliary, or virtual, degrees of freedom are introduced over the edges of a lattice. Thus endowing each site of the lattice with a number of virtual degrees of freedom equal to its coordination number k . In a second step these degrees of freedom are projected onto the physical space employing a set of projectors $A^{[i]}$, with each of the $A^{[i]}$ a tensor of rank $k + 1$ and the additional index corresponding to the local physical degree of freedom, see Fig. 4.10.

Since the process of projecting these fully entangled virtual degrees of freedom

leads to a summation over common indices, belonging to projectors located on neighboring physical sites, the final form of the PEPS state is thus given by

$$|\psi\rangle = \sum_{\{S_i\}} tTr[A_{S_1}^{[1]} A_{S_2}^{[2]} \cdots A_{S_N}^{[N]}] |S_1, S_2, \dots, S_N\rangle, \quad (4.14)$$

where tTr denotes the so-called *tensor trace* and corresponds to a summation over all virtual indices in the *Ansatz*, see Fig. 4.10. It should be noted that this is a form which is completely independent of the dimensionality of space and in the special case of a 1D chain, one recovers the same expression for an MPS, *i.e.*, Eq. (4.4). As in the case of MPS the dimension of the largest virtual space is referred to as the bond dimension of the *Ansatz* and for PEPS it is traditionally labelled by D .

Importantly, the construction presented above in terms of a covering of perfectly entangled states over the edges of a lattice makes it explicit that, upon consideration of systems large enough, such states will *necessarily* obey an area law for entanglement entropy as any bipartition of the system will cut a number of entangled pairs equal to the number of bonds traversed by the boundary of the bipartition.

The development of PEPS is, in some sense, really nothing more than the culmination of a series of developments based on the idea of employing a tensor product structure as a resource for building *Ansatz* states, which had already been explored earlier in the form of *tensor product states* [41, 42].

4.3.2 Some key properties

As with MPS there are a number of properties which make this *Ansatz* an attractive one from the perspective of numerical simulations. As we shall see, however, not all of the advantageous features present in an MPS simulation will find their way to PEPS simulations. Some of the basic properties of PEPS are

- ▷ **Efficient encodings:** analogously to the case of MPS, and as is apparent from Eq. (4.14), the number of values required to fully specify the *Ansatz* is given by $\sum_i |A^{[i]}| \sim \mathcal{O}(N)$, with $|A^{[i]}|$ the number of entries in the tensor $A^{[i]}$. Thus the PEPS encoding scales *linearly* with the system size.
- ▷ **Inefficient exact evaluations:** the evaluation of generic observables can be carried out by constructing tensor networks analogous to that in Fig. 4.11. As one may easily convince oneself the *exact* evaluation of such tensor networks entails a computational cost scaling *exponentially* with the smallest system dimension w , *i.e.*, scaling as $\mathcal{O}(D^{2w})$.⁷ As a matter of fact such computations

⁷The additional factor of 2 arises due to the double-layer bra-ket structure of the tensor network.

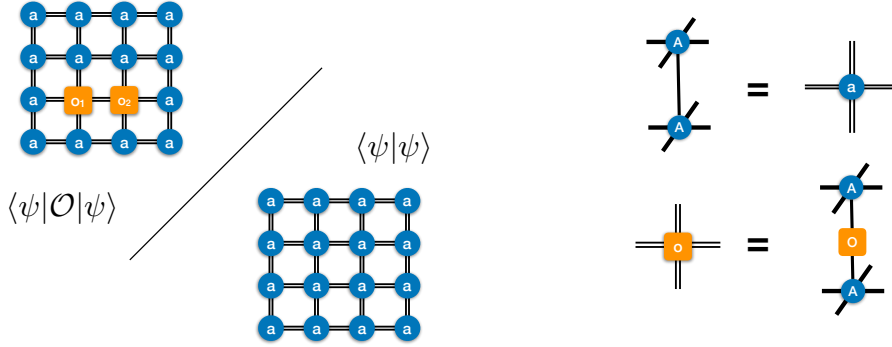


Figure 4.11: Left: illustration of typical tensor networks arising in the evaluation of the expectation values $\langle \psi | \mathcal{O} | \psi \rangle / \langle \psi | \psi \rangle$. In this case we show the measurement of an operator made up of 2 local operators (yellow squares). We denote the bra and ket virtual indices by means of double lines. Right: definition of the double-layer tensors a and o employed in the evaluation of observables.

have been shown to belong to the complexity class #P-complete [99].

In practice one resorts to *approximate* evaluations which can be carried out with a computational complexity scaling *polynomially* with the bond dimension D as well as an auxiliary bond dimension, typically denoted by χ , which controls the accuracy of the approximation. This gives a practical way of performing all evaluations required in a controlled way and is an approach which is expected to be justified for PEPS offering good approximations of gapped local Hamiltonians [100].

- ▷ **Intrinsic gauge freedom:** as in the case of MPS, it is also apparent from the form of the PEPS *Ansatz* that these encodings share the same notion of gauge invariance, *i.e.*, they remain invariant under the insertion of resolutions of identity, RR^{-1} , on any bond. This gauge invariance also plays an important role in the stability of numerical PEPS simulations, albeit in a more heuristic way.

Unlike in the case of MPS, it is in general not possible to exploit the gauge freedom intrinsic to PEPS to simplify the various computations involved in numerical calculations. Consider for example the quantity ϵ in Eq. (4.6) where two PEPS wave functions $|\psi\rangle$ and $|\tilde{\psi}\rangle$ differ only at a single tensor b

$$\begin{aligned}
 \epsilon &= \|\psi - \tilde{\psi}\|^2 \\
 &= \langle \psi | \psi \rangle + \langle \tilde{\psi} | \tilde{\psi} \rangle - \langle \tilde{\psi} | \psi \rangle - \langle \psi | \tilde{\psi} \rangle \\
 &= \mathbf{b}^\dagger \mathcal{N} \mathbf{b} + \tilde{\mathbf{b}}^\dagger \mathcal{N} \tilde{\mathbf{b}} - \tilde{\mathbf{b}}^\dagger \mathcal{N} \mathbf{b} - \mathbf{b}^\dagger \mathcal{N} \tilde{\mathbf{b}},
 \end{aligned}
 \tag{4.15}$$

where we single out the vectorization of the differing tensors \mathbf{b} and $\tilde{\mathbf{b}}$. The computation of this quantity involves the matrix \mathcal{N} , defined in Fig. 4.12, which in the case of PEPS cannot be regauged to yield the identity. The reason is that to enforce such isometric constraints one requires one-dimensional paths along which to decompose matrices into isometric and non-isometric parts, the latter of which can then be shifted along the path until some target site. As Fig. 4.12 illustrates, such paths are no longer available whenever the links of the lattice form loops.⁸

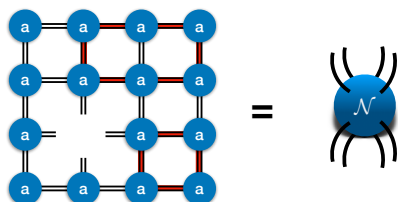


Figure 4.12: Single-site PEPS norm tensor network. The red lines emphasize the presence of loops, preventing a regauging of matrix \mathcal{N} into the identity. When interpreting \mathcal{N} as a matrix we do so by grouping bra (top) and ket (bottom) indices.

It is also not a straightforward matter to obtain the Schmidt decomposition of a PEPS. In fact obtaining this decomposition requires that one regroup the PEPS into MPS form so that the same techniques of the previous section may then be used. This regrouping, however, entails a cost growing exponentially with the linear size of the PEPS. For this reason the direct computation of quantities like *e.g.*, the entanglement entropy is rather rare and typically restricted to tree-like lattices where simplifications occur [101, 102].

Infinite projected entangled-pair states (iPEPS)

The PEPS *Ansatz* may be readily generalized to systems of an infinite size, where the *Ansatz* is known as *infinite* PEPS.

⁸Alternative approaches, however, make clever use of tree-like lattices which exhibit the same local motifs as the physical lattice of interest to achieve such a canonical form. The caveat of such an approach is that it involves the introduction of an intrinsically *uncontrolled* approxima-

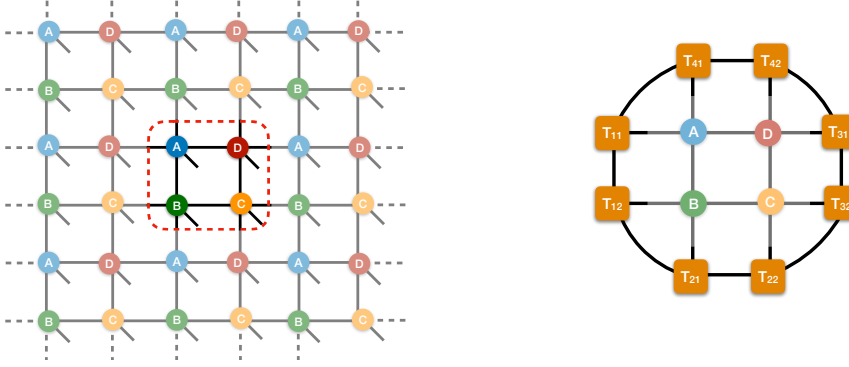


Figure 4.13: Left: illustration of an iPEPS wave function with a 4-site unit cell on the square lattice. Right: illustration of environment tensors (orange squares), typically arising in the optimization and evaluation of observables with both finite as well as infinite PEPS.

To directly address states in the thermodynamic limit, one proceeds by defining a unit cell that generates the full wave function, see Fig. 4.13. In practice both the evaluation of observables as well as the optimization of the iPEPS wave function can be carried out in a matter essentially identical to the way it is done for finite systems. Indeed, the key point is to note that whenever evaluating (local) observables, as well as optimizing the PEPS tensors, all computations may be implemented employing effective *environment* tensors, see Fig. 4.13, which allow to abstract away information related to system size. Thus much of what will be discussed below can be applied directly to systems regardless of their size.

As we will point out along the way, a few subtle differences do arise. One of the most notorious ones being the fact that iPEPS simulations generically lead to solving highly nonlinear optimization problems.

4.3.3 Projected entangled-pair operators (PEPO)

As was the case with MPOs, it is also possible to obtain decompositions of operators of interest on higher-dimensional lattices in terms of so-called *projected entangled-pair operators* which follow a straightforward generalization of Eq. (4.9)

$$\hat{O} = \sum_{\{S_i, S'_i\}} \text{tTr}[\mathcal{O}_{S_1, S'_1}^{[1]} \mathcal{O}_{S_2, S'_2}^{[2]} \cdots \mathcal{O}_{S_N, S'_N}^{[N]}] |S_1, S_2, \dots, S_N\rangle \langle S'_1, S'_2, \dots, S'_N|, \quad (4.16)$$

tion, which may alter the underlying physics of the problem in non-obvious ways, *e.g.*, reducing frustration in a lattice.

where each of the $\{\mathcal{O}^{[i]}\}$ represents now a tensor of rank $k + 2$ with 2 indices running over the local bra and ket physical degrees of freedom and the remaining k connect to all neighboring PEPO tensors. Just as for MPOs, there are well-defined procedures which allow to build PEPOs for wide classes of operators. Interestingly, such constructions can be visualized very intuitively in terms of particle decay processes, see Ref. [103].

Unlike in the 1D case, however, PEPOs are much less widely used in PEPS ground-state calculations, most likely due to the overhead incurred in implementing PEPO-based optimization on top of the intrinsically expensive PEPS calculations.⁹ On the other hand, PEPOs have seen moderate-spread use in finite temperature tensor network calculations of 2D systems [54, 104, 105], where they naturally arise.

4.3.4 Contraction schemes

As mentioned at the beginning of this section, one of the main caveats of performing simulations based on the PEPS *Ansatz* arises due to the intrinsic exponential scaling of exact computation of observables. This is why, in practice, one is forced to introduce approximate procedures with which to carry out the evaluation of various tensor networks arising in PEPS simulations. Such approximations are generically referred to as *contraction schemes*, just as in the classical case discussed in Sec. 3.3.

MPS-MPO scheme

In this scheme the idea is to make use of the similarity between the procedure of compressing an MPS state obtained by acting on an MPS with an MPO, see Fig. 4.14, and is perhaps the most widely used approach whenever dealing with systems of a finite size with open boundary conditions (OBC).

To be more precise, take a state $|\tilde{\psi}_L^{(1)}\rangle$ in MPS form describing the left-most column of the tensor network in Fig. 4.14, where each MPS tensor $\beta^{[i]}$ is initially given by the contraction of the physical indices of each of the left-most bra and ket PEPS tensors $\mathbf{A}^{[i,1]}$ at each row i . Thus, the "physical" indices of this new MPS correspond to the combination of the right virtual index of the PEPS tensor $\mathbf{A}^{[i,1]}$ and that of its complex conjugate. Similarly, one may build an MPO description $\mathcal{O}^{[j]}$ of the j^{th} column transfer matrix by contracting all tensors $\{\mathbf{A}^{[i,j]}\}$ with their corresponding complex conjugates, *i.e.*, each MPO tensor $\mathbf{a}^{[i,j]}$ is now made up by contracting the physical index in $\mathbf{A}^{[i,j]}$ with that of its complex conjugate, as in Fig. 4.11.

⁹This could be why, to the author's knowledge, there has been no PEPO based ground-state optimization employed to date.

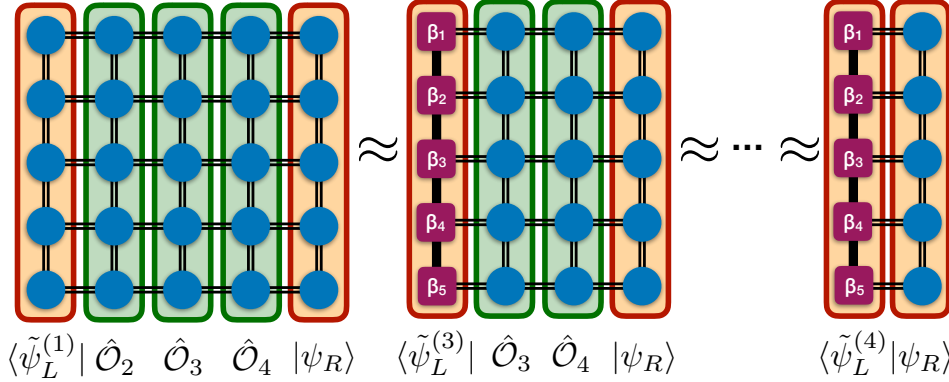


Figure 4.14: MPS-MPO contraction of a PEPS norm tensor network. At each step one compresses the action of a double layer PEPS MPO column on the boundary MPS back into MPS form by keeping the bond dimension fixed to some predefined maximum.

Using the picture above one may carry out the calculation of a norm tensor network, for example, as $\langle \tilde{\psi}_L^{(1)} | \mathcal{O}^{[1]} \mathcal{O}^{[2]} \dots \mathcal{O}^{[r-1]} | \psi_R \rangle$ by acting sequentially with the column MPOs on the edge MPS, as in Fig. 4.14. Since repeating this computation over several columns would entail the exponential growth of the virtual dimensions in $\langle \tilde{\psi}_L^{(i)} |$, one performs a compression of the combined MPS-MPO object at each step i by searching for the edge MPS $\langle \tilde{\psi}_L^{[i+1]} |$ minimizing the cost function

$$\epsilon^{[i]} = \|\langle \psi_L^{[i]} | \mathcal{O}^{[i+1]} - \langle \tilde{\psi}_L^{[i+1]} | \|^2, \quad (4.17)$$

over the manifold of MPS with a maximum auxiliary bond dimension χ . Once the MPS minimizing this function has been found, one sets $\langle \psi_L^{[i+1]} | = \langle \tilde{\psi}_L^{[i+1]} |$ and $i = i + 1$.

This compression may be carried out following an alternating least-squares procedure analogous to that in the DMRG algorithm in which, by targeting a specific tensor $\tilde{\beta}_j$ in $\langle \tilde{\psi}_L^{[i+1]} |$ and holding the remaining ones fixed, one minimizes the cost functional

$$\epsilon^{[i]}[\tilde{\beta}_j^\dagger, \tilde{\beta}_j] = \tilde{\beta}_j^\dagger \tilde{\mathcal{N}} \tilde{\beta}_j - \beta_j^\dagger \mathcal{O} \tilde{\beta}_j - \tilde{\beta}_j^\dagger \mathcal{O}^\dagger \beta_j + \text{const},$$

with $\tilde{\mathcal{N}}$ and \mathcal{O} as defined in Fig. 4.15.

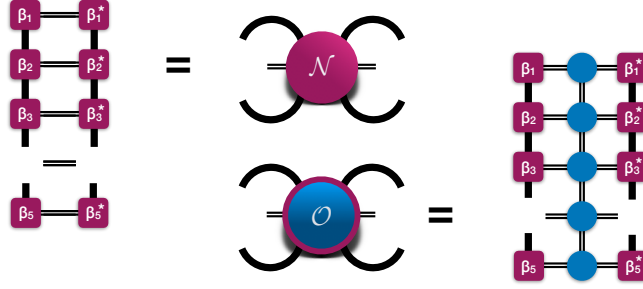


Figure 4.15: Objects $\tilde{\mathcal{N}}$ and \mathcal{O} appearing in the computation of the cost functional for the MPS-MPO contraction scheme.

Since this is a quadratic problem in $\tilde{\beta}_j$, as in the previous section, the optimal solution may be found by computing $\partial_{\tilde{\beta}_j} \epsilon^{[i]}[\tilde{\beta}_j^\dagger, \tilde{\beta}_j] = 0$, which leads to solving the linear system of equations

$$\tilde{\mathcal{N}}\tilde{\beta}_j = \mathcal{O}\beta_j.$$

By restricting the computation to the unitary gauge introduced in Sec. 4.2.4 above, one has $\tilde{\mathcal{N}} = 1$ and thus the solution is simply given by $\tilde{\beta}_j = \mathcal{O}\beta_j$.

Finally, it is worth noting that this approach is not restricted to calculations on systems of a finite size. As a matter of fact, some of the first infinite PEPS calculations were performed employing a scheme completely analogous to the one just described, albeit involving compression moves in all directions. In the case of the infinite system, however, it pays off to perform the contractions using a lattice tilted by 45° , where the computational complexity of the algorithm becomes $\mathcal{O}(\chi^3 D^4)$. See Ref. [106] for further details.

Corner transfer matrix scheme

An alternative approach which has been used quite successfully in infinite PEPS simulations is directly inspired by the CTM scheme presented in Sec. 3.3.1 for classical systems.

As it turns out one may proceed directly as explained in Sec. 3.3.1 even when dealing with quantum systems. However, an alternative procedure which has been found to work quite well in practice was proposed by Corboz in Ref. [107]. When employing the original proposal, as explained in the classical setting, the algorithm exhibits a computational complexity of $\mathcal{O}(\chi^3 D^4)$, whereas in the improved version of Ref. [107] the cost grows to $\mathcal{O}(\chi^3 D^6)$.

4.3.5 Imaginary-time evolution

One of the most widely used approaches used for the optimization of ground-state PEPS wave functions is that of so-called *imaginary-time evolution*. In this approach, by acting with the operator $\exp(-\Delta\hat{H})$ on an arbitrary starting vector $|\psi\rangle$ one may project out all components outside of the ground-state manifold by taking a sufficient number of such evolution steps.

In practice it is necessary to employ a Trotter-Suzuki decomposition [108] in order to break the exponential operator into smaller local gates which may be efficiently applied to the state by fully exploiting the tensor network structure. Even more, to improve convergence, one does not act with a full set of gates simultaneously but, instead, applies each of the gates one at a time.

Several approaches have been developed to perform the evolution at various computational complexities. Here we summarize the three most important ones:

Simple update

In the so-called *simple update*, proposed by Jiang *et al.* in Ref. [109], a rather strong approximation is applied in which one bypasses the effects of the full wave function and, instead, carries out a time evolution which only involves local objects directly affected by the Trotter gate. To compensate for the local nature of the update one employs a poor man's approach in order to incorporate the renormalization effects arising due to distant portions of the wave function, *i.e.*, by introducing a vector of weights on each bond of the wave function one obtains a sort of "mean field" representation for the wave function, see Fig. 4.16.

The insertion of these weight vectors is not fortuitous. They are actually inserted in an attempt at mimicking the effect of working with a canonized MPS and, as a matter of fact, such a "pseudo-canonical" form of a PEPS wave function can be achieved efficiently in (tree-like) Bethe lattices after evolving by a large number of time steps in the asymptotic limit $\Delta \rightarrow 0$.

The optimization procedure itself involves only the tensors directly affected by the Trotter gate as well as those weight vectors surrounding them. This small tensor network is then decomposed via an SVD which truncates the singular values kept and updates the weight vector on the bond optimized by using these singular values, see Fig. 4.16. In this case the optimization may be carried out with an overall computational complexity scaling as $\mathcal{O}(D^5)$, provided that a predecomposition step as in Fig. 4.17 (top left) is introduced and no observables are measured in the process.

As is to be expected, this poor man's approach gives results of intermediate quality which quickly degrade as one approaches states with an extended correlation

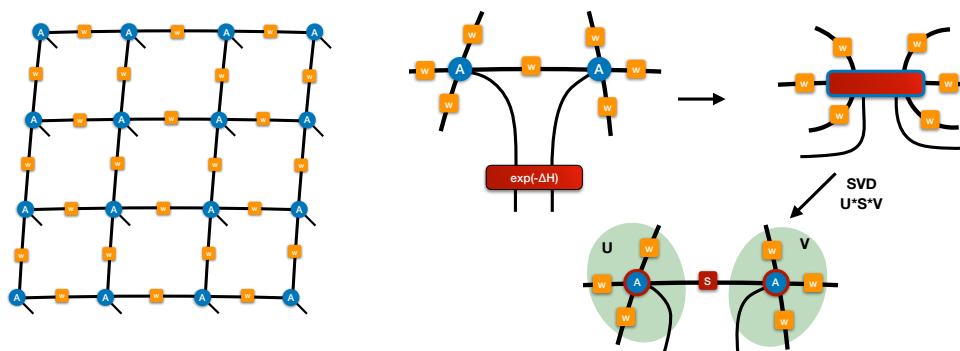


Figure 4.16: Left: illustration of a uniform PEPS *Ansatz* employed with the simple update. Additional weight matrices are illustrated as yellow squares on the bonds of the PEPS. Right: illustration of the simple update procedure explained in the main text. In a first step all weight vectors are loaded on the two tensors involved in the update and the network on the upper left is formed. In the final move an SVD is performed from which the singular values S are used as the new set of weights on the bond being updated.

length, *e.g.*, at critical points.

Full update

In the so-called *full update* [110, 111] one improves upon the simple update by making use of the assumption that the wave functions before and after the Trotter step differ only at the tensors which have been directly affected by a local Trotter gate. Here, unlike in the simple update, the compression of the wave function after acting with the Trotter gate is carried out so as to minimize a *global* cost function, *i.e.*, one employs a cost function analogous to that in Eq. (4.15), adjusted to the setting in which two of the tensors differ between the wave functions.

By using an ALS approach one compresses the wave function by targeting individual tensors at a time. Furthermore, in order to reduce the computational complexity of this optimization, the target tensors are further decomposed via QR/LQ decompositions into smaller objects, as illustrated in Fig. 4.17. Ultimately it is these smaller objects which are optimized at each step and, upon convergence of the ALS procedure, the original PEPS tensors are reconstructed. In this case the tensor $\tilde{\alpha}$, see Fig. 4.17, minimizing Eq. (4.15) is found by solving the linear system of equations

$$\mathcal{N}\tilde{\alpha} = \mathcal{W}\alpha. \quad (4.18)$$

with \mathcal{W} and \mathcal{N} as defined in Fig. 4.17. As we pointed out in Sec. 4.3.2, one may no longer choose a gauge in which the matrix \mathcal{N} becomes an identity. Nevertheless, a proposal by Lubasch, Bañuls and Cirac [111] allows to perform a regauging that, even though not fully allowing to circumvent the computation of \mathcal{N} , has been found to have a very positive impact on its conditioning. In practice, as a consequence of the nature of the contraction schemes employed, the matrix \mathcal{N} tends to lose hermiticity, specially for smaller values of the bond dimension χ . One then employs its closest hermitian approximant $\mathcal{N} \rightarrow (\mathcal{N} + \mathcal{N}^\dagger)/2$. These modifications greatly improve the stability and accuracy obtained in solving Eq. (4.18).

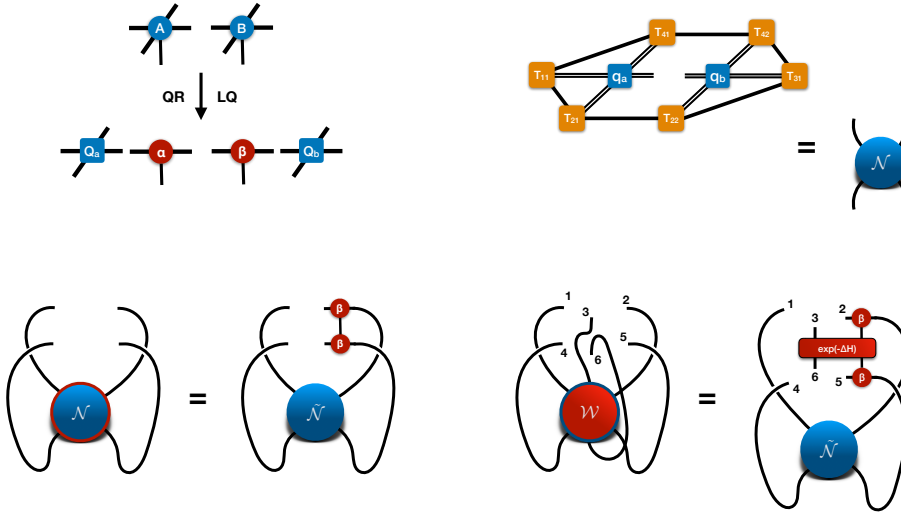


Figure 4.17: Top left: decomposition of tensors A and B into isometries Q_a, Q_b and the smaller tensors α and β . Top right: reduced bond environment where q_a, q_b represent the outer product between Q_a and Q_b and their complex conjugates, respectively. Bottom left: reduced norm network for tensor α . Bottom right: reduced environment network containing the imaginary time evolution gate $\exp(-\Delta\hat{H})$

In this update it is the construction of the bond environments what constitutes the bottleneck of the computation and can be performed using the contraction schemes mentioned above.

Cluster update

In the *cluster update*, proposed in Ref. [112] and denoted as CU_δ , one finds a middle ground in between the very cheap simple update and the expensive full update by obtaining separable representations of the environment tensors up to a certain

distance δ of the sites being optimized. In the case CU_0 one finds a type of update in which one assumes that all environments are separable and is closely connected to the simple-update. The case CU_1 improves on this by adding a single layer of non-separable environments and also allows for a slightly lower computational cost compared to the MPS-MPO scheme presented above. The cases CU_δ with $\delta > 1$ simply approach the limit of the full update without improving the computational scaling of the computation.¹⁰

4.3.6 Variational optimization

Surprisingly, one of the most recent developments for iPEPS has been the introduction of stable algorithms directly targeting the minimization of a PEPS' energy, *i.e.*, targeting the direct minimization of

$$E = \min_{\{A\}} \frac{\langle \psi(\{A\}) | \hat{H} | \psi(\{A\}) \rangle}{\langle \psi(\{A\}) | \psi(\{A\}) \rangle}, \quad (4.19)$$

with respect to the tensors $\{A\}$ making up the PEPS *Ansatz*. This is an important improvement over imaginary time evolution because, as can be easily proved, the convergence rate of the latter depends directly on the magnitude of the energy gap, *i.e.*, should the system exhibit a vanishing energy gap, convergence will be greatly slowed down.

Even though this is a problem which is in principle simple to formulate, its extreme nonlinearity in iPEPS makes it a complex one to address. One of the most recent proposals was put forward in Ref. [113], where it was shown how the CTM contraction scheme presented above can be modified to perform a systematic summation of Hamiltonian terms on infinite systems. As might readily be expected, of all optimization schemes presented, the variational update yields the most accurate results.

Since the essence of the procedure remains the same as that of the original CTM, involving only modifications related to the types of boundary tensors one must keep track of, we redirect the reader to Ref. [113] for a full account of the approach.

This problem has also been addressed in Ref. [114] from an alternative approach in which a conjugate gradient procedure is combined with so-called *channel environments* to perform the optimization. The approach employed therein has the advantage that the energy variance may be computed on-the-fly. Thus allowing one to obtain a direct measure of goodness for a given approximation.

¹⁰These intermediate values actually make the cost slightly higher, yet it has been argued that they may nevertheless be an interesting variant whenever implementing the algorithms using computational parallelism.

4.4 Multi-scale entanglement renormalization Ansatz (MERA)

Within the realm of strongly correlated systems those which exhibit critical behavior occupy a very prominent role. In such a regime a system becomes scale invariant, a reflection of diverging correlations in which entanglement spreads over all length scales in the system. The scaling of entanglement entropy for such systems exhibits a violation of the area law discussed at the beginning of the chapter which, for conformally invariant 1D systems, is of the form

$$S(A) \sim \log(L_A), \tag{4.20}$$

with L_A the length of a subsystem upon bipartition, *i.e.*, such systems exhibit *logarithmic* violations of the area law.

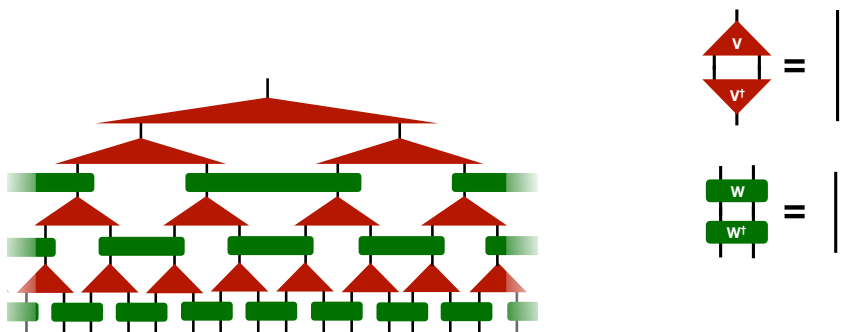


Figure 4.18

From the perspective of tensor networks a very interesting proposal has been developed by Vidal in which he designs a class of tensor networks specifically crafted to simulate systems exhibiting such violations of the area law. This class of states has been dubbed as the *multi-scale entanglement renormalization Ansatz* and they can be understood as quantum circuits performing *entanglement renormalization* [45–47, 62, 115, 116], see Fig. 4.18.

The ability of the MERA to account for this increased growth of entanglement stems from its holographic structure, *i.e.*, the *Ansatz* is designed in such a way that by adding an additional dimension, *i.e.*, a scale dimension, geodesic paths between two local degrees of freedom separated by a distance L involve a number of bonds scaling as $\log(L)$ [117].

This *Ansatz* has been particularly successful at characterizing critical systems, not only because of its favorable entropic properties but also because of its intrinsic efficiency, *i.e.*, just like in the case of MPS, the MERA offers a framework in which observables may be efficiently evaluated *exactly* due to the isometric nature of its components, see Fig. 4.18.

Interestingly, it is also possible to formulate such an *Ansatz* in a scale invariant form, where quantities like the central charge, scaling dimensions as well as operator product expansion coefficients may be extracted efficiently [48, 118, 119]. As this set of quantities can be used to uniquely identify a CFT, the MERA offers a unique tool for the study of lattice realizations of CFTs.

4.5 Conserved quantum numbers

An important concept in the simulation of many-body systems pertains that of symmetries. Indeed, as is well known, the presence of a symmetry enforces a particular structure on both the underlying Hilbert space of the system as well as the Hamiltonian describing its interactions, where these can be organized into so-called *symmetry sectors*, *i.e.*, subspaces invariant under the action of the symmetry operation [120–122].

Symmetries may be separated into those arising due to an invariance of the system under permutation of its components, *e.g.*, *lattice* symmetries, as well as those arising due to the *internal* structure of the local degrees of freedom, *e.g.*, spin rotations about a given axis. They can also arise both at the local (or gauge) as well as global level, *i.e.*, symmetries modifying the state of the whole system.

Within the tensor network framework global internal symmetries play an important role as they can be included in a very systematic manner to speed-up simulations as well as target individual symmetry sectors.

To simplify matters, we shall briefly explain the key idea behind the incorporation of such a symmetry in the particular case of the group $U(1)$, typically associated with the global conservation of particle number $\hat{N}_{tot} = \sum_i \hat{n}_i$ or total spin component $\hat{S}_{tot}^z = \sum_i \hat{S}_i^z$. Our discussion can nevertheless be directly applied to general compact *abelian* groups.¹¹ Below we shall follow the discussion presented in Refs. [123, 125].

Consider a system whose Hamiltonian \hat{H} is invariant under the action of the group $U(1)$, generated by some global operator $\hat{X} = \sum_i \hat{x}_i$. The presence of such a symmetry requires that the many-body Hilbert space admit a decomposition in terms of symmetry-invariant subspaces (sectors) of the form

¹¹The incorporation of symmetries related to *nonabelian* groups is also possible, although significantly more complex. For more information on the subject we refer the interested reader to Refs. [122–124]

$$\mathcal{H} = \bigoplus_{\alpha} V_{\alpha} \quad (4.21)$$

with $V_{\alpha} = W_{\alpha} \otimes d_{\alpha}$ a symmetry sector characterized by a charge α and satisfying $\dim(W_{\alpha}) = 1$, with a potentially nontrivial *degeneracy* space d_{α} .¹² Thus, a generic state in this Hilbert space may be labelled as $|\alpha, t_{\alpha}\rangle$, with $1 \leq t_{\alpha} \leq \dim(d_{\alpha})$.

Now, the key to incorporating such a symmetry into the tensor network framework lies on interpreting the various tensors appearing as symmetry-invariant linear maps between Hilbert spaces.

As an example take the rank-3 tensor T in Fig. 4.19. This tensor may be interpreted as the map $T : V_{a_1} \otimes V_{a_2} \rightarrow V_b$, where the arrows on the tensor are used to distinguish between input and output (dual) spaces. This is an important point as the action of a group element $\exp(-i\varphi) \in U(1)$ on a vector space V is given by the unitary representation $U : \exp(-i\varphi) \mapsto \hat{U}_{\varphi} := \exp(-i\varphi \hat{X})$, whereas the action on the dual space is given by the dual representation $\hat{U}_{\varphi}^{\dagger}$.

One may also consider the action of the symmetry group on the symmetry-invariant tensor T

$$T_{t_{\alpha_1}, t_{\alpha_2}, t_{\beta}}^{(\alpha_1, \alpha_2, \beta)} \mapsto \sum_{t'_{\alpha_1}, t'_{\alpha_2}, t'_{\beta}} (U_{\varphi})_{t'_{\alpha_1}, t_{\alpha_1}} (U_{\varphi})_{t'_{\alpha_2}, t_{\alpha_2}} T_{t'_{\alpha_1}, t'_{\alpha_2}, t'_{\beta}}^{(\alpha_1, \alpha_2, \beta)} (U_{\varphi})_{t'_{\beta}, t_{\beta}}^* \quad (4.22)$$

$$= \exp(-i(\alpha_1 + \alpha_2 - \beta)\varphi) T_{t_{\alpha_1}, t_{\alpha_2}, t_{\beta}}^{(\alpha_1, \alpha_2, \beta)} \quad (4.23)$$

$$= T_{t_{\alpha_1}, t_{\alpha_2}, t_{\beta}}^{(\alpha_1, \alpha_2, \beta)} \quad (4.24)$$

where in the last line we make use of the fact that the tensor is symmetry-invariant. This implies that $\alpha_1 + \alpha_2 - \beta = 0$ for all non-trivial tensor entries, establishing the conservation of the $U(1)$ charge. This is nothing more than a reflection of *Schur's lemma* [122].

In the general case one will have

¹²That the dimensionality of the irreducible representation space W_{α} should satisfy $\dim(W_{\alpha}) = 1$ is a consequence of the fact that we constrain our discussion to abelian groups [122]. This need not be the case for nonabelian groups.

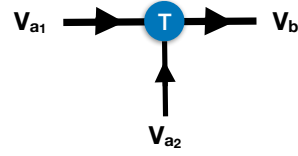


Figure 4.19: $U(1)$ -invariant tensor interpreted as linear mapping between vector spaces $V_{a_1} \otimes V_{a_2}$ and V_b . Labels next to incoming (outgoing) arrows indicate input (output) vector spaces. Such a tensor must obey symmetry constraints, such as the one in Eqs. 4.24.

$$T_{i_1, \dots, i_{k_{in}}, j_1, \dots, j_{k_{out}}} = (T^{\alpha_1, \dots, \alpha_{k_{in}}, \beta_1, \dots, \beta_{k_{out}}})_{t_{\alpha_1}, \dots, t_{\alpha_{k_{in}}}, t_{\beta_1}, \dots, t_{\beta_{k_{out}}}} \delta_{N_{in}, N_{out}} \quad (4.25)$$

with the convention $i = (\alpha, t_\alpha)$, $j = (\beta, t_\beta)$ for input and output indices and $N_{in} = \sum_i \alpha_i$, $N_{out} = \sum_i \beta_i$, with the sums running over all input and output indices, respectively. In writing this expression we interpret $T^{\alpha_1, \dots, \beta_{k_{out}}}$ as the $(k_{in} + k_{out})$ -rank tensor supported over degeneracy spaces. Thus, this expression generalizes the form of a block diagonal matrix ($k_{in} = k_{out} = 1$) to arbitrary rank objects.

In practice, the breaking down of tensors into symmetry blocks entails both memory savings as well as computational savings since now only smaller blocks need be manipulated. This also allows for the possibility of performing various operations, like *e.g.*, contractions and decompositions, on the different symmetry blocks in parallel.

Even beyond the practical advantages of operating with objects of reduced size and allowing for the targeting of specific quantum number sectors, see Fig. 4.19, the conservation of symmetries has played an important role in numerous forms including the characterization of topologically ordered states [126–130].

As we will see in the next section, the conservation of fermionic parity (or particle number) plays a crucial role in the ability to simulate fermionic systems using higher-dimensional tensor network *Ansätze* like PEPS or MERA.

4.6 Fermionic systems

To conclude this chapter we explain how one may employ the framework developed in all previous sections for the simulation of fermionic systems.

4.6.1 Matrix product states

The MPS-based simulation of fermionic systems is most often carried out by employing the so-called *Jordan-Wigner* transformation which allows to map spin degrees of freedom to fermionic degrees of freedom (and vice versa).

Let $\hat{\sigma}_i^+$, $\hat{\sigma}_i^-$, $\hat{\sigma}_i^z$ represent Pauli operators on a chain of spins. One may introduce the objects

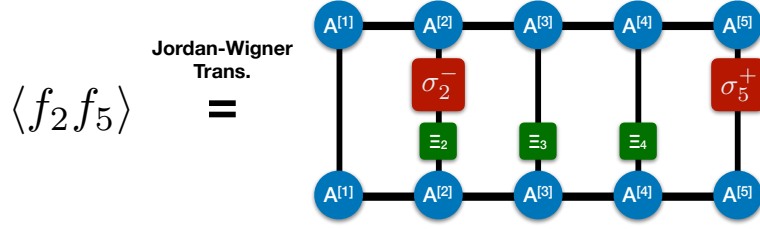


Figure 4.20: The evaluation of a fermionic expectation value can be carried out in MPS language by employing the Jordan-Wigner transformation. This requires the insertion of strings of "filling" operators $\hat{\Xi}_j$, see main text.

$$\hat{\Xi}_j = e^{+i\hat{\sigma}_j^+ \hat{\sigma}_j^-} \quad (4.26)$$

$$\hat{f}_j = \prod_{k=1}^{j-1} \Xi_k \hat{\sigma}_j^-, \quad (4.27)$$

$$\hat{n}_j = (1 + \hat{\sigma}_j^z)/2, \quad (4.28)$$

from which it may be readily verified that one obtains operators $\hat{f}_i^{(\dagger)}$ obeying the canonical fermionic anticommutation relations $\{\hat{f}_i, \hat{f}_j^\dagger\} = \delta_{i,j}$ and zero otherwise.

An important point to note when employing this mapping to simulate fermionic systems arises due to the *non-local* nature of the mapping in terms of strings of $\hat{\Xi}_j$ operators, representing "filling" negative factors controlled by a site's "occupation number" $\hat{\sigma}^+ \hat{\sigma}^-$. What this means in practice is that, in simulating fermionic models, one may employ the same implementation of an MPS code as for distinguishable degrees of freedom, *e.g.*, spins, provided that such strings of filling factors are properly accounted for.

Thus, for example, in evaluating the two-point correlator $\hat{f}_2 \hat{f}_5^\dagger$, see Fig. 4.20, one finds in the spin picture

$$\begin{aligned} \langle \hat{f}_2 \hat{f}_5^\dagger \rangle &= \langle \hat{\Xi}_1 \hat{\sigma}_2^- \hat{\Xi}_1 \hat{\Xi}_2 \hat{\Xi}_3 \hat{\Xi}_4 \hat{\sigma}_5^+ \rangle \\ &= \langle \hat{\sigma}_2^- \hat{\Xi}_2 \hat{\Xi}_3 \hat{\Xi}_4 \hat{\sigma}_5^+ \rangle. \end{aligned}$$

The inclusion of these "filling" factors may be carried out in a straightforward manner whenever employing an MPO-based formulation of the DMRG algorithm.

4.6.2 Higher-dimensional tensor networks

In the case of more generic *Ansätze*, the lack of a 1D structure turns the Jordan-Wigner approach above into a rather cumbersome one. Even more, given that the strings of Jordan-Wigner $\hat{\Xi}_j$ operators will now transform generic local operators in 2D into highly non-local objects, there is no clear picture on which to understand the effect of simulating such objects using tensors network *Ansätze*, *i.e.*, wave functions which have been designed to provide efficient descriptions of ground states of *local* Hamiltonians.

A much more convenient approach has been developed in Refs. [131–134], where it is shown how the introduction of two simple ingredients is enough to account for the effect of the fermionic anticommutation relations giving rise to additional negative signs in fermionic simulations. However, before jumping to the presentation of these ingredients we need some preliminaries. Below we follow the presentation in [132].

The first thing to note is that fermionic models are generically described by *parity-preserving* Hamiltonians. Here by parity we refer to the operator \hat{P} , satisfying $\hat{P}^2 = 1$ (thus providing a \mathbb{Z}_2 quantum number), determining whether a state contains an even or an odd number of fermions. This implies that one may separate the system’s Hilbert space \mathcal{H} into *even* ($\mathcal{H}^{(+)}$) and *odd* ($\mathcal{H}^{(-)}$) components as

$$\mathcal{H} \cong \mathcal{H}^{(+)} \oplus \mathcal{H}^{(-)} \tag{4.29}$$

in which states may now be labelled according to their parity p as $|p, t_p\rangle$, with t_p a degeneracy label, satisfying $\hat{P}|p, t_p\rangle = p|p, t_p\rangle$.

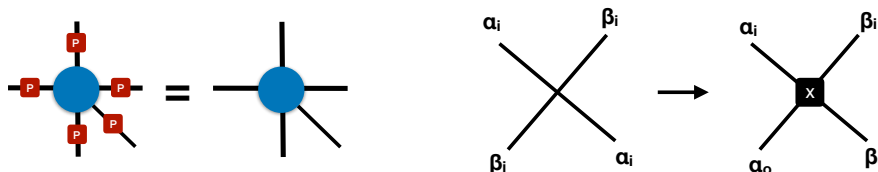


Figure 4.21: Graphical summary of fermionization rules for higher-dimensional tensor networks. Left: \mathbb{Z}_2 -invariant tensor preserving fermionic parity. Right: substitution of index crossings by fermionic swap gates, see main text.

Once the underlying symmetric structure of the many-body space is clear, one may employ all of the techniques discussed in the previous sections simply by applying the following *fermionization rules*

Fermionization Rules

- ▷ fermionic parity shall be preserved exactly, see Fig. 4.21.
- ▷ crossings of indices shall be replaced by fermionic *swap* tensors X satisfying

$$X_{\alpha_i, \beta_i, \alpha_o, \beta_o} = \delta_{\alpha_i, \beta_o} \delta_{\beta_i, \alpha_o} S(\alpha_i, \beta_i),$$

with $S(\alpha_i, \beta_i) = -1$ iff the parity of the states satisfies $p(\alpha_i) = p(\beta_i) = -1$, otherwise $S(\alpha_i, \beta_i) = 1$, see Fig. 4.21.

We conclude this section by directing the interested reader to some of the works [107, 131–133, 135–139] in which this simple set of rules has been employed to simulate various types of fermionic models.

Chapter 5

iPEPS study of the Kitaev-Heisenberg model

In condensed matter physics, the drive behind the exploration of complex quantum systems exhibiting exotic properties stems not only from their intrinsic interest at a fundamental level but also from a very practical perspective. Currently a very active area of research pertains the possibility of employing quantum systems for the implementation of general computing machines, *i.e.*, quantum computers; a possibility initially proposed by Feynman [140] and which many believe to be a promising route towards achieving a (potentially exponential) speed-up over its classical counterpart.

Among the various proposals available, *topological quantum computation* (TQC) [16] has received notorious consideration as one of the most promising approaches towards the development of a quantum computer. In this approach one relies on the peculiar exchange properties of exotic quasi-particles called *anyons* [141–146]. As their name indicates, such excitations need not necessarily fall within the usual classification of fermions or bosons but, instead, the overall phase factor arising as one moves one around another is in general arbitrary.¹ In fact, such excitations can only arise in quasi-particle form in two-dimensional systems, as it is here where the effect of exchanging, or *braiding*, particles is described by the irreducible representations of the braid group and is deeply connected to the topological properties of the system.² As shown by Freedman *et al.* [17], this seemingly simple observation has the powerful consequence that generic computations may be encoded in terms

¹Actually the effect of exchanging two particles need not even result in an overall phase factor. The cases in which it does refer to so-called *Abelian* anyons. In the more general case the irreducible representations of the braid group need not be one-dimensional, thus potentially leading to more complex superpositions. In this case one speaks of *non-Abelian* anyons.

²The term braiding here arises from the fact that the outcome of an exchange of anyons in general depends on the order in which it is performed, so that one may visualize the space-time quasi-particle trajectories as the braiding of thin fibers.

of a highly coordinated braiding of such particles.

Quantum spin liquids (QSLs), *i.e.*, systems made up of (pseudo-)spin degrees of freedom in which strong quantum fluctuations preempt the formation of symmetry-breaking order as one takes the temperature of the system to absolute zero, have been a common target of study in this context. The reason is that, typically arising in (Mott) insulating compounds, the *Lieb-Schultz-Mattis theorem* (and generalizations thereof) [147–149] guarantees that their featureless nature is almost certainly bound to lead to exotic topologically ordered phases. Typical of these phases is the emergence of *fractionalized* excitations obeying anyonic statistics.

One of the most paradigmatic examples of a QSL arises in a model initially proposed by Kitaev [18]. As shown by Kitaev, not only is this model exactly soluble but it also hosts so-called Ising anyons in its spectrum. Given the peculiar nature of its interactions, however, it was long believed that it would remain as nothing more than a theoretical curiosity until a pioneering proposal by Jackeli and Khaliullin [150] made it clear that it might be possible to realize the highly anisotropic interactions in real materials, provided that additional, more conventional, interactions are introduced. This work spurred numerous theoretical proposals where Kitaev's model was extended in various ways in attempts to bridge the physics of the materials to those of the highly sought after model.

In this chapter we shall explore one of these extensions known as the *Kitaev-Heisenberg* model, employing the iPEPS *Ansatz*. Most of the results presented in this chapter have been published in [151].

5.1 Kitaev's honeycomb model

The model originally proposed by Kitaev in Ref. [18] describes a system of $S = 1/2$ spins on a honeycomb lattice interacting via the Hamiltonian

$$H = -J_x \sum_{x\text{-bonds}} \hat{\sigma}_i^x \hat{\sigma}_j^x - J_y \sum_{y\text{-bonds}} \hat{\sigma}_i^y \hat{\sigma}_j^y - J_z \sum_{z\text{-bonds}} \hat{\sigma}_i^z \hat{\sigma}_j^z, \quad (5.1)$$

with each sum running over the subset of bonds labeled by the corresponding type, see Fig. 5.1, and $\hat{\sigma}$ representing the Pauli operators. The Hamiltonian is thus given by highly anisotropic Ising-like interaction terms, each of which couples only the spin components matching the labeling of the bonds on the lattice. As one might already expect the directional nature of the interactions makes this model a strongly *frustrated* one, as there is no simple way of satisfying all interaction terms simultaneously. Indeed, it has been shown that, already at the classical level, the model has a ground-state degeneracy growing exponentially fast with system size [152].

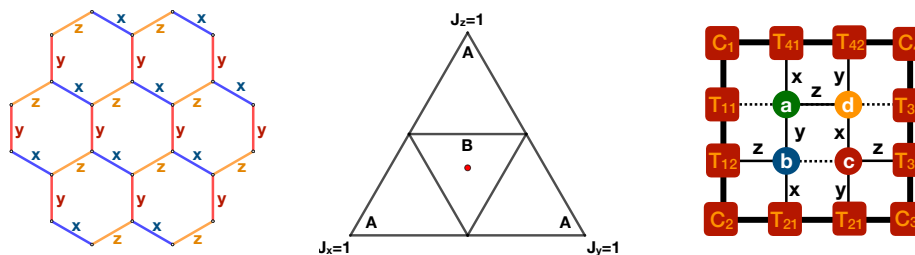


Figure 5.1: Left: labeling of the links of a honeycomb lattice according to Kitaev’s construction. Center: phase diagram of Kitaev’s honeycomb model; the outermost triangle corresponds to the intersection of the plane $J_x + J_y + J_z = 1$ and the positive octant ($J_x, J_y, J_z \geq 0$). Right: unit cell employed for our iPEPS study.

From the form of the Hamiltonian it can be readily verified that it possesses a \mathbb{Z}_2 time-reversal symmetry, corresponding to the mapping $\hat{S} \rightarrow -\hat{S}$, as well as a C_3^* composite symmetry made up of a $2\pi/3$ lattice rotation about any site and a $2\pi/3$ spin rotation about the [111] spin axis, properly reflecting the spatial dependence of the interaction terms.

In the following section, for the sake of brevity, we shall directly state the main results presented by Kitaev in Ref. [18], as well as other relevant results from Ref. [153]. The interested reader is referred to the previous references for a complete account of the beautiful constructions employed in obtaining these results.

5.1.1 Exact Results

As shown by Kitaev, as well as subsequent work [152–154], the model can be mapped to one of Majorana fermions hopping in the presence of static \mathbb{Z}_2 gauge fluxes. The ground-state sector is characterized by having a gauge-flux free configuration and the dispersion relation of the fermions in this flux-free sector is given by

$$\epsilon_{\mathbf{q}} = \pm |f_{\mathbf{q}}| \quad (5.2)$$

with $f_{\mathbf{q}} = 2(J_x e^{iq_1} + J_y e^{iq_2} + J_z)$, $q_1 = \mathbf{q} \cdot \mathbf{n}_1$, $q_2 = \mathbf{q} \cdot \mathbf{n}_2$, and the lattice basis vectors $\mathbf{n}_1 = (\frac{1}{2}, \frac{\sqrt{3}}{2})$ and $\mathbf{n}_2 = (-\frac{1}{2}, \frac{\sqrt{3}}{2})$. As illustrated in the center panel of Fig. 5.1, the model exhibits 4 different phases, characterized by the existence or absence of a finite gap to excitations. The gapped phases are generically called **A** phases whereas the gapless phase (center triangle) is called **B** phase. To determine

the boundary between gapped and gapless phases, one may simply look for lines along which Eq. (5.2) vanishes. It is simple to verify that the conditions

$$\begin{aligned} |J_x| &\leq |J_y| + |J_z|, \\ |J_y| &\leq |J_x| + |J_z|, \\ |J_z| &\leq |J_x| + |J_y|, \end{aligned}$$

determine the region for which the gap is zero. Within this region it can be seen that there are exactly two wave vectors $\pm \mathbf{q}_*$ at which the gap closes.

Follow-up work by Baskaran *et al.* in Ref. [153] showed how it was possible to extract the exact analytical dynamical correlation functions of the model. For the ground state it was shown that the static two-site correlation functions exhibit an extremely peculiar form, *i.e.*, the correlation functions are non-zero if they correspond to spins on neighboring sites and the spin components match the type of the bond joining the spins, where they are given by

$$\langle \sigma_i^\alpha \sigma_j^\alpha \rangle = \frac{\sqrt{3}}{16\pi^2} \int_{BZ} \cos \theta(q_1, q_2) dq_1 dq_2, \quad (5.3)$$

with $\cos \theta(q_1, q_2) = \frac{\text{Re}[f_{\mathbf{q}}]}{|f_{\mathbf{q}}|}$ and $f_{\mathbf{q}}$ as given above.

We shall use these known results in the next section to assess the accuracy of iPEPS *Ansatz* wave functions when simulating the model. This is an important preliminary step on our way to considering additional extensions, as there have been claims in Ref. [155] that the original iPEPS *Ansatz* is incapable of providing an adequate description of the complex ground state of the model, particularly inside the gapless phase. Here we shall provide compelling evidence for the contrary.

5.1.2 iPEPS Benchmarks

For all results below we have employed iPEPS wave functions with the structure shown in Fig. 5.1 where, to simulate the honeycomb lattice, we map it onto a so-called brickwall lattice containing trivial bonds, *i.e.*, bonds on which the PEPS *Ansatz* carries a trivial bond dimension $D = 1$ (dashed lines in Fig. 5.1) and thus do not couple the degrees of freedom on that bond. We have also employed complex arithmetic as these wave functions yielded the best results.

Before diving into the main topic of this chapter, we shall stop to consider the suitability of iPEPS wave functions to provide a proper description of the complex ground state for Kitaev's model. Indeed, since we will only be interested in performing simulations starting from the most challenging point of the phase diagram

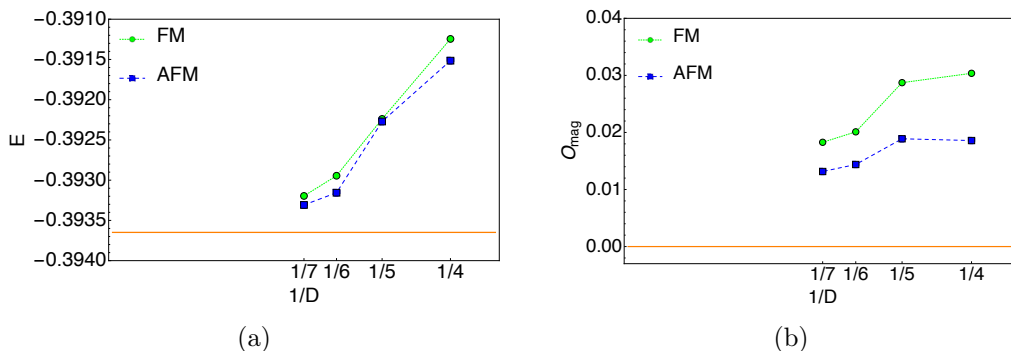


Figure 5.2: Energy per site as a function of inverse bond dimension D in both FM and AFM regimes (left). Order parameter O_{mag} as a function of inverse bond dimension D in both FM and AFM regimes (right).

in Fig. 5.1, *i.e.*, the point $J_x = J_y = J_z = 1$ (red dot), right in the middle of the gapless phase, we shall focus on this location.

We begin by looking at the ground-state energies per site. Given the form of Eq. (5.1) it is possible to directly infer the energy per site from the evaluation of the correlators in Eq. (5.3). By evaluating this expression we find the numerically exact value of $E_0 = -0.3936$. The iPEPS results employing tensors optimized via the full update are presented in Fig. 5.2(a). There it can be seen how, starting from a bond dimension of $D = 4$, as one increases the bond dimension a systematic improvement of the variational energies takes place. The reason we do not show values of the bond dimension $D < 4$ is that, curiously, they failed to converge to a state which could be convincingly placed inside the expected QSL phase. The same was true for all states obtained via the simple update, regardless of the bond dimension employed. This makes it clear that employing the right optimization scheme plays a key role in obtaining proper results. In the end we managed to obtain the energies $E_0^{FM} = -0.3931$ and $E_0^{AFM} = -0.3933$ for the largest bond dimension considered $D = 7$, which provide a relative accuracy of $\Delta E_0^{FM} \sim 0.1\%$ and $\Delta E_0^{AFM} \sim 0.07\%$ at the ferromagnetically and antiferromagnetically coupled points, respectively.

Another element characterizing a QSL are quantum fluctuations strong enough to preclude the formation of, in this case, \mathbb{Z}_2 symmetry-breaking long-range order even at absolute zero temperature. Thus to evaluate this component of our iPEPS wave functions we have considered the root-mean-square value of the local magnetic moments as a measure of this symmetry breaking, *i.e.*, we define the order parameter

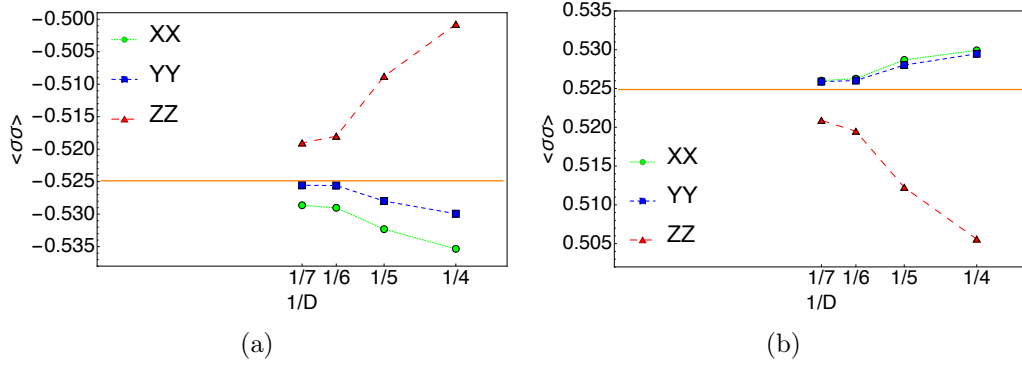


Figure 5.3: Nearest-neighbour correlation functions in the antiferromagnetically coupled (a) and ferromagnetically coupled (b) cases.

$$O_{mag} = \sqrt{\frac{1}{N} \sum_{\alpha \in UC} \langle \hat{\sigma}_\alpha \rangle^2}, \quad (5.4)$$

with $\hat{\sigma}_\alpha$ the Pauli operator at each unit-cell site. The results for both FM and AFM points are shown in Fig. 5.2(b). A strong suppression in O_{mag} is visible for all values of the bond dimension considered. For the FM coupled data we find a maximum of 0.03 at $D = 4$ with a subsequent suppression to a value of 0.017 at $D = 7$. On the other hand for the AFM coupled data we find a maximum of 0.02 at $D = 4$ with a subsequent suppression to a value of 0.012 at $D = 7$. Together with the systematic reduction in symmetry-breaking as the bond dimension is increased, these results provide a clear signature of the vicinity of our wave functions to a QSL phase.

Finally, owing to the extremely peculiar form of the spin correlators in the ground state of the model, we have obtained additional signatures of the vicinity of our wave functions to a putative Kitaev QSL phase by looking at the local correlation functions. The results are shown in Fig. 5.3. By evaluating Eq. (5.3), it is readily verified that a value $\langle \sigma_i^\alpha \sigma_j^\alpha \rangle \approx 0.525$ is to be expected for neighboring sites for which the bond type label matches the spin component α . We find that our results indeed systematically approach this value as the bond dimension is increased. It should be mentioned that the XX and YY correlators exhibit a curious deviation with respect to the ZZ correlators. This is an artificial breaking of the $\frac{2\pi}{3}$ composite symmetry mentioned above, arising purely as a numerical artifact of the way we map the honeycomb lattice onto a brickwall lattice for the construction of the CTM environment tensors. Importantly, this feature is systematically reduced as we increase the number of variational parameters in the wave functions and the environments.

At this point it should already be fairly clear that obtaining an adequate description

of the Kitaev QSL phase is possible via iPEPS wave functions. Even though it should still be possible to improve the quality of the approximations further by increasing the value of the bond dimension, *i.e.*, the number of variational parameters, the computational cost of doing so would have taken a prohibitively long time.

5.2 Kitaev-Heisenberg model

As mentioned in the introduction, a large part of the motivation behind the study of QSL phases arises from the possibility of their realization in real materials.

A family of materials which has received substantial attention over recent years [156–165] corresponds to the so-called *Iridates*, *i.e.*, compounds of the form $A_2\text{IrO}_3$ ($A = \text{Na, Li}$), in which a sizeable charge gap together with a strong spin-orbit coupling lead to an effective description of the active t_{2g} orbitals of Ir^{4+} ions in terms of Kramers-doublet pseudospin-1/2 degrees of freedom arranged on a honeycomb lattice.

A very interesting proposal was put forward by Chaloupka *et al.* in Ref. [166] based on the *Kitaev-Heisenberg model* (KHM) of Ref. [167] yet extended to its full parameter space, *i.e.*,

$$H_{i,j}^{(\gamma)} = A \left(\cos \varphi \mathbf{S}_i \cdot \mathbf{S}_j + 2 \sin \varphi S_i^{(\gamma)} S_j^{(\gamma)} \right), \quad (5.5)$$

with (i, j) labeling nearest-neighbor sites of a honeycomb lattice, the first term being an isotropic Heisenberg interaction, the second an anisotropic Kitaev interaction in which $\gamma \in (x, y, z)$ determines the spin components interacting along a given bond, $\varphi \in [-\pi, \pi)$ and A an overall scaling factor which we set to one.

5.2.1 Previous work

This model has been tackled in the past using a variety of approaches in different regions of its full parameter regime [155, 166–169]. In its original formulation (covering only the region $\varphi \in [-\pi/2, 0]$) small system studies [167, 169] found either a second or weak first order phase transition joining a QSL phase to a so-called stripy phase at roughly $\varphi \approx -76^\circ$ (or $\alpha \approx 0.8$ in the original formulation), see Fig. 5.1. This value is also reported in the extended formulation on a 24-site system [166]. The restricted formulation was also studied from a slave-particle mean-field approach in Ref. [168] where the behavior of the order parameter showed a discontinuity at a value of $\varphi \approx -72^\circ$ ($\alpha \approx 0.76$). There it was nevertheless suggested that the transition could end up being of either second or weak first-order type, upon inclusion of quantum fluctuations beyond the mean-field level.

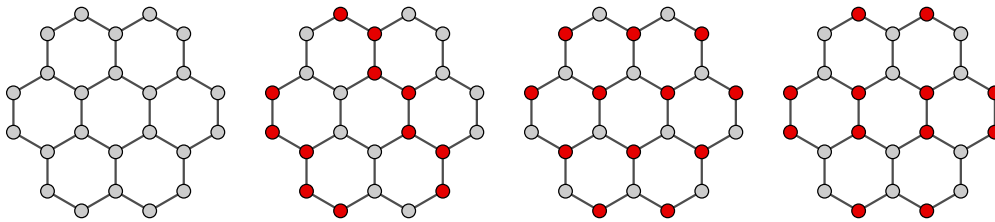


Table 5.1: Schematic representation of the various phases found in the phase diagram of the Kitaev-Heisenberg model. Circles of equal (different) color represent spins aligned (anti-)parallel to each other. From left to right: ferromagnetic, zigzag, Néel and stripy orders.

Finally, a so-called mixed PEPS (mPEPS) approach in Ref. [155] found a phase transition at $\varphi \approx -89^\circ$ ($\alpha \approx 0.99$) or, perhaps more precisely, it was found that the QSL phases did not have a finite span in the thermodynamic limit.

5.2.2 iPEPS approach

Here we will be interested in studying the extension of Kitaev's model given by Eq. (5.5). The interest in employing the iPEPS algorithm arises due to various reasons: first, the algorithm is formulated directly in the thermodynamic limit, allowing it to overcome limitations due to the intrinsically small system sizes available from ED and MPS studies previously employed; second, since the bond dimension, representing the only refinement parameter in the *Ansatz*, can be seen as a measure of the amount of entanglement encoded by the wave function, by systematically increasing its value we may monitor the effect of introducing additional correlations beyond the mean-field level, given by the value $D = 1$, thus providing insights beyond those from the previous slave-particle mean-field approaches.³

More specifically, we will be concerned with addressing the following open questions: do the QSL phases survive in the thermodynamic limit? and, if they do, what type of phase transition leads to the various phases found beyond the Kitaev QSL phases?

In order to tackle these questions we will employ the following approach. First, a rough idea of the phases present and their locations may be obtained by performing an optimization of the iPEPS wave functions around the full parameter range $\varphi \in [-\pi, \pi)$. Once these phases have been identified, we address both questions

³Here it should nevertheless be emphasized that the way iPEPS approaches the mean-field level is not expected to be equivalent to the approach in Ref. [168], where the slave-particle formulation employed allowed for an adequate representation of the Kitaev QSL phases. Indeed, as mentioned in the previous section, we were not able to find good QSL phase representatives below $D = 4$.

above simultaneously by letting each phase compete, *i.e.*, by choosing tensors representative of each neighboring phase and optimized far away from a potential transition point, we carry out additional optimization steps for a range of values of φ across the expected phase transition using these representatives as initial states. This provides an initial bias for each optimization. Then, should the QSL energies remain lower than those of the competing phases across a finite range of φ values, one obtains strong evidence for the survival of the QSL phase in the thermodynamic limit. At the same time one may observe the behavior of the energy curves as φ is varied, so that in the case of a first-order phase transition the metastability of the competing phases in the close vicinity of the transition should allow us to observe an energy crossing. On the other hand, should the competing energy lines meet at a vanishing angle, we will have evidence for a continuous phase transition. These observations can of course be complemented with measurements of various order parameters, which should also exhibit clear signatures of the type of transition.

5.2.3 Results

In their proposal Chaloupka *et al.* [166] performed a 24-site Lanczos diagonalization study of this model in which 6 different phases were identified, namely: antiferromagnetically coupled QSL (ASL), ferromagnetically coupled QSL (FSL), Néel, stripy, ferromagnetic and zigzag, see Fig. 5.1. We have found the same phases using iPEPS and we show an overview of the full phase diagram found in our study in Fig. 5.4.

In the study by Chaloupka *et al.* the phase transitions between symmetry broken phases (stripy/Néel and ferromagnetic/zigzag) were found to be of first-order, whereas the FSL to ordered transitions were found to be of either second or weak first-order. In the case of the ASL phase, the nature of the transitions to the ordered zigzag and Néel phases was not directly identified but observed to correspond to level crossings, thus pointing towards first-order-type transitions.

Here, in order to capture the different types of magnetic order we define four additional order parameters, *i.e.*,

$$O_{ferro} = \sqrt{\frac{1}{4} (\langle \sigma_a \rangle + \langle \sigma_b \rangle + \langle \sigma_c \rangle + \langle \sigma_d \rangle)^2}, \quad (5.6)$$

$$O_{stripy} = \sqrt{\frac{1}{4} (\langle \sigma_a \rangle - \langle \sigma_b \rangle - \langle \sigma_c \rangle + \langle \sigma_d \rangle)^2}, \quad (5.7)$$

$$O_{zigzag} = \sqrt{\frac{1}{4} (\langle \sigma_a \rangle + \langle \sigma_b \rangle - \langle \sigma_c \rangle - \langle \sigma_d \rangle)^2}, \quad (5.8)$$

$$O_{Néel} = \sqrt{\frac{1}{4} (\langle \sigma_a \rangle - \langle \sigma_b \rangle + \langle \sigma_c \rangle - \langle \sigma_d \rangle)^2}, \quad (5.9)$$

with each of them being designed to identify the different types of order expected inside different regions of the phase diagram. Any form of symmetry breaking

beyond those captured by these four order parameters should be visible through a finite O_{mag} , see Eq. 5.4.

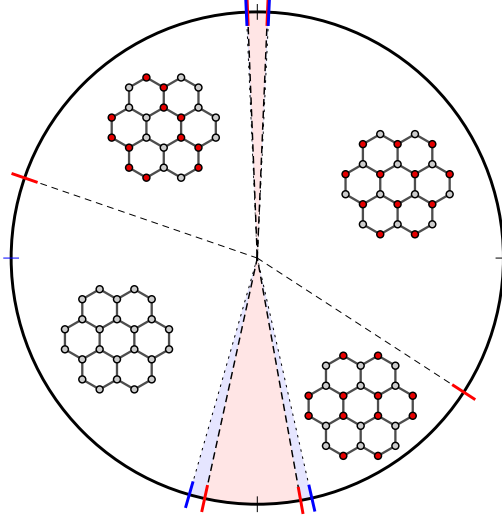


Figure 5.4: Regions spanned by the different phases found using iPEPS. Four different magnetically ordered (collinear) phases are found: Néel (top right), zigzag (top left), ferromagnetic (bottom left) and stripy (bottom right). Magnetically ordered phases are characterized using the order parameters in (5.4)-(5.9). Regions shaded in red correspond to the spin liquid phases. Phase boundary angles corresponding to $D = 6$ are indicated by red thick lines on the edge of the circle. Phase areas and transition angles found by a $1/D \rightarrow 0$ extrapolation are indicated by the blue shaded regions and blue thick lines.

FSL-Stripy transition

In order to illustrate the procedure proposed above let us consider the region corresponding to FM Kitaev couplings and AFM Heisenberg couplings defined by $\varphi \in [-90^\circ, 0]$. After a preliminary set of runs we find 3 different phases in this quadrant: FSL, stripy and Néel as one moves from $\varphi = -90^\circ$ to $\varphi = 0$. Noting that this matches the results from previous studies [155, 166–169] it remains to verify how our results agree with the transition points found previously. Having obtained tensors representing the phases at the two extremes of the angle window shown in the top panel of Fig. 5.5, we perform imaginary-time evolution on these states for all values of φ in this window.

There an energy crossing at a finite angle is clearly observed for a value of $\varphi \approx -80^\circ$ with $D = 6$. From the arguments presented above we believe that this represents

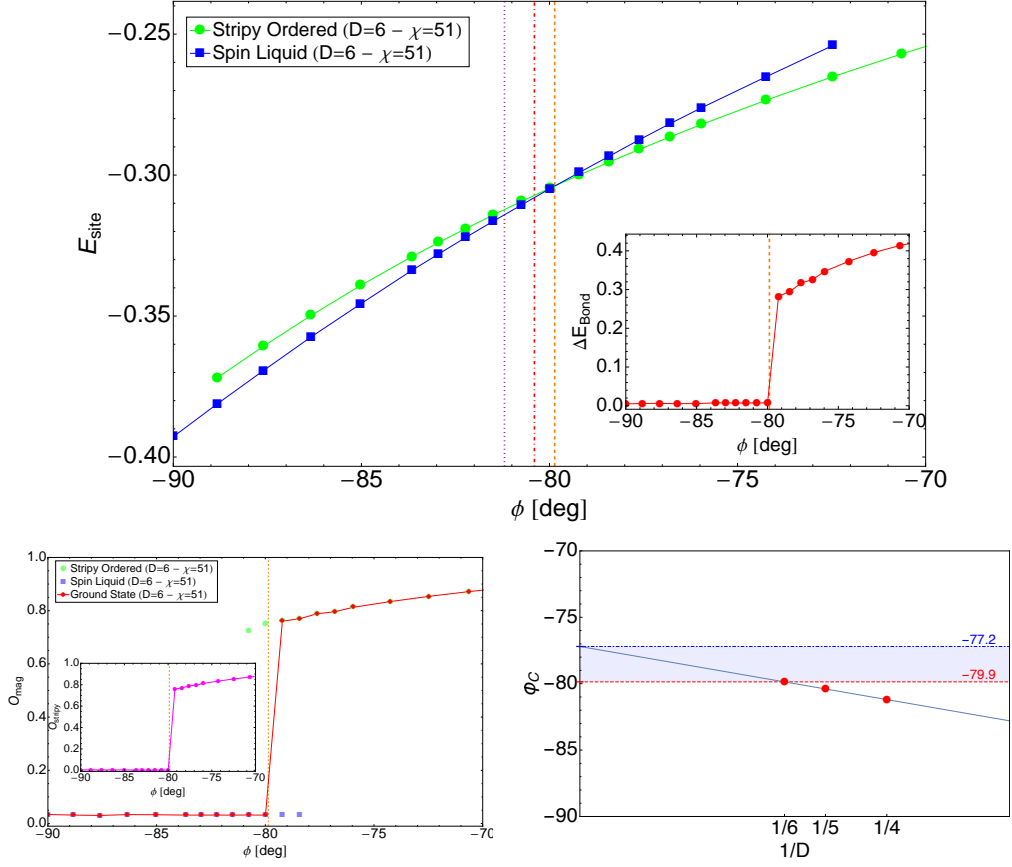


Figure 5.5: Top: Energy crossings for the FSL to stripy phase transition. Dotted (Purple), Dash-Dotted (Red) and Dashed (Orange) lines correspond to the location of the phase transition for $D = 4, 5, 6$, respectively. The inset shows the maximum deviation of the bond energies from the mean value normalized to the mean value. Bottom left: O_{mag} within each phase (green circles: stripy / blue squares: FSL) and the reconstructed ground state curve (red diamonds). The inset shows the behavior of O_{stripy} over the same range of angles. Order parameters are normalized to one. Dashed orange lines indicate the estimated location of the phase transition for $D = 6$. Bottom right: linear extrapolation of the phase boundary in the limit $1/D \rightarrow 0$.

an actual level crossing in the system. Moreover, the magnetization data shows a pronounced jump consistent with a first-order phase transition, see bottom left plot in Fig. 5.5. Here all order parameters remain remarkably close to zero within the $\varphi \in [-90^\circ, -80^\circ]$ range, as expected for the FSL, and a jump in both O_{mag} and O_{stripy} occurs as the energies of the FSL and stripy phases cross, indicating a transition into a stripy ordered phase. In the upper inset in Fig. 5.5 we show the relative deviation in bond energies from the average value and here a jump is also

visible. Similarly, the transition between symmetry-broken stripy and Néel phases is found to be of first-order and located at $\varphi \approx -33^\circ$ (data not shown).

We note here that the phase boundary systematically shifts towards smaller values of φ (in norm) as we increase the bond dimension D , effectively increasing the size of the FSL region. A linear extrapolation in $1/D$ to the $D \rightarrow \infty$ limit yields a phase boundary at $\varphi_\infty \approx -77^\circ$, very close to the value found in previous studies [166, 167, 169], *i.e.*, $\varphi \approx -76^\circ$ (or $\alpha \approx 0.8$ in the original parametrization [167]), see bottom right panel in Fig. 5.5. As there is no clear argument for the validity of such an extrapolation, we quote the transition values for $D = 6$ in Tab. 5.2 and interpret this value as a *lower bound* for the extent of the FSL phase on this part of the phase diagram. We will do this consistently in all cases below.

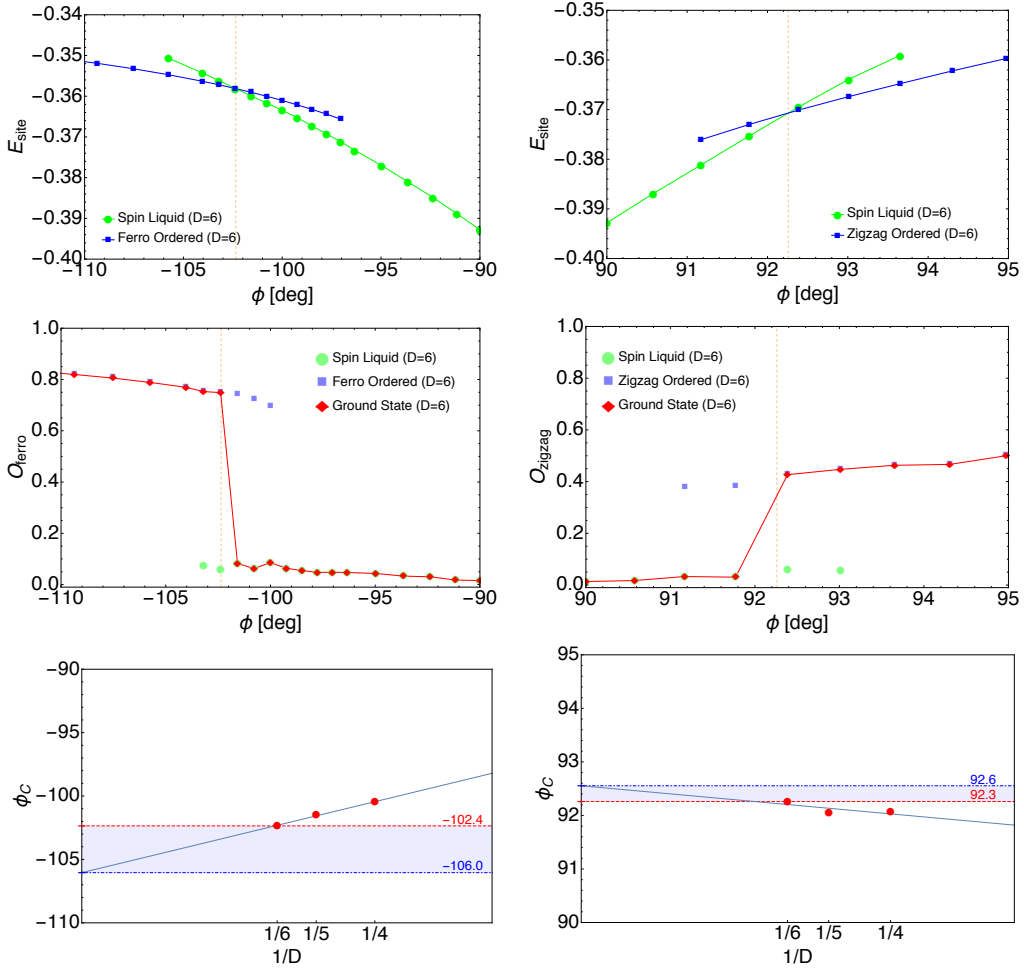


Figure 5.6: Data for the FSL to Ferro (left column) and the ASL to Zigzag (right column) phase transitions. Top: energy crossing, middle: order parameters, bottom: linear extrapolation of the phase boundary in the limit $1/D \rightarrow 0$.

FSL-Ferromagnetic transition

Keeping the sign of the couplings for the Kitaev term fixed and flipping the interaction from AFM to FM for the Heisenberg term (this puts us in the third quadrant of the phase diagram, see Fig. 5.4) we find two phases: ferromagnetic and FSL, with the phase boundary being located at $\varphi \approx -102^\circ$ for $D = 6$ and a $D \rightarrow \infty$ extrapolated value of $\varphi_\infty \approx -106^\circ$. An energy crossing at a finite angle together with a discontinuity in the order parameters O_{mag} and O_{ferr} of comparable magnitude to that of the FSL-stripy transition again indicate that this is a first-order phase transition, see left panels in Figs. 5.6 and 5.8.

ASL-Zigzag transition

Switching the character of the interaction of the Kitaev term to AFM brings us to the second quadrant of the phase diagram where we find 3 phases: ferromagnetic, zigzag and ASL with the zigzag phase in between the ASL and ferromagnetic phases, see Fig. 5.4. The transition from ASL to zigzag is located at $\varphi \approx 92^\circ$ with $D = 6$ (a $D \rightarrow \infty$ extrapolation increases this value only very slightly to $\varphi_\infty \approx 93^\circ$), see right panels in Fig. 5.6, whereas that from ferromagnetic to zigzag is found to be at $\varphi \approx 161^\circ$. These transitions also exhibit energy crossings at finite angles with the angle (strength of the transition) being significantly enhanced between the symmetry-broken phases. Discontinuities in the order parameters O_{mag} / O_{zigzag} in the first case (see the right panels in Fig. 5.6) and O_{ferro} / O_{zigzag} in the second (data not shown) again allow us to infer that these transitions are of first-order type.

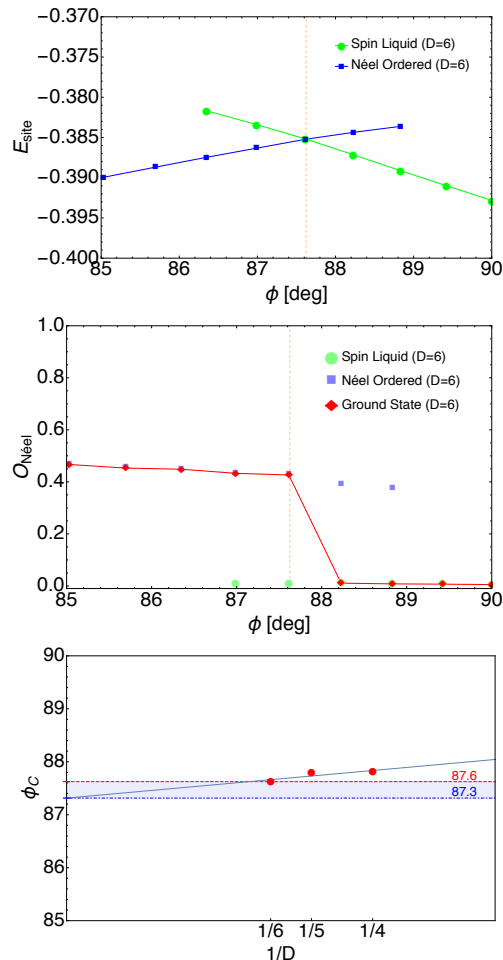


Figure 5.7: Energy crossings (top), O_{mag} (middle) and $1/D \rightarrow 0$ extrapolation of the phase boundary (bottom) for Néel and spin liquid phases.

ASL-Néel transition

Finally, in the regime with all antiferromagnetic couplings $\varphi \in [0^\circ, 90^\circ]$, we find two phases: ASL and Néel. The phase transition is located at $\varphi \approx 88^\circ$ with $D = 6$ (extrapolating $D \rightarrow \infty$ again brings only a very slight lowering to $\varphi_\infty \approx 87^\circ$) and an energy crossing at a finite angle together with discontinuities in $O_{mag} / O_{Néel}$ tell us that this transition is of first-order type as well, see Fig. 5.7. Here the magnitude of the jumps in the ASL-Néel and ASL-zigzag cases is considerably weaker than in the lower half of the phase diagram, see Fig. 5.8.

As noted previously in Ref. [167], the regions corresponding to Néel and zigzag phases are connected via a four-sublattice transformation. The same transformation connects the stripy phase to the ferromagnetic phase. As is well known, stronger quantum fluctuations in the Néel phase lead to a suppression in the order parameters compared to the ferromagnetic phase thus yielding weaker discontinuities in the phase transitions in the upper half of the phase diagram as compared to those found in the lower half. These features are nicely reflected in the order parameters shown in Fig. 5.8 as their magnitudes at the phase transition points match quite well.

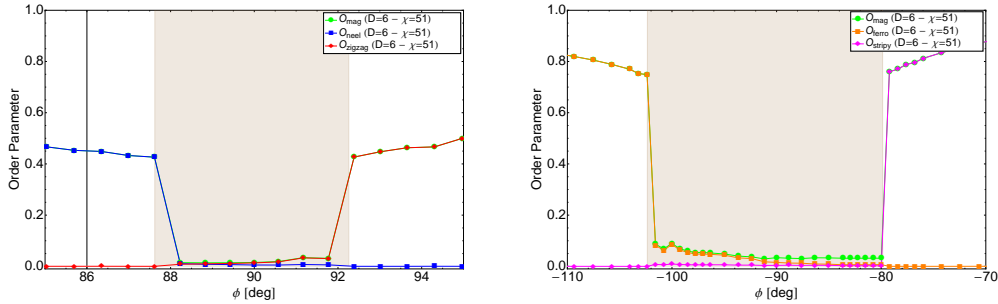


Figure 5.8: Order parameters as a function of the angle φ in the vicinity of the points $\varphi = \pm 90^\circ$, normalized to 1. Regions of strongly suppressed symmetry breaking are clearly visible in both cases with finite discontinuities in the order parameters. The shaded regions indicate the estimated extents of the regions covered by the QSL phases. All order parameters not shown remain very close to zero.

We summarize the most important results found in Figs. 5.4 and 5.8.

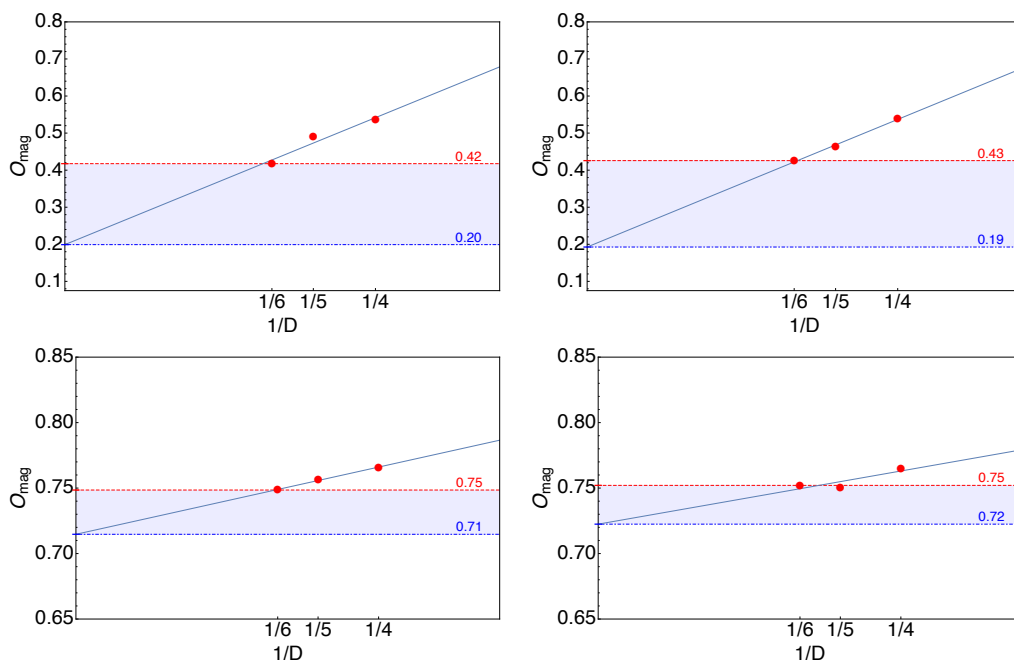


Figure 5.9: Order parameters O_{mag} as a function of inverse bond dimension D at the various phase transitions, normalized to 1. Blue continuous lines correspond to linear fits to the data. Red lines (dashed) correspond to the $D = 6$ values whereas blue (dot-dashed) lines correspond to the value extrapolated to $1/D \rightarrow 0$. The blue shaded area highlights the region where the true value of the order parameter is expected to lie in the thermodynamic limit.

5.3 Discussion

In summary, in the case of the spin liquid with antiferromagnetic couplings we found evidence of first-order phase transitions into symmetry-broken Néel and zigzag phases for finite values of the bond dimension D , in terms of energy crossings at finite angles as well as discontinuities in the order parameters. As can be seen in Fig. 5.9 a considerable suppression of the discontinuity takes place as additional entanglement is introduced by growing the bond dimension D . This suggests that, in contrast to the situation on the lower half of the phase diagram, these transitions are likely to become weak first-order transitions in the thermodynamic limit.

In the case of the spin liquid with ferromagnetic couplings we have also found evidence for first-order phase transitions leading to ferromagnetic and stripy ordered phases, in contrast with results from previous small system studies [166, 167, 169], and a reduced extent compared to these previous results. As shown in Fig. 5.9 the behavior of the order parameters as D is increased is highly suggestive of finite discontinuities, even in the limit $1/D \rightarrow 0$, thus providing significant evidence for

the first-order nature of these transitions in the thermodynamic limit.

Given that the phase boundaries showed a systematic shift as a function of D effectively increasing the size of the QSL phases, as shown in Figs. 5.5, 5.6 and 5.7, we conclude that our $D = 6$ results correspond to lower bounds. This means that upon increasing the bond dimension in our *Ansatz* beyond $D = 6$ we expect the FSL to span at least a region $\varphi \in [-102^\circ, -80^\circ]$, whereas the ASL is expected to cover at least the region $\varphi \in [88^\circ, 92^\circ]$. The effect being more noticeable in the former case can be related to the nature of the competing phases (ferromagnetic and stripy) allowing the ferromagnetic spin liquid phase to profit more effectively from additional quantum fluctuations introduced as the bond dimension is increased.

Support for our estimates of the location of the phase transitions and their first-order nature has been provided more recently by iDMRG studies of the KHM on infinite cylinders [170], where stronger discontinuities for the transitions between the FSL and the ferromagnetic/stripy phases compared to those between the ASL and the zigzag/Néel phases are also found.

As mentioned in Sec. 5.2.1, the possibility of a first-order phase transition between the FSL and the magnetically ordered phases was discussed in Ref. [168]. There it was discussed how, within a slave-particle mean-field formulation, the transition could be one between a \mathbb{Z}_2 spin liquid and a (gapped) $U(1)$ spin liquid in which, due to nonperturbative effects, an immediate confinement of the spinons in the \mathbb{Z}_2 phase directly leads into a magnetically ordered phase.

A significant difference between our results and those in Ref. [168] corresponds to the magnitude of the discontinuity observed, where in our simulations we find a discontinuity in the magnetic order parameters about twice as large as the one observed in Ref. [168], even after $1/D \rightarrow 0$ extrapolation. Given that our *Ansatz* properly captures the various phases, it is highly unlikely that a sudden jump, weakening the discontinuities, arises for larger values of the bond dimension D . One final possibility relates to the intrinsic rigidity of employing fixed-size iPEPS unit cells. Such a rigidity should be particularly visible at first-order phase transitions, where the system may not freely nucleate as the transition happens.

	iPEPS	Lanczos
ASL - Néel	88°	88°
ASL - Zigzag	92°	92°
FSL - Stripy	-80°	-76°
FSL - Ferro	-102°	-108°
Ferro - Zigzag	161°	162°
Stripy - Néel	-33°	-34°

Table 5.2: Left: transition points found using iPEPS with a bond dimension $D = 6$. Right: 24-site Lanczos results from Chaloupka *et al.* [166].

Chapter 6

Infinite projected entangled-pair states on cylinders

One of the main forces driving the area of TNAs stems from the remarkable success of the DMRG in the simulation of 1D lattice models. This success, as we discussed in Ch. 4, is essentially a consequence of the property that ground states of gapped and local 1D Hamiltonians both obey an area law of entanglement entropy as well as admit an efficient representation in terms of MPS.

Perhaps most notorious is the fact that the class of MPS has been repeatedly found to provide very accurate results even when studying, *e.g.*, critical systems [171–175], in which the closing of the energy gap leads to a spreading of correlations over all length scales in the system, or 2D systems [22, 176–178], where an area law can no longer be used to certify the efficiency of MPS. As a consequence MPS represent not only the golden standard for the simulation of 1D lattice models, but also one of the most competitive algorithms for the simulation of strongly-correlated 2D systems.

In the realm of 2D TNAs, and even though significantly younger than MPS, (i)PEPS have already shown considerable promise as a competitive algorithm for the simulation of strongly-correlated systems, with notable achievements including some of the lowest variational energies and important insights into the physics of the t - J [107, 135], Hubbard [136], as well as various frustrated spin models [151, 179–189] in the thermodynamic limit.

Even though numerous studies have made it clear that the class of MPS provides a very competitive approach for the simulation of strongly-correlated systems, even beyond 1D, the fact that generic ground states of systems in higher dimensions impose heavier requirements on the amount of entanglement an *Ansatz* wave function must be able to encode, poses serious questions to the scalability of MPS as the method of choice for their study.

To get an idea of the actual numbers one might consider a value of $D = 4$, which is well within the limits of what is currently reachable in a numerical simulation, and a width of $W = 10$. This gives $m = 1.048.576$, a value vastly exceeding what is currently feasible using state-of-the-art implementations of the DMRG algorithm. Thus, in light of this simple entropic argument, it might appear obvious what the method of choice should be whenever simulating 2D systems. However, as we have remarked in Sec. 4, PEPS simulations do not inherit certain advantageous features, related to numerical stability and computational complexity, present in MPS simulations, *e.g.*, the difference in computational scaling $O(m^3)$ vs. $O(D^{10-12})$ allowing for substantially larger value of m or the ability to generically choose a unitary gauge, making it difficult to predict their relative performance based on such a naive argument.

A few questions thus naturally begin to arise, namely: is it possible to employ PEPS wave functions as a complementary approach once entropic demands start becoming prohibitively large for MPS simulations on 2D systems? If so, for which system sizes should this takeover begin to happen?

6.1 Previous work

The case of computations on infinite cylindrical geometries has received reduced attention¹ with a lot of the work focused on the extraction of topological information [128, 193, 194] in which case the computations may be carried out using cylinders of infinite width, which allow for convenient simplifications, or using exact contractions of cylinders with modest widths. The case of numerical simulations on cylinders with an *arbitrary* finite width has, to the best of our knowledge, received no attention to date.

One may conceive a number of reasons as to why PEPS have received little attention over time for the simulation of semi-infinite cylinders. A first reason one may imagine arises from the fact that the inclusion of the tensor indices corresponding to the PBC can lead to an increase in computational complexity of the, already rather expensive, algorithms. Another reason pertains the numerical stability of the computations. Recall that the formulation of the algorithms on systems with open boundary conditions (OBC) is typically performed in a way completely analogous to MPS simulations for finite systems, so that in contracting the network for the norm $\langle \psi | \psi \rangle$, one may impose the unitary gauge introduced in Sec. 4.2, ensuring the stability of the computations. However, extending this approach to systems with periodic boundaries employing a PBC MPS boundary representation would prevent one from imposing the unitary gauge, thus compromising the numerical stability of the computations. Alternatively, should one insist on employing an

¹Specializations of the iPEPS algorithm to ladders of reduced width, *i.e.*, $W \leq 3$, have been considered in [191, 192]. These, however, do not scale well to arbitrary width cylinders.

OBC MPS boundary description, this representation will be subject to considerably larger entanglement requirements. The reason being that a direct OBC MPS representation of the boundary would require the "folding" of the PBC PEPS indices along the bulk, thus resulting in a squaring of the PEPS bond dimension along the direction parallel to the boundary and, presumably, an increase of the corresponding bond dimension for the MPS boundary representation. Given that it is the boundary construction that poses the main bottleneck in PEPS simulations, such an increase could render the algorithm essentially unusable.

In the following section we will evaluate various approaches in order to better understand what the best way of proceeding is, when carrying out PEPS simulations on cylinders.

All results below represent original work by the author unless otherwise specified.

6.2 Contraction schemes

Given the lack of progress in our current setting, the first question to be addressed is: how can a proper description of generic boundary fixed points be obtained? In this section we will be exclusively concerned with this question.

Since, given the nature of the problem, it is possible to "cook-up" a very large number of heuristic approaches to formulate the iPEPS algorithms on cylinders, here we shall discuss only a few of the most reasonable possibilities. As we shall see some of these may be rapidly disposed of based on simple arguments, and so we will touch upon them only so briefly.

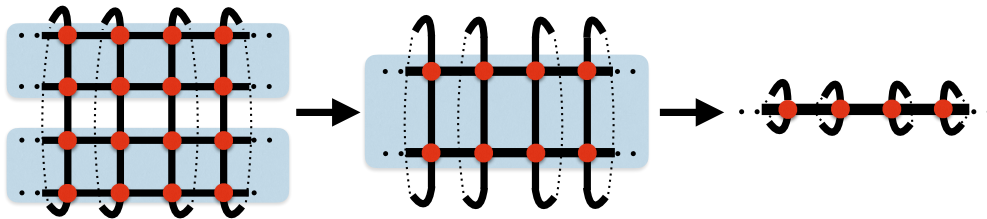


Figure 6.2: Illustration of a scheme in which one coarse-grains the iPEPS to width where it can be contracted exactly. As in this scheme one starts to approach an MPS description, the horizontal bond dimensions will likely need to scale exponentially with coarse-graining iteration.

6.2.1 Width-reduction scheme

As a first attempt one could try to reduce the width of the cylinder by obtaining an effective description in terms of a narrower cylinder for which an exact contraction of the boundary can be carried out exactly. This could be achieved, *e.g.*, simply by formulating coarse graining operations along the finite dimension of the cylinder, as in Fig. 6.2, in such a way that only a maximum number of degrees of freedom, *i.e.*, a maximum bond dimension, are kept as one coarse grains the lattice.

This approach has a very fundamental shortcoming: in trying to effectively reduce the width of the PEPS *Ansatz* we start to approach an MPS description. This means that for this approach to remain effective, the bond dimension of the reduced PEPS tensors along the horizontal direction would potentially have to scale exponentially with the number of coarse graining steps. Thus, such an approach would effectively take us back to the original problem we found when employing MPS encodings of 2D wave functions.

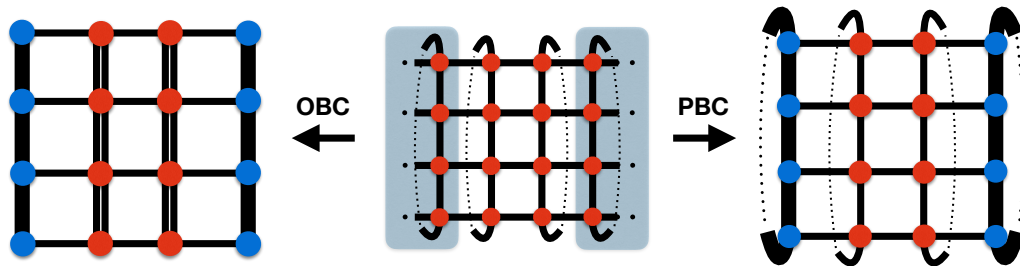


Figure 6.3: Illustration of two possible ways of mapping an iPEPS wave function on an infinite cylinder. One may choose to preserve translation symmetry along the vertical axis by employing a PBC MPS (blue tensors) representation of the system (right) or break this symmetry artificially by employing an OBC MPS(left).

6.2.2 OBC-MPS scheme

In this scheme we attempt to obtain boundary fixed point descriptions by employing OBC MPS encodings. To do this one must first perform a folding of the PEPS indices along the boundaries, see Fig. 6.3, in order to obtain a PEPS transfer matrix resembling that in a ladder/slab geometry. Using this representation we may then employ the technique explained in Sec. 4.3.4 to obtain the boundary fixed points.

This approach inherits the numerical stability provided by the ability to enforce the unitary gauge presented in Sec. 4.2. It is nevertheless important to note that it also entails an artificial breaking of translation symmetry, potentially removing one

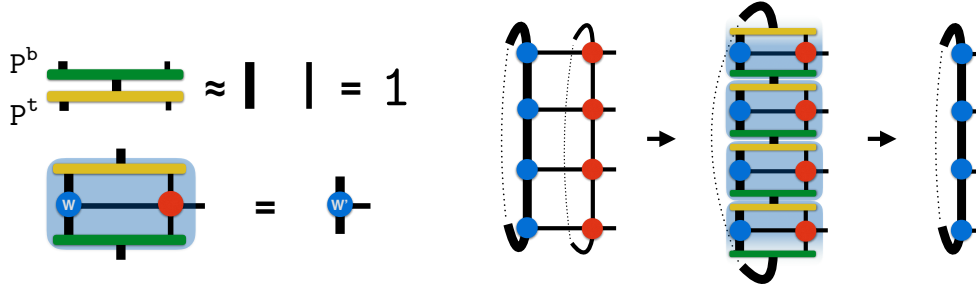


Figure 6.4: Illustration of the compression schemes employing a PBC MPS representation of the boundaries. Here one insert approximate resolutions of the identity at each bond after merging with a column of PEPS tensors.

of the advantages of preserving this symmetry at the level of the PEPS encoding. Also, since now the boundary bond dimension corresponds to the coarse graining of PEPS indices with dimension D^2 , the value of χ required to achieve convergence could be increased significantly.²

The evaluation of observables can be done by employing the same ideas presented in Sec. 4.3.4. The computational cost in this setting becomes $\mathcal{O}(\chi^3 D^6 + \chi^2 D^9 d)$ provided we employ the single-site optimization explained in the previous chapter and we avoid the direct computation of the full cost function in Eq. 4.15.³

6.2.3 Local PBC-MPS schemes

In these schemes we employ a PBC MPS representation for the boundary, see Fig. 6.3, and compress the enlarged boundary tensors upon absorption of a column of bulk double PEPS tensors by introducing approximate resolutions of the identity on each bond, as in Fig. 6.4, allowing us to preserve any translation symmetry present in the PEPS representation.

In order to obtain the (approximate) resolutions of the identity required we have employed two approaches. The first one relies on employing the idea of projective truncations, successfully used in the context of TNR, see Sec. 3.3.3, where they are given in terms of isometric matrices. We show the cost function employed in Fig. 6.5. We shall refer to this approach as the *projective truncation* PBC (PT PBC) approach. This approach can be implemented with a leading computational

²As a rule of thumb the values of χ for which convergence is typically achieved scale as $\chi \sim \mathcal{O}(D^2)$, whenever performing simulations using OBC. When using PBC, and then folding these additional indices through the bulk, we effectively square the PEPS bond dimensions being compressed and thus naively expect a scaling of the form $\chi \sim \mathcal{O}(D^4)$.

³Employing the so-called double-site MPS optimization would entail a growth of the computational cost to $\mathcal{O}(\chi^3 D^8 + \chi^2 D^{11} d)$ and so we avoid its use here.

complexity scaling as $\mathcal{O}(\chi^3 D^6)$. The second approach employs a modification of the CTM procedure employed on the infinite plane [107], where the resolutions of the identity are now given in terms of generic projectors. We shall refer to this approach as the iCTM PBC approach and show the steps involved in Appendix A. It can be implemented with a leading computational complexity of $\mathcal{O}(\chi^3 D^6)$

Since in computing the resolutions of the identity above we do not employ the full wave function, we refer to these schemes as *local* schemes.

These schemes have the advantage that, by preserving any translation symmetry present in the PEPS unit cell, they allow for a convenient preconditioning of the boundary tensors since one may simply recycle boundaries obtained on an infinite plane. Here, to maximize efficiency, we shall recycle these boundaries directly and employ the resolutions of the identity to obtain the tensor networks required for measurements.

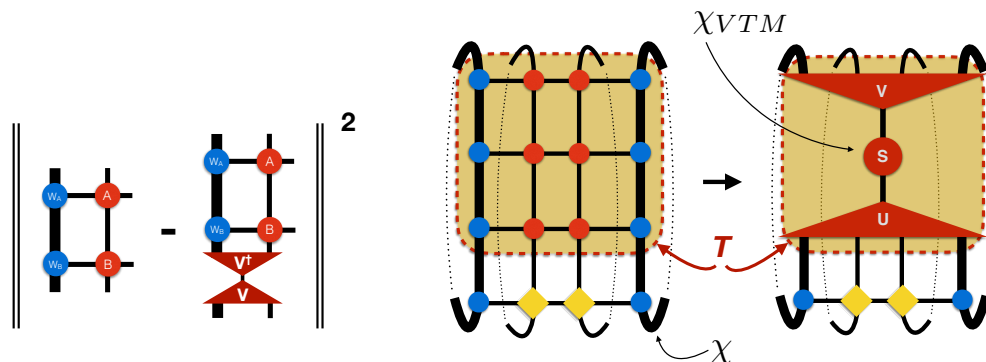


Figure 6.5: Left: illustration of the cost function employed in the PT PBC scheme to obtain resolutions of the identity in terms of isometries. Right: illustration of a procedure employed to compress the cylindrical transfer matrix T (brown box) representing the environment of a set of measurement tensors (yellow diamonds). By performing an SVD of this environment one may improve the efficiency of the computations in a controlled way.

When employing these schemes one may perform additional controlled approximations to improve the efficiency in calculating local observables. To do this we employ a truncated SVD of the cylindrical transfer matrix T representing the environment around a set of measurement tensors, see Fig. 6.5, in which we keep χVTM states after truncation. Such an approximation pays off particularly well in situations where the width of the unit cell is significantly smaller than that of the cylinder. The reason is that in such a case the spectrum of T thins down exponentially fast with the ratio between widths.

6.2.4 Global PBC-MPS scheme

This scheme represents a variant of the schemes above in which the full wave function is employed in computing the resolutions of the identity at each bond. We refer to this scheme as the *full wave function* iCTM PBC scheme and illustrate in App. A a possible way of proceeding. However, we shall not be presenting data obtained using this approach here.

6.3 Benchmarks

Since in PEPS simulations there is a number of different sources of error, we shall simplify the following discussion by exploiting a very convenient property of PEPS wave functions, namely, their modularity. This modularity originates in the fact that, once a particular unit cell structure has been chosen and PEPS tensors representing states of interest have been obtained, *e.g.*, by numerical optimization or direct construction, they may be embedded in any lattice admitting a complete covering based on the chosen PEPS unit cell.⁴ Thus providing *Ansatz* states for a range of lattice sizes directly from a single simulation. In our case this will allow us to focus on the computation of boundary fixed points without dealing with the additional complexity of optimizing the PEPS tensors. A task which we postpone to future work.

In order to evaluate the different schemes we shall rely on three criteria: convergence, time-to-solution and accuracy, which we will evaluate by performing simulations of the transverse field Ising model for a number of transverse field values at various cylinder widths W .

6.3.1 Transverse field Ising model

The transverse field Ising model (TFIM) is defined as

$$H = - \sum_{\langle i,j \rangle} \sigma_i^z \sigma_j^z - h \sum_i \sigma_i^x,$$

with $\langle i, j \rangle$ and i , here and below, running over all bonds and all sites on the lattice, respectively, and σ^α representing a Pauli matrix. As is well known, and depending on the value of the magnetic field h , this model exhibits two different phases, *i.e.*, a ferromagnetic and a paramagnetic phase, which are separated by a critical point at $h_c \approx 3.04$ [54, 197–201]. In the region $h < h_c$ the ground-state

⁴This feature has already been successfully exploited in previous PEPS studies. See, *e.g.*, Refs. [128, 193–196].

manifold is doubly degenerate with the ground states being characterized by a finite magnetization along the z axis M_z . On the other hand the region $h > h_c$ has a nondegenerate ground-state manifold with a vanishing M_z magnetization and a finite magnetization M_x parallel to the field applied. In both cases the system exhibits a finite energy gap away from h_c , regardless of the width of the cylinder. The value h_c , however, corresponds to a critical point at which a second order phase transition is found, leading to the closing of the energy gap.

The presence of the critical point will allow us to probe the accuracy of the various contraction schemes by tuning the magnetic field from a mildly correlated regime with $h = 1$ to a strongly-correlated regime at $h = 3$ and a number of values in between.

Convergence

We begin by examining the rate at which each scheme approaches a given value of the energy per site, *i.e.*, we compare the value of the energy for a given value of χ to that achieved for the largest χ considered.

We show some sample convergence curves as a function of the boundary bond dimension χ in Fig. 6.6 for fields $h = [1.0, 2.75, 2.9]$ using the FU. There it can be seen how for small values of the magnetic field, *i.e.*, $h = 1$, all of the schemes achieve excellent convergence at reduced values of χ , reflecting the short correlation length of the states. Moving closer to the critical point leads to an overall up-shift of the various curves for all the methods. This is expected due to the same reason above, *i.e.*, a more strongly-correlated state requires a larger bond dimension to account for the increased entanglement present in the state.

Interestingly, the relative convergence behavior exhibited between narrow and wider cylinders is reversed between the OBC scheme and the local PBC schemes, *i.e.*, the local PBC schemes converge faster for wider cylinders whereas the OBC scheme tends to converge faster for narrower cylinders. This is most likely a consequence of the interplay between the bond dimensions χ and χ_{VTM} . More precisely, to judge convergence in the local schemes we proceed by considering fixed values of χ_{VTM} and then observe convergence as a function of χ . Given that the spectrum of the tensors T , see Sec. 6.2.3, depends directly on the value of χ chosen, fixing the value of χ_{VTM} leads to a slight reduction in accuracy, *i.e.*, a somewhat slower convergence. Since the spectrum of the transfer matrix T is most dense for narrower cylinders, it is there where the effect becomes most relevant.

As Fig. 6.6 shows, even though a slow down in convergence is a generic feature of all schemes as one moves to values of h closer to h_c , both the smoothness as well as the rate with which convergence is achieved (at least in this example) by employing the OBC MPS scheme is noticeably better than that of the other two

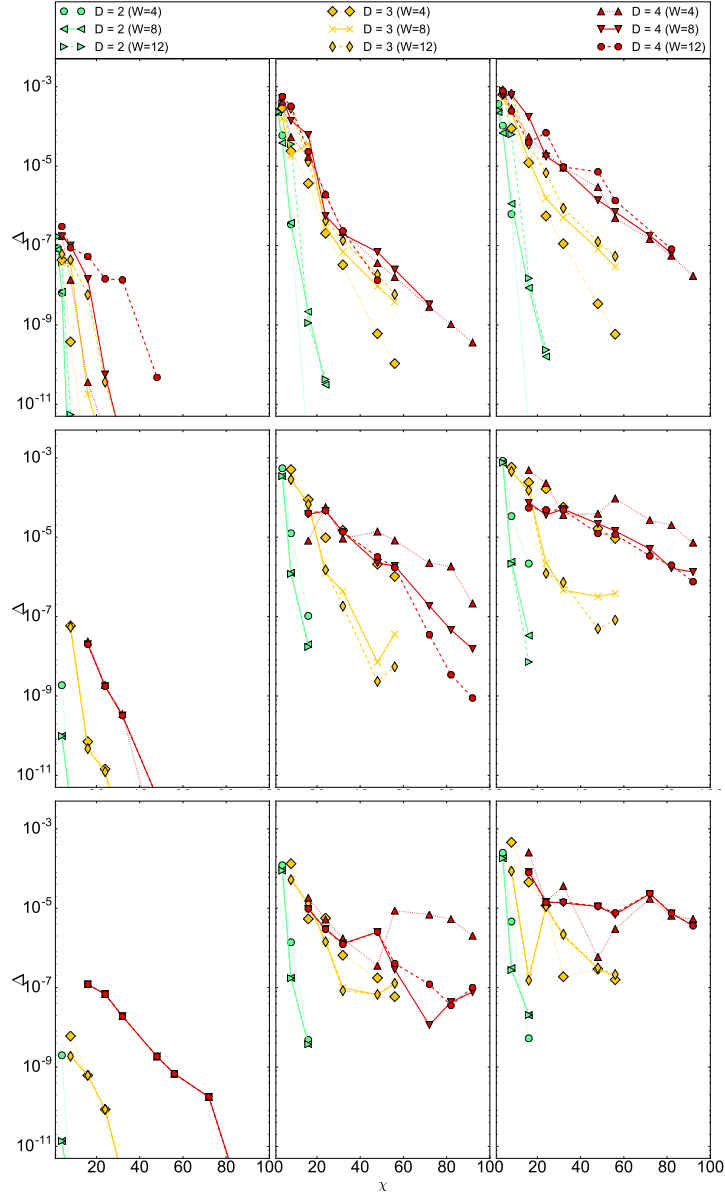


Figure 6.6: Relative convergence plots of the energy per site for the various contraction schemes. Top row: OBC, middle row: iCTM PBC and bottom row: PT PBC schemes, respectively. The left/middle/right columns corresponds to field values of $h = 1.0$, $h = 2.75$ and $h = 2.9$, respectively. All simulations were carried out using tensors optimized via the FU.

schemes. Indeed, from the plot it is apparent that the values at which a given convergence level is achieved are also systematically smaller compared to those of the local schemes. A finding which is rather at odds with our original expectations.

This is most likely a consequence of the fact that more compact representations of optimization minima can be found using the OBC MPS scheme due its global nature. It is also plausible that the possibility of breaking translation symmetry allows for more flexible search paths, although we have found no evidence of a significant artificial symmetry breaking once the boundaries have converged.⁵

Accuracy

To illustrate the accuracies achievable with our current approaches we show in Fig. 6.7 the relative error in energy per site as a function of cylinder width obtained using tensors from both the SU and the FU of various bond dimensions D . Even though we only show results for the OBC scheme directly, the supporting plots on the right column show that variations between the OBC and the iCTM PBC scheme are small enough to yield no qualitative changes to those presented in Fig. 6.7. Thus showing that results remain consistent across the approaches employed.

There it is possible to see the remarkable accuracies achievable whenever performing simulations off criticality. However, once we start approaching the critical point the accuracy of our simulations starts to drop rapidly, particularly for cylinders of narrower widths. Since the OBC scheme properly accounts for finite size effects in the construction of the boundary fixed points, we expect the primary limiting factor in this regime to be the quality of the PEPS tensors used. This is supported by the modest variations found with respect to the iCTM PBC scheme.

As expected the tensors optimized via the SU generically exhibit a lower accuracy whenever simulating states of a considerable correlation length, *i.e.*, beyond $h = 1.0$ in the plot. When employing FU-optimized tensors we find that values of very good quality, *i.e.*, at least as good as $\Delta E \sim 10^{-4}$, are achievable for all cylinder widths considered, even when restricting ourselves to simulations of modest bond dimension D and placing the system at a value of the magnetic field $h = 3.0$, *i.e.*, about a percent away from the critical point.

Time-to-solution

In Fig. 6.8 we show a comparison of the time-to-solution required for various values of the cylinder width W and bond dimension D using the author's MATLAB-based implementations of all three contraction schemes. Proper attention has been paid to employing only operations abiding to the known optimal computational

⁵The convergence behavior for tensors employing the SU is significantly improved for all schemes and thus Fig. 6.6 represents a worst-case scenario.

6.3 Benchmarks

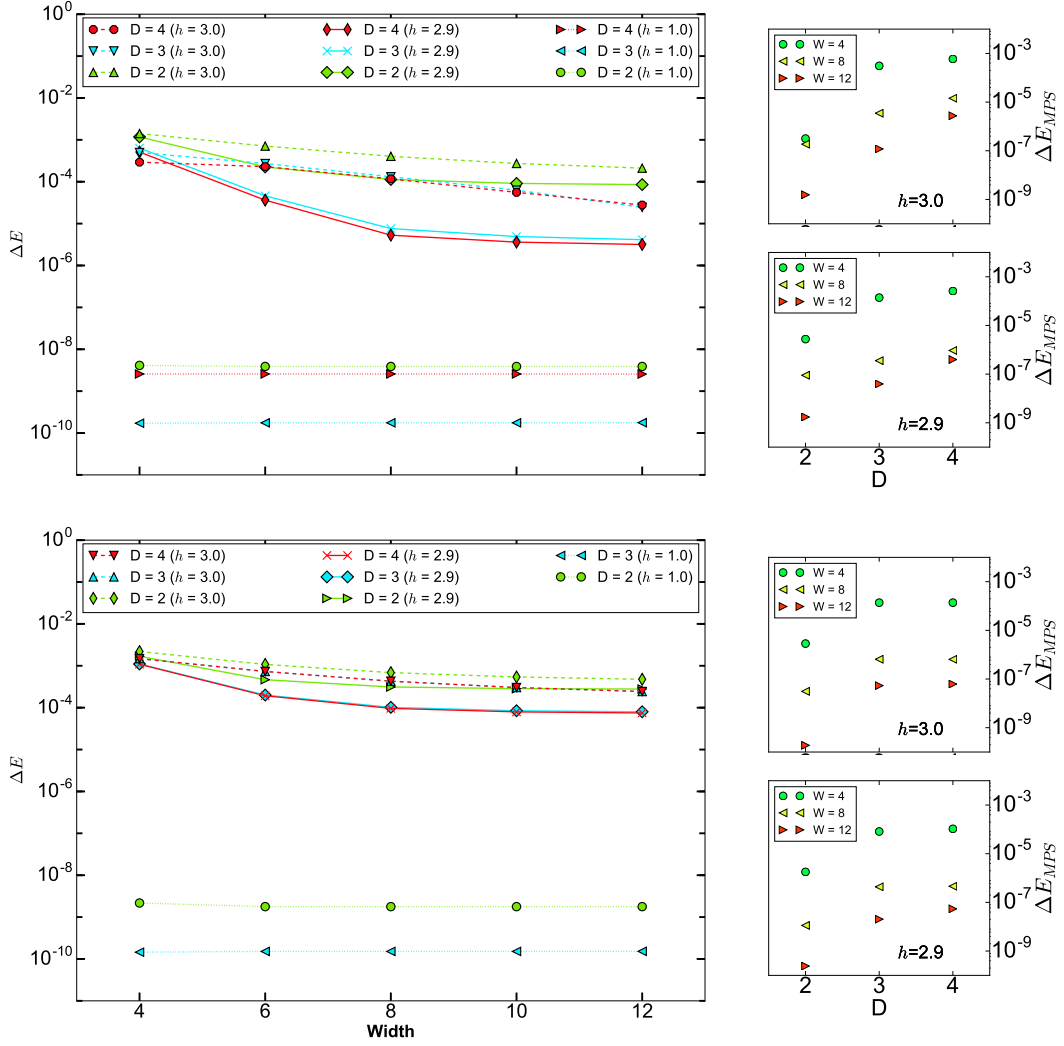


Figure 6.7: Left: relative error in the energy per site using the OBC MPS scheme employing tensors optimized via the FU (top) and SU (bottom). Reference values were obtained using results from the iDMRG algorithm extrapolated to zero truncation error. Right: relative difference between iCTM PBC and OBC schemes with the FU (top half) and the SU (bottom half). Field values are shown in the plot.

complexity, however, none of the implementations has been optimized for ultimate performance. All simulations were performed sequentially using the same type of processor.

As one may readily convince oneself, a number of caveats may arise when performing such a direct comparison. Indeed, as we explained above the way the simulations are carried out are not equivalent nor are the expected computational

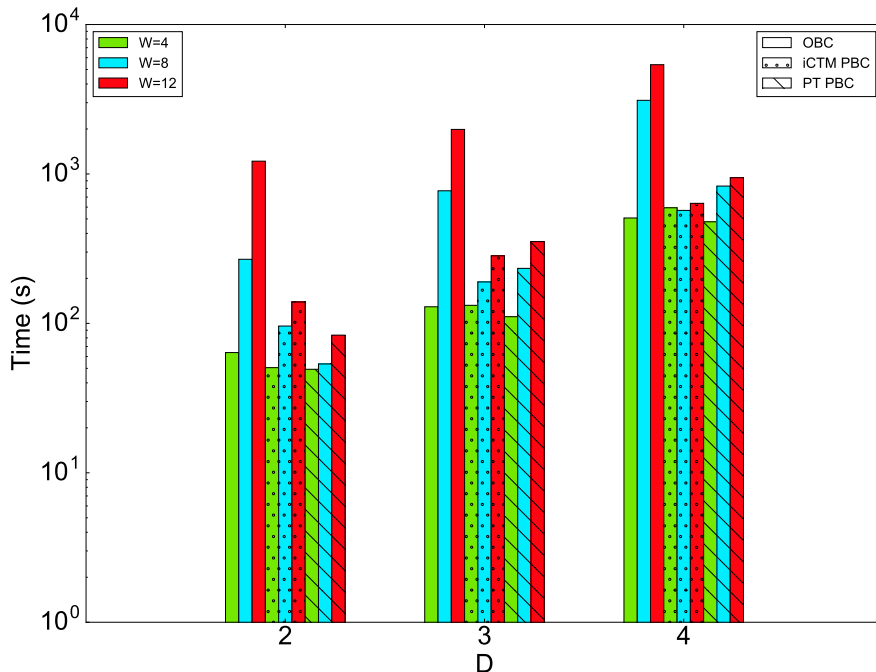


Figure 6.8: Time to solution for all three contraction schemes. Time required to complete the measurement of all observables required for the evaluation of the energy per site. The data corresponds to simulations at $h = 2.75$ employing FU tensors.

scalings. We thus show the results in Fig. 6.8 mostly to give a feeling for the relative run-time between schemes under similar conditions and not because of their being of quantitative relevance.

As Fig. 6.8 shows, a significant difference in the actual run times of the algorithms indeed arises in practice. Indeed, for the two largest cylinder widths presented, *i.e.*, $W = 8, 12$, the results show that employing one of the local schemes can result in a reduction of the overall runtimes up to a factor of ~ 10 . A qualitative difference between the OBC and the local MPS schemes is that whereas in the former the operation carrying the leading computational complexity is proportional to the cylinder width W , in the latter schemes the terms scaling linearly with W are actually subleading so that once we reach a large enough D (χ), we expect to see no system size dependence. This is an effect which appears to be visible at $D = 4$ for the iGCTM PBC scheme, although larger values of D would be required to verify that the simulations have already started to reach such regime.

All in all the results in Figs. 6.6 and 6.7 not only strengthen the idea of employing PEPS wave functions on cylinders as a viable one but also validate an approach exploiting the modularity of PEPS wave functions as well as locality in the contraction schemes as long as cylinders wide enough are considered, *i.e.*, $W \gtrsim 6$. This is

a conclusion which extends to other models like the Heisenberg model below (data not shown).

6.4 iMPS vs iPEPS comparison

As we mentioned at the beginning of the chapter, the main motivation for this work pertains the exploration of the iPEPS algorithm as a viable approach on cylindrical geometries. This is particularly important as simulations on cylinders have become the *de-facto* approach for MPS studies of 2D strongly-correlated systems, in which an understanding of the physics at the thermodynamic limit is obtained by means of simulating cylinders of increasing widths. As is well known, however, such studies can yield results which are in stark contrast to those from studies targeting the thermodynamic limit directly, *e.g.*, using iPEPS wave functions on the infinite plane. A notorious example has recently arisen in the study of the antiferromagnetic Heisenberg model on the Kagome lattice where MPS studies favored a gapped \mathbb{Z}_2 spin liquid [176, 202, 203] whereas a *projected entangled-simplex state* (PESS) *Ansatz* [204],⁶ provides evidence for a gapless spin liquid [102, 205]. Thus, studying the relative performance of iMPS and iPEPS on cylindrical geometries may help us understand the limits of MPS studies of 2D systems as well as provide an important benchmark for future developments of the iPEPS algorithm.

In what follows we shall begin to address the question: when should, if ever, iPEPS become the method of choice over iMPS, when simulating strongly-correlated systems on infinite cylindrical geometries? In order to do so we will consider two paradigmatic models: the Heisenberg and Hubbard models on the square lattice.

As we found in Sec. 6.3, it is possible to obtain good results by performing iPEPS calculations based on a recycling of the boundaries together with a iCTM PBC contraction scheme in which the approximate resolutions of the identity are obtained by means of *local* computations, see Sec. 6.2. Since this approach is very favorable in terms of computational costs, we shall employ it in our discussion below.

The results presented in this section have been published in [139] as part of a collaboration. The author would like to thank Prof. Philippe Corboz for authorizing the publication of his iPEPS data for the Hubbard model, shown in Fig. 6.12, as part of this work. The PEPS tensors optimized using the variational update for the Heisenberg model were also provided by him.

⁶A PESS can be regarded as a variant of PEPS in that they are constructed by projecting more complex simplices at the virtual level, compared to the single sites employed in PEPS [204].

6.4.1 Heisenberg model

We begin by considering the Heisenberg model

$$H = \sum_{\langle i,j \rangle} \hat{S}_i \cdot \hat{S}_j,$$

with \hat{S} defining spin-1/2 operators. For $W = 2$ cylinders the system becomes strongly dimerized, with a finite spin gap separating the ground state from a band of propagating spin triplets. Even though this picture remains valid for any finite even width, increasing the system width has the effect of reducing the energy gap. In the limit $W \rightarrow \infty$ the energy gap closes, giving way to a critical state with an algebraic decay of correlations and a finite sublattice magnetization. The most accurate results to date, using stochastic series expansions (SSE), give an energy per site $E_0 = -0.6694421(4)$ in the thermodynamic limit [206].

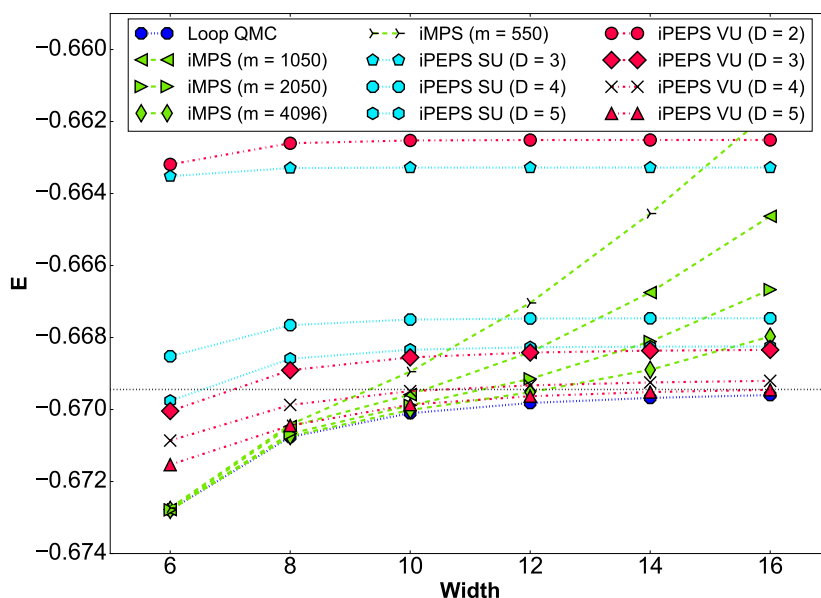


Figure 6.9: Variational energies for the Heisenberg model using iMPS (dashed lines/green symbols), iPEPS SU (dotted lines/cyan symbols), iPEPS VU (dot-dashed lines/red symbols) and loop QMC (dotted line/blue circles) methods. Loop QMC error bars are smaller than the symbol size. The black horizontal dotted line represents the SSE thermodynamic limit estimate, $E_0 = -0.6694421(4)$, from Ref. [206]. For the largest bond dimensions considered, *i.e.*, $m = 4096$ and $D = 5$, a crossover between iMPS and iPEPS is visible around $W \sim 11$.

Our main results for the Heisenberg model are shown in Fig. 6.9. As initially expected, various crossings of the energy curves appear depending on the precise

values of the bond dimension as well as optimization scheme used. For the largest bond dimensions considered, *i.e.*, $m = 4096$ and $D = 5$, the crossover where iPEPS outperform iMPS happens at a width $W \sim 11$, although a very close competition is clearly visible in the range $W \in [8, 12]$.

For the iPEPS simulations we find that, up to the largest bond dimension considered ($D = 5$), most curves corresponding to the SU remain remarkably flat across the full set of widths simulated. Given that the SU is based on an approximation incorporating only subparts of the wave function, renormalization effects arising due to longer-ranged entanglement are almost completely absent and, in this case, it simply produces states for which the correlation length does not appear to become large enough to notice the finite width of most cylinders considered. Indeed, the values of the energy obtained contain only minor corrections to the value obtained for the 2D system.

On the other hand simulations with tensors using the variational update (VU) improve significantly on the energies of the SU and a bending of the energy curves is clearly visible as one moves to narrower cylinders, although not enough to completely match the accuracy of the iMPS simulations for the narrowest cylinders shown ($W = 6$). The overall improvement of the VU compared to the SU can be understood as a consequence of the tensors providing more accurate approximations to the physics of the infinite size system. Still, given that we are ultimately not properly accounting for finite size effects, as one moves to narrower cylinders the relative accuracy drops considerably below $W \sim 8$.

We find that iMPS simulations manage to reproduce the reference energy values to high accuracy for cylinder widths up to $W \sim 10$ where, for a given bond dimension m , a clear up-bend in the curves starts to take place resulting in a significant loss in accuracy. This is a clear reflection of the fact that the bond dimensions considered are not enough to compensate for the higher entropic demands of simulations on wider cylinders.

To get an overall idea of how efficient the encoding of the wave functions is, in Fig. 6.10 we show a comparison of the relative errors for both iMPS and iPEPS as a function of inverse number of variational parameters. There it is again possible to see how, for a fixed number of variational parameters, the VU provides a significantly more accurate estimate than that of the SU. More importantly, it is also possible to see how the VU curves systematically decay faster than the SU curves as one increases the number of variational parameters. The improved efficiency of the PEPS encoding is clearly visible in that all PEPS curves are located to the right of all MPS curves. It is remarkable that, starting with cylinders of width $W \sim 8$, the rate of decrease in relative error for iPEPS wave functions as a function of inverse number of variational parameters essentially matches that of iMPS on the narrowest cylinders considered ($W = 4$). This observation becomes all the more relevant once we recall that these tensors have not been optimized for

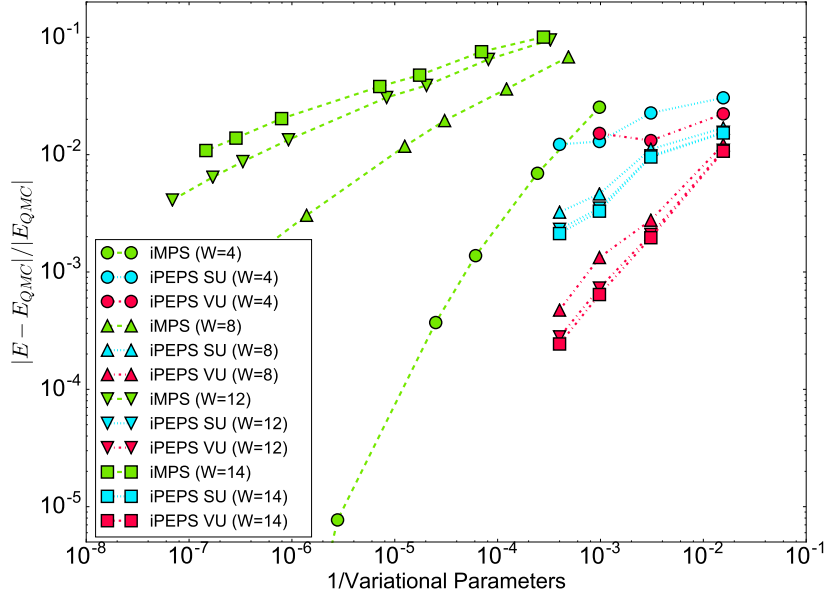


Figure 6.10: Relative error of the different *Ansatz* wave functions for the square lattice Heisenberg model as a function of inverse variational parameters. The higher efficiency of the iPEPS *Ansatz* (SU – dotted lines/cyan symbols, VU – dot-dashed lines/red symbols) is reflected on the fact that all iPEPS curves are located to the right of all iMPS curves (dashed lines/green symbols). We employ non-symmetric tensors to simplify the counting of variational parameters.

each of the cylinder widths.

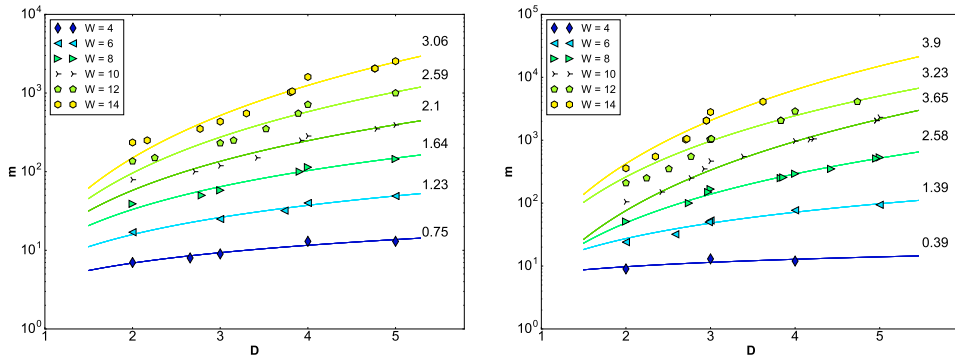


Figure 6.11: Energy based correspondence between iMPS and iPEPS bond dimensions m and D for simulations of the Heisenberg model using the SU (left) and VU (right). Estimated values for \tilde{W} in Eq. (6.2) are shown next to the curves.

Finally we may turn to the correspondence between values of the bond dimensions

m and D as a function of the cylinder widths. To obtain an m -to- D mapping we match their energy as a function of their bond dimensions, *i.e.*, for each *Ansatz* we perform linear interpolations of the energy curves at a fixed width and then for each value of m (D) we find the expected accuracy and the value of D (m) matching that value. We show the correspondences obtained using the SU and FU in Fig. 6.11, where it is possible to see that indeed, at least for cylinders of moderate width, a relation of the form

$$m \sim D^{\tilde{W}}, \quad (6.2)$$

analogous to that in Eq. (6.1), does appear to hold albeit with values \tilde{W} differing from the actual width W of the cylinder. In fact, considering the case $W = 10$, as in our example at the beginning of the chapter, instead of $\tilde{W} \approx W$ we find values of $\tilde{W} \approx 2.1$ and $\tilde{W} \approx 3.6$ when matching accuracies between states using the SU and VU, respectively. This in turn yields a pair of bond dimensions $D = 4$, $m \sim 1000$ offering comparable accuracies. In other words, our initial estimate resulted in a gross overestimation of the value of m required to match a PEPS state with a given D .

6.4.2 Hubbard model

We now consider the Hubbard model

$$\mathcal{H} = -t \sum_{\langle i,j \rangle, \sigma} \left(\hat{c}_{i\sigma}^\dagger \hat{c}_{j\sigma} + h.c. \right) + U \sum_i \hat{n}_{i\uparrow} \hat{n}_{i\downarrow},$$

where $\hat{c}_{i\sigma}^\dagger$ ($\hat{c}_{i\sigma}$) creates (annihilates) an electron with spin σ on site i and $\hat{n}_{i\sigma} := \hat{c}_{i\sigma}^\dagger \hat{c}_{i\sigma}$ represents the number operator. This model has been studied extensively using a large variety of numerical methods given its close connection to the physics of the cuprate high-temperature superconductors, see Refs. [22, 207–212] and references therein. In the half-filled case, *i.e.*, $n := \frac{1}{N} \sum_i \langle n_i \rangle = 1$ and N the number of sites, it is widely accepted that the system finds itself in a Mott-insulating regime for arbitrarily small values of the on-site repulsion U . Since we wish to avoid difficulties arising due to a large number of competing states, a problem largely present at weak doping, we shall constrain our simulations to the half-filled regime at a strong repulsion of $U/t = 8$. Using this set of parameters the ground-state energy per site has been estimated using auxiliary field QMC (AFQMC) to be $E_0 = -0.5247(2)$ in the thermodynamic limit [22].

The ground-state energy per site on an infinite cylinder of width 6 has been estimated using state-of-the-art finite DMRG simulations, employing elaborate finite-size-effect cancellation and extrapolation techniques, to be at $E_0^{(6)} = -0.52528(1)$ [22].

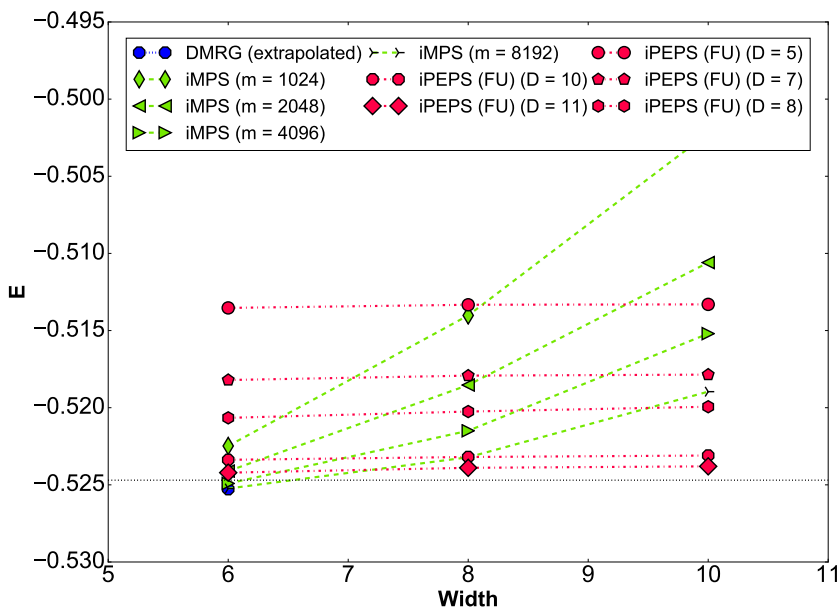


Figure 6.12: Variational energies for the half-filled Hubbard model at $U/t = 8$, using iMPS (dashed lines/green symbols), iPEPS (dot-dashed lines/red symbols) and (extrapolated) DMRG (blue circle) methods. The DMRG result was obtained from Ref. [22]. The horizontal dotted line represents the AFQMC thermodynamic limit estimate, $E_0 = -0.5247(2)$, from Ref. [22]. For the largest bond dimensions considered, *i.e.*, $m = 8192$ and $D = 11$, a crossover between iMPS and iPEPS is visible around $W \sim 7$.

Our main results for the half-filled Hubbard model are summarized in Fig. 6.12. In general we find a situation qualitatively similar to that in Fig. 6.9 for the Heisenberg model, in that various energy crossings are visible depending on the different values of the bond dimensions m and D . In this example we find that for the largest bond dimensions considered, *i.e.*, $D = 11$ and $m = 8192$, the crossover where iPEPS provides an improvement over iMPS happens at a width of $W \sim 7$.

For our iMPS simulations we find good convergence at $W = 6$, where we may directly compare to Ref. [22], after which a strong increase in energy is noticeable for all bond dimensions considered. This more rapid increase in iMPS energies, compared to the one found above for the Heisenberg model, can be understood as a consequence of the increased local Hilbert space dimension, *i.e.*, 4 compared to 2 of the Heisenberg model, thus allowing for a more rapid build-up of entanglement between different parts of the system as the cylinder widths increase. Even though the largest value of m we consider here, *i.e.*, $m = 8192$, still does not quite manage to reproduce the (extrapolated) reference energy quoted above, it is nevertheless reassuring to see that the difference found is quite small, with a relative difference

$\Delta E^{(6)} \approx 0.01\%$. It is also interesting to see that, without any additional extrapolation, the variational energies of the largest bond dimension iPEPS simulations already come very close to the thermodynamic limit estimate, with a relative error of $\Delta E = 0.17\%$.

As in the case of the Heisenberg model we find that the energy-based m -to- D correspondence for the Hubbard model, shown in Fig. 6.13, also exhibits the proposed functional form in Eq. (6.2). Here the functional form is rather visible up to values of the bond dimensions lying on the lower end of the curves, reflecting the fact that the smaller (for a given width) values might have still not been large enough to approximate the ground state properly.

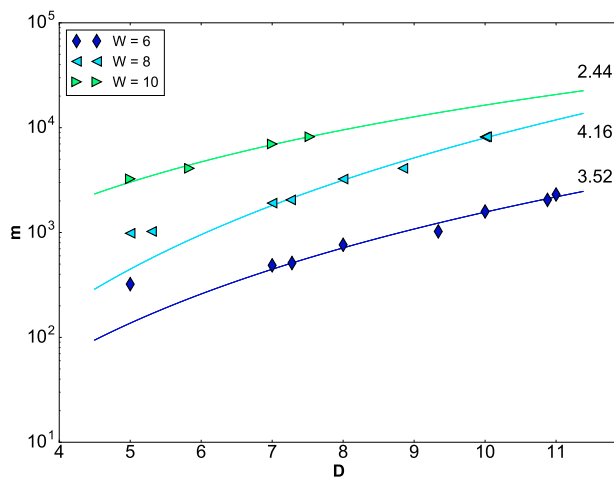


Figure 6.13: Energy based correspondence between iMPS and iPEPS bond dimensions m and D , respectively, for simulations of the Hubbard model using the FU. Estimated values for \tilde{W} in Eq. (6.2) are shown next to the curves.

Before closing this section we emphasize that the discussion on the m -to- D mapping is based entirely on matching the *energy* of the various *Ansatz* states and it is thus not obvious that such a procedure should give results analogous to those obtained from the matching of *entanglement entropies*, as discussed in the beginning of the chapter. We believe that the exponential behavior found for m as a function of D in Figs. 6.11 and 6.13 can nevertheless be understood as a reflection of the latter.

For this we begin by noting that the presence of a finite energy gap guarantees that a lower variational energy is indeed a good indicator of the proximity to the ground state. Thus, once one has reached bond dimensions large enough to properly encode the physics of the ground state one effectively obtains representations of the same state, and thus the same entanglement entropy, up to spurious contributions from higher excited states. Noting that the energy gaps start to close as the

cylinder widths start getting larger, the fact that the exponential behavior begins to disappear once the cylinder widths reach a certain threshold, *i.e.*, $W \sim 10 - 12$ in this case, appears to support this argument. In other words, the closing of the energy gaps allows for a mixing of more and different types of states thus breaking the correspondence.

6.5 Discussion

We started off this chapter with a very basic discussion based on entropic arguments in which we motivated the exploration of the iPEPS algorithm on infinite cylindrical geometries. One of the goals of this exercise was to evaluate the feasibility of such an approach when compared to the more widely spread use of (i)MPS simulations on the same type of geometry.

Since the use of the iPEPS algorithm on infinite cylindrical geometries had been, until now, largely unexplored territory, in the first half of the chapter we focused on various possible formulations and found that the combination with OBC MPS techniques is possible, yielding very satisfactory results even without the explicit tuning of the PEPS tensors for each individual cylinder. In addition, we explored alternative contraction schemes with the aim of preserving any translation symmetry present in the original PEPS *Ansatz* while remaining computationally cheap. There we proposed two *local* variants which exhibited a performance largely dependent on how correlated the underlying state was, and generally requiring larger values of the boundary bond dimension χ for convergence. These local schemes could nevertheless be employed to give adequate results at a reduced runtime compared to the *global* OBC MPS scheme. We also proposed a global contraction scheme with the ability to preserve translation invariance and expect this to be the most adequate variant when going further into the tuning of the tensors for each individual cylinder. The exploration of the latter, however, remains as future work.

In the second half of the chapter we have focused on a direct comparison to the iMPS approach and have managed to show how, as expected from our original entropic argument, various crossovers in the relative accuracy of the iMPS and iPEPS *Ansätze* occur as the width of the cylinders and the bond dimensions m and D are increased. For the largest bond dimensions considered, a modest width of $W \sim 7$ was already enough to obtain an improvement over iMPS energies by using iPEPS wave functions when simulating the half-filled Hubbard model at $U/t = 8$. It seems reasonable to expect an additional improvement of iPEPS over iMPS energies as the value of U is reduced. On the other hand we found that when simulating the Heisenberg model this crossover took place at a considerably larger width of $W \sim 11$, albeit with a strong competition over the range $W \in [8, 12]$.

It is perhaps worth emphasizing that it is not the *precise* widths at which the

energy crossings take place that are of particular importance but, instead, it is the overall energy landscape which provides important insights. After all it is clear that modifications in either bond dimension will necessarily lead to a shift of the crossover value (not to mention improvements in the algorithms). The energy landscape, however, gives us a qualitative understanding of their relative accuracies and an m -to- D mapping under different settings which, together with knowledge of the actual computational effort for each simulation, can be used as a guiding principle for when to choose one method over the other.

We have found evidence for the possibility of finding m -to- D mappings via a matching of the energy accuracy and that, to an extent discussed above, their behavior matches the one expected based on an *entropic* matching of bond dimensions. All in all we have found that the initial entropic argument grossly overestimated the value of m required to match the quality of a given D PEPS wave function. This is something which we interpret as a strong sign for how much improvement should still be achievable by refining the PEPS formulation employed here.

Given that we have found good overlap between the regions in which each method exhibits proper accuracy, we believe that these results provide a good example of how MPS and PEPS algorithms may be employed in the future in a complementary way to obtain accurate results over a wide range of cylinder widths, *i.e.*, one may exploit the remarkable accuracy of MPS at reduced cylinder widths while making full use of the entropic advantage provided by PEPS at increased widths, with the intermediate region serving as a direct cross-check scenario.

Chapter 7

Conclusions & Outlook

In this thesis we have applied tensor network algorithms to study the physics of strongly-correlated two-dimensional systems. In order to make it a relatively self-contained work we have not only presented the applications and new results obtained by the author and collaborators but have also spent some time developing the basic notions required to understand the machinery involved in such computations.

Before we conclude this work we would like to digress somewhat on a number of promising avenues connected to the work presented here and which we believe constitute lines of study which might prove interesting in the future.

The idea of employing quantum-inspired contraction schemes for the renormalization of partition functions is one with plenty of room for exciting applications. Indeed, having strengthened the interpretability of *tensor network renormalization* (TNR) as a framework of proper *renormalization group* transformations in Ch. 3, the possibility of performing RG-based characterizations of both 2D classical and 1+1D quantum systems from a controlled *nonperturbative* perspective opens up, *i.e.*, by following a procedure similar to that presented in Ch. 3, one may study RG flows generated by the *complete* Hamiltonian in a controlled way without the introduction of, *e.g.*, ϵ -expansions about a given dimension of space [4]. Given the excellent characterization of the Blume-Capel model we have managed to obtain, it appears very tempting to explore, in even more detail, various interesting properties like, *e.g.*, the emergence of *supersymmetry* at its tricritical point [6] or the explicit construction of lattice analogues of scaling operators [174]. This would be of interest not only to better understand their real-space structure but could also be used, among other things, to study the transition between different universality classes.

Along these lines a significantly more challenging endeavor would correspond to the efficient formulation and implementation of a 3D TNR algorithm capable of

encoding multiplicative logarithmic corrections to the area law expected for $D \geq 2$ Fermi liquids or spin-Bose metals [213, 214]. One of the key issues to be addressed in such a project, at least naively, would be to understand how to formulate this generalization to produce a *branching* MERA structure [215], as opposed of the MERA obtained from 2D TNR [61]. The reason for this more stringent requirement is that in 3D the regular MERA does *not* allow to encode logarithmic corrections to the area law and, thus, a much more complex structure is required.

In the area of frustrated spin models the reduced number of reliable methods available make the application of iPEPS a very interesting endeavor. Even though in Ch. 5 we have constrained ourselves to the exploration of one of the earliest variants of the Kitaev-Heisenberg model, proposed to describe the physics of the layered Iridates $A_2\text{IrO}_3$ ($A = \text{Na}, \text{Li}$), the overall quality of the results we have managed to find give confidence in moving towards more complex generalizations containing off-diagonal Kitaev terms or longer-ranged interactions [216, 217]. These generalizations are introduced in order to go beyond the original family of Iridates considered here to include other interesting candidates for Kitaev physics like, *e.g.*, $\alpha\text{-RuCl}_3$ [218, 219]. For these applications it would also be very interesting to explore recent developments for finite temperature calculations [104, 105, 138], which should in principle allow to draw direct connections to current experimental efforts and fill a rather notorious gap between these and numerical simulations.

Finally, the exploration of PEPS methods on cylinders represents an area with plenty of room for improvement and applications. In Ch. 6 we have shown that PEPS indeed constitute a viable alternative for the simulation of cylindrical geometries and have suggested the exploration of complementary MPS-PEPS approaches. However, to fully exploit the potential of PEPS one of the first steps to follow would be to understand how to best perform the optimization of the wave function directly on the cylinder. Even though we have provided hints for a possible route, it is very likely that additional steps need to be taken to compensate for the relatively expensive algorithms. Once such a generalization has been properly understood the world of frustrated magnetism and fermionic systems provides plenty of models which remain controversial and could use additional input in understanding the transition from quasi-1D to 2D. One relatively obvious example corresponds to the antiferromagnetic Heisenberg model on the Kagome lattice for which MPS and PESS, a variant of PEPS in which one considers entangled simplices [204], support either gapped or gapless ground states, respectively. Also, having understood how to simulate generic systems on cylinders, the study of topologically ordered phases may be done reliably using model information only and thus extending studies based on hand-crafted wave functions [128, 193, 194].

Appendix A

Supplementary material for chapter 6

A.1 Diagrams for the construction of projectors P_b and P_t

Here we present the diagrams for the computation of the projectors P_b and P_t , introduced in Sec. 6.2.3 for the iCTM PBC and the full wave function PBC schemes. We show the operations employed for the iCTM PBC scheme in Fig. A.2. For the full wave function PBC scheme we propose to replace the starting diagram in A.2(a) with the construction in A.1.

A.2 Loop Quantum Monte Carlo Simulations of the Heisenberg Model

As was mentioned in the main body of the text, we have used loop QMC simulations as reference data to judge the accuracy of iMPS and iPEPS when simulating the Heisenberg model. For these simulations we have relied on version 4.0a1 of the loop QMC code available as part of the ALPS project.[93] Since loop QMC simulations are carried out both at finite temperature as well as finite size, obtaining ground state estimates in the thermodynamic limit will in general require finite-T as well as finite-size extrapolations. In order to simplify the procedure we have performed all simulations at temperatures low enough to render the finite T variations comparable to the statistical error. We found that temperatures in

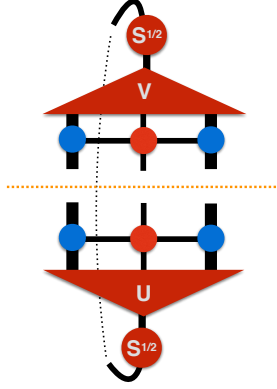


Figure A.1: Proposed construction for the full wave function computation of the projectors P_b and P_t . The upper and lower halves (separated by the orange dashed line), could be handled like the corresponding halves in Fig. A.2a). The objects U , S , V would be obtained in the same way as in the right panel of Fig. 6.5. The bond wrapping around the cylinder, of dimension χ_{VTM} , could again be used as a "perturbation" parameter with which to speed-up calculations.

Width	E_0
4	-0.683282(2)
6	-0.672788(1)
8	-0.670760(2)
10	-0.670101(2)
12	-0.669815(2)
14	-0.669677(1)
16	-0.669594(3)

Table A.1: Loop QMC estimates for the infinite-length finite-width ground state energies of the $S = 1/2$ Heisenberg model on square lattice cylinders.

the range $T \sim [0.01, 0.003]$, depending on cylinder width, were enough to obtain negligible variations.

To obtain energy estimates in the infinite-length limit, we carried out simulations on systems of various lengths $L \in [32, 1024]$. This data was then extrapolated assuming a scaling of the form $E(L) = a + b(1/L)$ which, given that the system always has a non vanishing energy gap, is a reasonable assumption. For the actual energy estimates we obtained, see Table A.1.

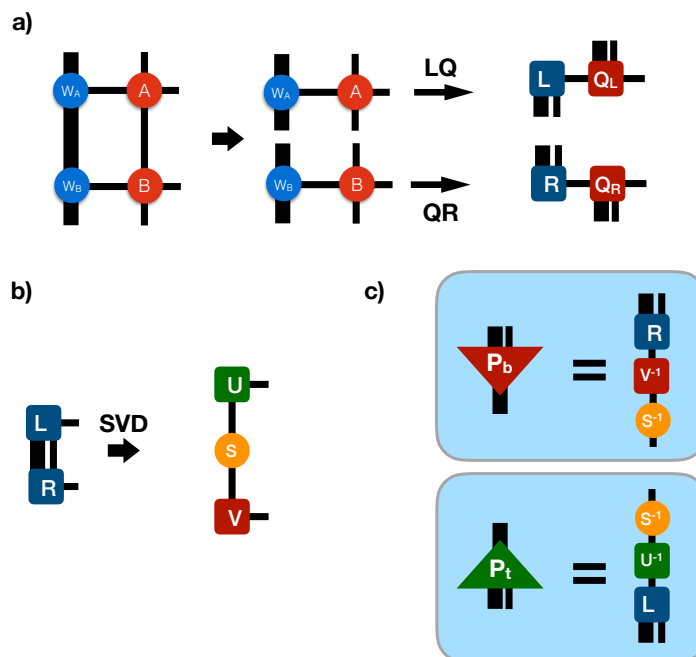


Figure A.2: Sequence of operations employed in the iCTM PBC scheme from Sec. 6.2.3. The cost of the initial QR/LQ decompositions can be reduced by employing truncated SVD decompositions.

A.3 iPEPS Simulations

As mentioned in the main text, we find that recycling the boundaries obtained from a simulation on the infinite plane provides good starting points for the boundary construction. The iCTM PBC scheme was then used to adjust the boundaries when performing measurements.

When computing the energies, a cylinder made up of the boundary tensors W and up to 2 columns of PEPS tensors must be contracted. In addition to the compression mentioned in Fig. 6.5, we also employed, for the larger values of D , an additional compression step which reduces the vertical transfer matrix inside the brown box in Fig. 6.5 from a four-column object to a two-column object. This compression happens in a manner completely analogous to the procedure illustrated in Fig. 6.4. An additional parameter χ' was introduced for this compression and its proper convergence also monitored.

Simulations for the Heisenberg model were carried out both with and without

preserving the S_z^{total} U(1) symmetry of the model, where the non-symmetric data was used to generate Fig. 6.10 in the main text. We present our energy estimates for the Heisenberg model shown in the main text using the simple and variational updates in tables A.2 and A.3, respectively. We estimate the error bars of the data based on the convergence of the energies as a function of all auxiliary bond dimensions. For the simple update we estimate error bars to be smaller than ± 0.0001 for all values of D . Error bars in the variational update are estimated to be at or below ± 0.0003 for all values of D . In Fig. A.3 we provide some sample data illustrating the convergence behavior we found as a function of the auxiliary bond dimension χ .

Simulations for the Hubbard model were carried out preserving both U(1) quantum numbers associated to S_z^{total} and charge conservation. We present our variational energy estimates for the Hubbard model shown in the main text in table A.4. We estimate error bars of this data to be smaller than ± 0.0001 for $D = 5$ and around ± 0.0003 for $D > 5$.

We have constrained our simulations to use checkerboard unit cells, *i.e.* 2×2 unit cells with only two types of tensors. All simulations were carried out using real double-precision arithmetic.

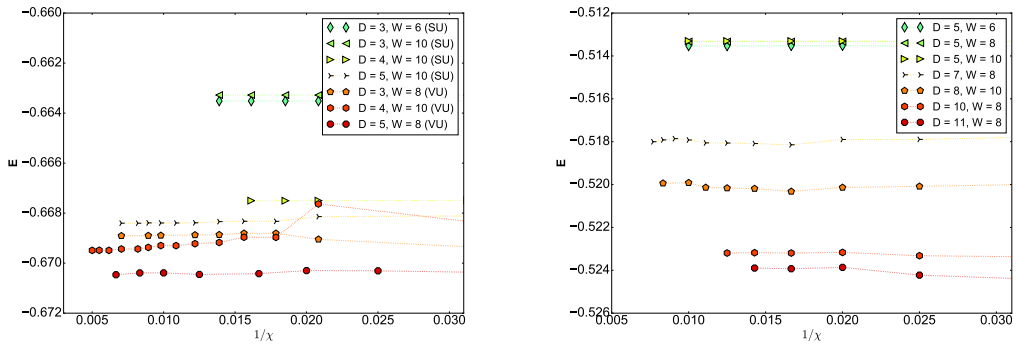


Figure A.3: Convergence of iPEPS energies as a function of the inverse boundary bond dimension χ . Top: sample convergence data for the Heisenberg model. For this data a value of χ_{VTM} large enough to exhibit negligible variations was chosen. Bottom: sample convergence data for the half-filled Hubbard model. Here an approach in which χ_{VTM} was scaled proportionally to χ^2 was used.

D \ Width	4	6	8	10	12	14	16
2	-0.6624	-0.6595	-0.6594	-0.6594	-0.6594	-0.6594	-0.6594
3	-0.6678	-0.6635	-0.6633	-0.6633	-0.6633	-0.6633	-0.6633
4	-0.6744	-0.6685	-0.6677	-0.6675	-0.6675	-0.6675	-0.6675
5	-0.6749	-0.6698	-0.6686	-0.6683	-0.6683	-0.6683	-0.6682

Table A.2: iPEPS estimates for the infinite-length finite-width ground state energies of the $S = 1/2$ Heisenberg model on square lattice cylinders using tensors optimized with the simple update. Error bars are estimated to be at or below ± 0.0001 .

D \ Width	4	6	8	10	12	14	16
2	-0.6681	-0.6632	-0.6626	-0.6625	-0.6625	-0.6625	-0.6625
3	-0.6743	-0.6700	-0.6689	-0.6686	-0.6684	-0.6684	-0.6683
4	-0.6729	-0.6709	-0.6699	-0.6695	-0.6693	-0.6692	-0.6692
5		-0.6715	-0.6704	-0.6699	-0.6696	-0.6695	-0.6695

Table A.3: iPEPS estimates for the infinite-length finite-width ground state energies of the $S = 1/2$ Heisenberg model on square lattice cylinders using tensors optimized variationally on the infinite plane. Error bars are estimated to be at or below ± 0.0003 .

A.4 iMPS Simulations

All iMPS simulations were carried out using an implementation of the iDMRG algorithm based on the ALPS libraries, which we hope to make public soon. Simulations for the Heisenberg model were carried out both with and without preserving the U(1) symmetry corresponding to the conservation of S_z^{total} present in the model. The symmetric and non-symmetric simulations were used to generate Fig. 6.9 and Fig. 6.10 in the main text, respectively. We present our U(1) symmetric variational energy estimates for the Heisenberg model shown in the main text in table A.5. Similarly, all simulations for the Hubbard model were carried out preserving both U(1) quantum numbers associated to S_z^{total} and charge conservation. We present our variational energy estimates for the Hubbard model shown in the main text in table A.6.

We have restricted the size of the optimization unit cells to be twice the width of the cylinder and used a bottom-to-top left-to-right zig-zag pattern to cover the system. All simulations were carried out using real double-precision arithmetic.

D \ Width	6	8	10
5	-0.5135	-0.5133	-0.5133
7	-0.5182	-0.5179	-0.5179
8	-0.5207	-0.5202	-0.5199
10	-0.5234	-0.5232	-0.5231
11	-0.5242	-0.5239	-0.5238

Table A.4: iPEPS estimates for the infinite-length finite-width ground state energies of the half-filled Hubbard model at $U/t = 8$ on square lattice cylinders using tensors optimized with the full update. Error bars are estimated to be smaller than ± 0.0001 for $D = 5$ and around ± 0.0003 for $D > 5$.

m \ Width	4	6	8	10	12	14	16
550	-0.68328	-0.67273	-0.67042	-0.66895	-0.66704	-0.66456	-0.66173
1050	-0.68328	-0.67278	-0.67047	-0.66959	-0.66841	-0.66675	-0.66463
2050	-0.68328	-0.67279	-0.67067	-0.66988	-0.66915	-0.66811	-0.66667
4096	-0.68328	-0.67279	-0.67074	-0.67001	-0.66952	-0.66890	-0.66797

Table A.5: iMPS estimates for the infinite-length finite-width ground state energies of the $S = 1/2$ Heisenberg model on square lattice cylinders.

m \ Width	6	8	10
1024	-0.52248	-0.51402	-0.50221
2048	-0.52411	-0.51853	-0.51059
4096	-0.52491	-0.52149	-0.51520
8192	-0.52524	-0.52321	-0.51896

Table A.6: iMPS estimates for the infinite-length finite-width ground state energies of the half-filled Hubbard model at $U/t = 8$ on square lattice cylinders.

Bibliography

- [1] Philip W Anderson et al. “More is different”. *Science* 177.4047 (1972), pp. 393–396.
- [2] John Bardeen, Leon N Cooper, and J Robert Schrieffer. “Microscopic theory of superconductivity”. *Phys. Rev.* 106.1 (1957), p. 162.
- [3] Michael Fisher. “Scaling, universality and renormalization group theory”. *Crit. Phen.* (1983), pp. 1–139.
- [4] John Cardy. *Scaling and renormalization in statistical physics*. Vol. 5. Cambridge university press, 1996.
- [5] Alexander A Belavin, Alexander M Polyakov, and Alexander B Zamolodchikov. “Infinite conformal symmetry in two-dimensional quantum field theory”. *Nuc. Phys. B* 241.2 (1984), pp. 333–380.
- [6] Malte Henkel. *Conformal invariance and critical phenomena*. Springer Science & Business Media, 2013.
- [7] Leo P Kadanoff. “Scaling laws for Ising models near T_c ”. *From Order To Chaos: Essays: Critical, Chaotic and Otherwise*. World Scientific, 1993, pp. 165–174.
- [8] Kenneth G Wilson. “The renormalization group: Critical phenomena and the Kondo problem”. *Rev. Mod. Phys.* 47.4 (1975), p. 773.
- [9] Rev Shankar. “Renormalization-group approach to interacting fermions”. *Rev. Mod. Phys.* 66.1 (1994), p. 129.
- [10] Philip W Anderson. “Resonating valence bonds: A new kind of insulator?”. *Materials Research Bulletin* 8.2 (1973), pp. 153–160.
- [11] Frédéric Mila. “Quantum spin liquids”. *European Journal of Physics* 21.6 (2000), p. 499.
- [12] Patrick A Lee. “An end to the drought of quantum spin liquids”. *Science* 321.5894 (2008), pp. 1306–1307.
- [13] Leon Balents. “Spin liquids in frustrated magnets”. *Nature* 464.7286 (2010), p. 199.

- [14] Lev Davidovich Landau. “On the theory of phase transitions. I.” *Zh. Eksp. Teor. Fiz.* 11 (1937), p. 19.
- [15] Lev Davidovich Landau and Evgenii M Lifshitz. *Statistical Physics: V. 5: Course of Theoretical Physics*. Pergamon press, 1969.
- [16] A Yu Kitaev. “Fault-tolerant quantum computation by anyons”. *Ann. Phys.* 303.1 (2003), pp. 2–30.
- [17] Michael H Freedman, Michael Larsen, and Zhenghan Wang. “A Modular Functor Which is Universal for Quantum Computation”. *Commun. Math. Phys.* 227.3 (2002), pp. 605–622.
- [18] Alexei Kitaev. “Anyons in an exactly solved model and beyond”. *Ann. Phys.* 321.1 (2006), pp. 2–111.
- [19] Patrick A. Lee, Naoto Nagaosa, and Xiao-Gang Wen. “Doping a Mott insulator: Physics of high-temperature superconductivity”. *Rev. Mod. Phys.* 78 (1 2006), pp. 17–85.
- [20] B Keimer et al. “From quantum matter to high-temperature superconductivity in copper oxides”. *Nature* 518.7538 (2015), p. 179.
- [21] John Hubbard. “Electron correlations in narrow energy bands”. *Proceedings of the royal society of london a: mathematical, physical and engineering sciences*. Vol. 276. 1365. The Royal Society. 1963, pp. 238–257.
- [22] JPF LeBlanc et al. “Solutions of the two-dimensional Hubbard model: benchmarks and results from a wide range of numerical algorithms”. *Phys. Rev. X* 5.4 (2015), p. 041041.
- [23] Bo-Xiao Zheng et al. “Stripe order in the underdoped region of the two-dimensional Hubbard model” (2016). arXiv: [1701.00054](https://arxiv.org/abs/1701.00054).
- [24] Andreas Roland Hehn. “Series expansion methods for quantum lattice models”. PhD thesis. 2016.
- [25] Kris Van Houcke et al. “Diagrammatic monte carlo”. *Physics Procedia* 6 (2010), pp. 95–105.
- [26] Evgeny Kozik et al. “Diagrammatic Monte Carlo for correlated fermions”. *EPL (Europhysics Letters)* 90.1 (2010), p. 10004.
- [27] Jan Gukelberger. “From non-unitary anyons to unconventional superfluidity”. PhD thesis. 2015.
- [28] Richard Blankenbecler, DJ Scalapino, and RL Sugar. “Monte Carlo calculations of coupled boson-fermion systems. I”. *Phys. Rev. D* 24.8 (1981), p. 2278.
- [29] Jorge E Hirsch and R Martin Fye. “Monte Carlo method for magnetic impurities in metals”. *Phys. Rev. Lett.* 56.23 (1986), p. 2521.

-
- [30] SMA Rombouts, Kristiaan Heyde, and Natalie Jachowicz. “Quantum monte carlo method for fermions, free of discretization errors”. *Phys. Rev. Lett.* 82.21 (1999), p. 4155.
- [31] Emanuel Gull et al. “Continuous-time auxiliary-field Monte Carlo for quantum impurity models”. *EPL (Europhysics Letters)* 82.5 (2008), p. 57003.
- [32] Mauro Iazzi and Matthias Troyer. “Efficient continuous-time quantum Monte Carlo algorithm for fermionic lattice models”. *Phys. Rev. B* 91.24 (2015), p. 241118.
- [33] Jakub Imriska. “Hubbard models on general lattices: a dynamical cluster approximation approach”. PhD thesis. 2016.
- [34] Matthew B. Hastings. “An area law for one-dimensional quantum systems”. *J. Stat. Mech. Theor. Exp.* 08 (2007), P08024.
- [35] Matthew B Hastings. “Solving gapped Hamiltonians locally”. *Phys. Rev. B* 73.8 (2006), p. 085115.
- [36] Michael M Wolf et al. “Area laws in quantum systems: mutual information and correlations”. *Phys. Rev. Lett.* 100.7 (2008), p. 070502.
- [37] Luigi Accardi. “Topics in quantum probability”. *Phys. Rep.* 77.3 (1981), pp. 169–192.
- [38] Mark Fannes, B Nachtergaele, and RF Werner. “Exact antiferromagnetic ground states of quantum spin chains”. *EPL (Europhysics Letters)* 10.7 (1989), p. 633.
- [39] Stellan Östlund and Stefan Rommer. “Thermodynamic limit of density matrix renormalization”. *Phys. Rev. Lett.* 75.19 (1995), p. 3537.
- [40] Steven R. White. “Density matrix formulation for quantum renormalization groups”. *Phys. Rev. Lett.* 69 (19 1992), pp. 2863–2866.
- [41] T. Nishino et al. “Two-Dimensional Tensor Product Variational Formulation”. *Prog. Theor. Phys.* 105.3 (2001), pp. 409–417.
- [42] Y. Nishio et al. “Tensor Product Variational Formulation for Quantum Systems” (2004). arXiv: [0401115 \[cond-mat\]](#).
- [43] Frank Verstraete and J. Ignacio Cirac. “Renormalization algorithms for quantum-many body systems in two and higher dimensions” (2004). arXiv: [0407066 \[cond-mat\]](#).
- [44] Frank Verstraete et al. “Criticality, the area law, and the computational power of projected entangled pair states”. *Phys. Rev. Lett.* 96.22 (2006), p. 220601.
- [45] Guifre Vidal. “Entanglement renormalization: an introduction” (2009). arXiv: [0912.1651](#).
- [46] Glen Evenbly and Guifré Vidal. “Algorithms for entanglement renormalization”. *Phys. Rev. B* 79.14 (2009), p. 144108.

- [47] Glen Evenbly and Guifre Vidal. “Entanglement renormalization in two spatial dimensions”. *Phys. Rev. Lett.* 102.18 (2009), p. 180406.
- [48] Robert NC Pfeifer, Glen Evenbly, and Guifré Vidal. “Entanglement renormalization, scale invariance, and quantum criticality”. *Phys. Rev. A* 79.4 (2009), p. 040301.
- [49] Tomotoshi Nishino and Kouichi Okunishi. “Corner transfer matrix renormalization group method”. *J. Phys. Soc. Jpn.* 65.4 (1996), pp. 891–894.
- [50] Tomotoshi Nishino and Kouichi Okunishi. “Corner transfer matrix algorithm for classical renormalization group”. *J. Phys. Soc. Jpn.* 66.10 (1997), pp. 3040–3047.
- [51] Román Orús and Guifré Vidal. “Simulation of two-dimensional quantum systems on an infinite lattice revisited: Corner transfer matrix for tensor contraction”. *Phys. Rev. B* 80.9 (2009), p. 094403.
- [52] Román Orús. “Exploring corner transfer matrices and corner tensors for the classical simulation of quantum lattice systems”. *Phys. Rev. B* 85.20 (2012), p. 205117.
- [53] Michael Levin and Cody P Nave. “Tensor renormalization group approach to two-dimensional classical lattice models”. *Phys. Rev. Lett.* 99.12 (2007), p. 120601.
- [54] ZY Xie et al. “Coarse-graining renormalization by higher-order singular value decomposition”. *Phys. Rev. B* 86.4 (2012), p. 045139.
- [55] RJ Baxter. “Dimers on a rectangular lattice”. *J. Math. Phys.* 9.4 (1968), pp. 650–654.
- [56] RJ Baxter. “Variational approximations for square lattice models in statistical mechanics”. *J. Stat. Phys.* 19.5 (1978), pp. 461–478.
- [57] Rodney J Baxter. *Exactly solved models in statistical mechanics*. Elsevier, 2016.
- [58] HH Zhao et al. “Renormalization of tensor-network states”. *Phys. Rev. B* 81.17 (2010), p. 174411.
- [59] Glen Evenbly and Guifre Vidal. “Tensor network renormalization”. *Phys. Rev. Lett.* 115.18 (2015), p. 180405.
- [60] Glen Evenbly. “Algorithms for tensor network renormalization”. *Phys. Rev. B* 95.4 (2017), p. 045117.
- [61] Glen Evenbly and Guifre Vidal. “Tensor Network Renormalization Yields the Multiscale Entanglement Renormalization Ansatz”. *Phys. Rev. Lett.* 115.20 (2015), p. 200401.
- [62] Guifre Vidal. “Entanglement renormalization”. *Phys. Rev. Lett.* 99.22 (2007), p. 220405.

-
- [63] Miguel Aguado and Guifre Vidal. “Entanglement renormalization and topological order”. *Phys. Rev. Lett.* 100.7 (2008), p. 070404.
- [64] G. Evenbly and G. Vidal. “Local Scale Transformations on the Lattice with Tensor Network Renormalization”. *Phys. Rev. Lett.* 116 (4 2016), p. 040401.
- [65] Shuo Yang, Zheng-Cheng Gu, and Xiao-Gang Wen. “Loop Optimization for Tensor Network Renormalization”. *Phys. Rev. Lett.* 118 (11 2017), p. 110504.
- [66] M. Bal et al. “Renormalization Group Flows of Hamiltonians Using Tensor Networks”. *Phys. Rev. Lett.* 118 (25 2017), p. 250602.
- [67] JC Xavier et al. “Critical behavior of the spin-3 2 Blume-Capel model in two dimensions”. *Phys. Rev. B* 57.18 (1998), p. 11575.
- [68] Paul D. Beale. “Finite-size scaling study of the two-dimensional Blume-Capel model”. *Phys. Rev. B* 33 (3 1986), pp. 1717–1720.
- [69] CJ Silva, AA Caparica, and JA Plascak. “Wang-Landau Monte Carlo simulation of the blume-capel model”. *Phys. Rev. E* 73.3 (2006), p. 036702.
- [70] Wooseop Kwak et al. “First-order phase transition and tricritical scaling behavior of the Blume-Capel model: A Wang-Landau sampling approach”. *Phys. Rev. E* 92 (2 2015), p. 022134.
- [71] PA Belov, AA Nazarov, and AO Sorokin. “Determination of CFT central charge by the Wang-Landau algorithm” (2016). arXiv: [1612.06374](https://arxiv.org/abs/1612.06374).
- [72] Philippe Francesco, Pierre Mathieu, and David Sénéchal. *Conformal field theory*. Springer Science & Business Media, 2012.
- [73] Markus Hauru et al. “Topological conformal defects with tensor networks”. *Phys. Rev. B* 94.11 (2016), p. 115125.
- [74] Davide Gaiotto. “Domain walls for two-dimensional renormalization group flows”. *J. High Energy Phys.* 103 (2012).
- [75] Mark Srednicki. “Entropy and area”. *Phys. Rev. Lett.* 71.5 (1993), p. 666.
- [76] Guifre Vidal et al. “Entanglement in quantum critical phenomena”. *Phys. Rev. Lett.* 90.22 (2003), p. 227902.
- [77] Pasquale Calabrese and John Cardy. “Entanglement entropy and quantum field theory”. *J. Stat. Mech. Theor. Exp.* 2004.06 (2004), P06002.
- [78] Marcus Cramer et al. “Entanglement-area law for general bosonic harmonic lattice systems”. *Phys. Rev. A* 73.1 (2006), p. 012309.
- [79] Michael M Wolf. “Violation of the entropic area law for fermions”. *Phys. Rev. Lett.* 96.1 (2006), p. 010404.
- [80] Yimin Ge and Jens Eisert. “Area laws and efficient descriptions of quantum many-body states”. *New J. Phys.* 18.8 (2016), p. 083026.
- [81] Norbert Schuch, Ignacio Cirac, and David Pérez-García. “PEPS as ground states: Degeneracy and topology”. *Ann. Phys.* 325.10 (2010), pp. 2153–2192.

- [82] Germán Sierra and Tomotoshi Nishino. “The density matrix renormalization group method applied to interaction round a face Hamiltonians”. *Nuc. Phys. B* 495.3 (1997), pp. 505–532.
- [83] Ian P McCulloch and Miklós Gulácsi. “The non-Abelian density matrix renormalization group algorithm”. *EPL (Europhysics Letters)* 57.6 (2002), p. 852.
- [84] IP McCulloch et al. “Phase diagram of the 1D Kondo lattice model”. *Low Temp. Phys.* 117.3-4 (1999), pp. 323–328.
- [85] Örs Legeza and Jenő Sólyom. “Stability of the Haldane phase in anisotropic magnetic ladders”. *Phys. Rev. B* 56.22 (1997), p. 14449.
- [86] Ö Legeza and J Sólyom. “Optimizing the density-matrix renormalization group method using quantum information entropy”. *Phys. Rev. B* 68.19 (2003), p. 195116.
- [87] Tetsuya Mutou, Naokazu Shibata, and Kazuo Ueda. “Temperature-Induced Gap Formation in Dynamic Correlation Functions of the One-Dimensional Kondo Insulator: Finite-Temperature Density-Matrix Renormalization-Group Study”. *Phys. Rev. Lett.* 81.22 (1998), p. 4939.
- [88] Ulrich Schollwöck. “The density-matrix renormalization group in the age of matrix product states”. *Ann. Phys.* 326.1 (2011), pp. 96–192.
- [89] Michael A Nielsen and Isaac Chuang. *Quantum computation and quantum information*. 2002.
- [90] Bogdan Pirvu et al. “Matrix product operator representations”. *New J. Phys.* 12.2 (2010), p. 025012.
- [91] Gregory M Crosswhite and Dave Bacon. “Finite automata for caching in matrix product algorithms”. *Phys. Rev. A* 78.1 (2008), p. 012356.
- [92] Gregory M Crosswhite, Andrew C Doherty, and Guifré Vidal. “Applying matrix product operators to model systems with long-range interactions”. *Phys. Rev. B* 78.3 (2008), p. 035116.
- [93] B Bauer et al. “The ALPS project release 2.0: open source software for strongly correlated systems”. *J. Stat. Mech. Theor. Exp.* 2011.05 (2011), P05001.
- [94] Michele Dolfi et al. “Matrix product state applications for the ALPS project”. *Comput. Phys. Commun.* 185.12 (2014), pp. 3430–3440.
- [95] Sebastian Keller et al. “An efficient matrix product operator representation of the quantum chemical Hamiltonian”. *J. Chem. Phys.* 143.24 (2015), p. 244118.
- [96] Zeph Landau, Umesh Vazirani, and Thomas Vidick. “A polynomial time algorithm for the ground state of one-dimensional gapped local Hamiltonians”. *Nat. Phys.* 11.7 (2015), pp. 566–569.

-
- [97] Roman Orus and Guifre Vidal. “Infinite time-evolving block decimation algorithm beyond unitary evolution”. *Phys. Rev. B* 78.15 (2008), p. 155117.
- [98] Lukasz Cincio and Guifré Vidal. “Characterizing topological order by studying the ground states on an infinite cylinder”. *Phys. Rev. Lett.* 110.6 (2013), p. 067208.
- [99] Norbert Schuch et al. “Computational complexity of projected entangled pair states”. *Phys. Rev. Lett.* 98.14 (2007), p. 140506.
- [100] M Schwarz, O Buerschaper, and J Eisert. “Approximating local observables on projected entangled pair states”. *Phys. Rev. A* 95.6 (2017), p. 060102.
- [101] Wei Li, Jan von Delft, and Tao Xiang. “Efficient simulation of infinite tree tensor network states on the Bethe lattice”. *Phys. Rev. B* 86.19 (2012), p. 195137.
- [102] HJ Liao et al. “Heisenberg antiferromagnet on the Husimi lattice”. *Phys. Rev. B* 93.7 (2016), p. 075154.
- [103] Jacob C. Bridgeman and Christopher T. Chubb. “Hand-waving and interpretive dance: An introductory course on tensor networks” (2016). arXiv: [1603.03039](https://arxiv.org/abs/1603.03039).
- [104] Piotr Czarnik, Lukasz Cincio, and Jacek Dziarmaga. “Projected entangled pair states at finite temperature: Imaginary time evolution with ancillas”. *Phys. Rev. B* 86.24 (2012), p. 245101.
- [105] Piotr Czarnik and Jacek Dziarmaga. “Variational approach to projected entangled pair states at finite temperature”. *Phys. Rev. B* 92.3 (2015), p. 035152.
- [106] Jacob Jordan et al. “Classical simulation of infinite-size quantum lattice systems in two spatial dimensions”. *Phys. Rev. Lett.* 101.25 (2008), p. 250602.
- [107] Philippe Corboz, T.M. Rice, and Matthias Troyer. “Competing states in the t-J model: uniform d-wave state versus stripe state”. *Phys. Rev. Lett.* 113 (2014), p. 046402.
- [108] Masuo Suzuki. “Decomposition formulas of exponential operators and Lie exponentials with some applications to quantum mechanics and statistical physics”. *J. Math. Phys.* 26.4 (1985), pp. 601–612.
- [109] HC Jiang, ZY Weng, and T Xiang. “Accurate determination of tensor network state of quantum lattice models in two dimensions”. *Phys. Rev. Lett.* 101.9 (2008), p. 090603.
- [110] Frank Verstraete, Valentin Murg, and J Ignacio Cirac. “Matrix product states, projected entangled pair states, and variational renormalization group methods for quantum spin systems”. *Adv. Phys.* 57.2 (2008), pp. 143–224.
- [111] Michael Lubasch, J Ignacio Cirac, and Mari-Carmen Banuls. “Algorithms for finite projected entangled pair states”. *Phys. Rev. B* 90.6 (2014), p. 064425.

- [112] Michael Lubasch, J Ignacio Cirac, and Mari-Carmen Bañuls. “Unifying projected entangled pair state contractions”. *New J. Phys.* 16.3 (2014), p. 033014.
- [113] Philippe Corboz. “Variational optimization with infinite projected entangled-pair states”. *Phys. Rev. B* 94.3 (2016), p. 035133.
- [114] Laurens Vanderstraeten et al. “Gradient methods for variational optimization of projected entangled-pair states”. *Phys. Rev. B* 94.15 (2016), p. 155123.
- [115] Guifré Vidal. “Class of quantum many-body states that can be efficiently simulated”. *Phys. Rev. Lett.* 101.11 (2008), p. 110501.
- [116] Glen Evenbly and Guifre Vidal. “Quantum criticality with the multi-scale entanglement renormalization ansatz”. *Strongly Correlated Systems*. Springer, 2013, pp. 99–130.
- [117] Glen Evenbly and Guifré Vidal. “Tensor network states and geometry”. *J. Stat. Phys.* 145.4 (2011), pp. 891–918.
- [118] G Evenbly et al. “Boundary quantum critical phenomena with entanglement renormalization”. *Phys. Rev. B* 82.16 (2010), p. 161107.
- [119] G Evenbly, P Corboz, and G Vidal. “Nonlocal scaling operators with entanglement renormalization”. *Phys. Rev. B* 82.13 (2010), p. 132411.
- [120] Jun John Sakurai and Eugene D Commins. *Modern quantum mechanics, revised edition*. 1995.
- [121] Florian Scheck. *Quantum Physics*. Springer, 2007.
- [122] John F Cornwell. *Group theory in physics: An introduction*. Vol. 1. Academic press, 1997.
- [123] Sukhwinder Singh, Robert NC Pfeifer, and Guifré Vidal. “Tensor network decompositions in the presence of a global symmetry”. *Phys. Rev. A* 82.5 (2010), p. 050301.
- [124] Sukhwinder Singh and Guifre Vidal. “Tensor network states and algorithms in the presence of a global SU (2) symmetry”. *Phys. Rev. B* 86.19 (2012), p. 195114.
- [125] Sukhwinder Singh, Robert NC Pfeifer, and Guifre Vidal. “Tensor network states and algorithms in the presence of a global U (1) symmetry”. *Phys. Rev. B* 83.11 (2011), p. 115125.
- [126] Thorsten B Wahl et al. “Symmetries and boundary theories for chiral projected entangled pair states”. *Phys. Rev. B* 90.11 (2014), p. 115133.
- [127] Shuo Yang et al. “Chiral projected entangled-pair state with topological order”. *Phys. Rev. Lett.* 114.10 (2015), p. 106803.
- [128] Didier Poilblanc, J Ignacio Cirac, and Norbert Schuch. “Chiral topological spin liquids with projected entangled pair states”. *Phys. Rev. B* 91.22 (2015), p. 224431.

-
- [129] Didier Poilblanc, Norbert Schuch, and Ian Affleck. “SU (2) 1 chiral edge modes of a critical spin liquid”. *Phys. Rev. B* 93.17 (2016), p. 174414.
- [130] Carlos Fernández-González et al. “Constructing topological models by symmetrization: A projected entangled pair states study”. *Phys. Rev. B* 94.15 (2016), p. 155106.
- [131] Philippe Corboz et al. “Simulation of interacting fermions with entanglement renormalization”. *Phys. Rev. A* 81.1 (2010), p. 010303.
- [132] Philippe Corboz, Jacob Jordan, and Guifré Vidal. “Simulation of fermionic lattice models in two dimensions with projected entangled-pair states: Next-nearest neighbor Hamiltonians”. *Phys. Rev. B* 82.24 (2010), p. 245119.
- [133] Philippe Corboz et al. “Simulation of strongly correlated fermions in two spatial dimensions with fermionic projected entangled-pair states”. *Phys. Rev. B* 81.16 (2010), p. 165104.
- [134] Christina V Kraus et al. “Fermionic projected entangled pair states”. *Phys. Rev. A* 81.5 (2010), p. 052338.
- [135] Philippe Corboz et al. “Stripes in the two-dimensional t-J model with infinite projected entangled-pair states”. *Phys. Rev. B* 84.4 (2011), p. 041108.
- [136] Philippe Corboz. “Improved energy extrapolation with infinite projected entangled-pair states applied to the two-dimensional Hubbard model”. *Phys. Rev. B* 93.4 (2016), p. 045116.
- [137] G Evenbly and G Vidal. “Entanglement renormalization in noninteracting fermionic systems”. *Phys. Rev. B* 81.23 (2010), p. 235102.
- [138] Piotr Czarnik and Jacek Dziarmaga. “Fermionic projected entangled pair states at finite temperature”. *Phys. Rev. B* 90.3 (2014), p. 035144.
- [139] Juan Osorio Iregui, Matthias Troyer, and Philippe Corboz. “Infinite matrix product states versus infinite projected entangled-pair states on the cylinder: A comparative study”. *Phys. Rev. B* 96.11 (2017), p. 115113.
- [140] Richard P Feynman. “Simulating physics with computers”. *Int. J. Theor. Phys.* 21.6 (1982), pp. 467–488.
- [141] Frank Wilczek. “Magnetic flux, angular momentum, and statistics”. *Phys. Rev. Lett.* 48.17 (1982), p. 1144.
- [142] Frank Wilczek. “Remarks on dyons”. *Phys. Rev. Lett.* 48.17 (1982), p. 1146.
- [143] Gregory Moore and Nathan Seiberg. “Classical and quantum conformal field theory”. *Commun. Math. Phys.* 123.2 (1989), pp. 177–254.
- [144] Edward Witten. “Quantum field theory and the Jones polynomial”. *Commun. Math. Phys.* 121.3 (1989), pp. 351–399.
- [145] Klaus Fredenhagen, Karl-Henning Rehren, and Bert Schroer. “Superselection sectors with braid group statistics and exchange algebras”. *Commun. Math. Phys.* 125.2 (1989), pp. 201–226.

- [146] Jürg Fröhlich and Fabrizio Gabbiani. “Braid statistics in local quantum theory”. *Rev. Math. Phys.* 2.03 (1990), pp. 251–353.
- [147] Elliott Lieb, Theodore Schultz, and Daniel Mattis. “Two soluble models of an antiferromagnetic chain”. *Ann. Phys.* 16.3 (1961), pp. 407–466.
- [148] Masaki Oshikawa. “Commensurability, excitation gap, and topology in quantum many-particle systems on a periodic lattice”. *Phys. Rev. Lett.* 84.7 (2000), p. 1535.
- [149] Matthew B Hastings. “Lieb-Schultz-Mattis in higher dimensions”. *Phys. Rev. B* 69.10 (2004), p. 104431.
- [150] G Jackeli and G Khaliullin. “Mott insulators in the strong spin-orbit coupling limit: From Heisenberg to a quantum compass and Kitaev models”. *Phys. Rev. Lett.* 102.1 (2009), p. 017205.
- [151] Juan Osorio Iregui, Philippe Corboz, and Matthias Troyer. “Probing the stability of the spin-liquid phases in the Kitaev-Heisenberg model using tensor network algorithms”. *Phys. Rev. B* 90.19 (2014), p. 195102.
- [152] G Baskaran, Diptiman Sen, and R Shankar. “Spin-S Kitaev model: Classical ground states, order from disorder, and exact correlation functions”. *Phys. Rev. B* 78.11 (2008), p. 115116.
- [153] G Baskaran, Saptarshi Mandal, and R Shankar. “Exact results for spin dynamics and fractionalization in the Kitaev model”. *Phys. Rev. Lett.* 98.24 (2007), p. 247201.
- [154] Han-Dong Chen and Zohar Nussinov. “Exact results of the Kitaev model on a hexagonal lattice: spin states, string and brane correlators, and anyonic excitations”. *J. Phys. A* 41.7 (2008), p. 075001.
- [155] Huan He et al. “Study Highly Frustrated Spin Systems with mixed PEPS in infinite honeycomb lattice” (2013). arXiv: [1303.2431](#).
- [156] Yogesh Singh and P Gegenwart. “Antiferromagnetic Mott insulating state in single crystals of the honeycomb lattice material Na_2IrO_3 ”. *Phys. Rev. B* 82.6 (2010), p. 064412.
- [157] X Liu et al. “Long-range magnetic ordering in Na_2IrO_3 ”. *Phys. Rev. B* 83.22 (2011), p. 220403.
- [158] SK Choi et al. “Spin waves and revised crystal structure of honeycomb iridate Na_2IrO_3 ”. *Phys. Rev. Lett.* 108.12 (2012), p. 127204.
- [159] Feng Ye et al. “Direct evidence of a zigzag spin-chain structure in the honeycomb lattice: A neutron and x-ray diffraction investigation of single-crystal Na_2IrO_3 ”. *Phys. Rev. B* 85.18 (2012), p. 180403.
- [160] Yogesh Singh et al. “Relevance of the Heisenberg-Kitaev model for the honeycomb lattice iridates A_2IrO_3 ”. *Phys. Rev. Lett.* 108.12 (2012), p. 127203.

-
- [161] Riccardo Comin et al. “ Na_2IrO_3 as a novel relativistic Mott insulator with a 340-meV gap”. *Phys. Rev. Lett.* 109.26 (2012), p. 266406.
- [162] Atsuo Shitade et al. “Quantum spin Hall effect in a transition metal oxide Na_2IrO_3 ”. *Phys. Rev. Lett.* 102.25 (2009), p. 256403.
- [163] Giniyat Khaliullin. “Orbital order and fluctuations in Mott insulators”. *Progress of Theoretical Physics Supplement* 160 (2005), pp. 155–202.
- [164] Junggho Kim et al. “Magnetic excitation spectra of Sr_2IrO_4 probed by resonant inelastic X-ray scattering: establishing links to cuprate superconductors”. *Phys. Rev. Lett.* 108.17 (2012), p. 177003.
- [165] Hlynur Gretarsson et al. “Crystal-field splitting and correlation effect on the electronic structure of A_2IrO_3 ”. *Phys. Rev. Lett.* 110.7 (2013), p. 076402.
- [166] J. Chaloupka, G. Jackeli, and G. Khaliullin. “Zigzag Magnetic Order in the Iridium Oxide Na_2IrO_3 ”. *Phys. Rev. Lett.* 110.9 (2013), p. 097204.
- [167] J. Chaloupka, G. Jackeli, and G. Khaliullin. “Kitaev-Heisenberg Model on a Honeycomb Lattice: Possible Exotic Phases in Iridium Oxides A_2IrO_3 ”. *Phys. Rev. Lett.* 105.2 (2010), p. 027204.
- [168] Robert Schaffer, Subhro Bhattacharjee, and Yong Baek Kim. “Quantum phase transition in Heisenberg-Kitaev model”. *Phys. Rev. B* 86.22 (2012), p. 224417.
- [169] Hong-Chen Jiang et al. “Possible proximity of the Mott insulating iridate Na_2IrO_3 to a topological phase: Phase diagram of the Heisenberg-Kitaev model in a magnetic field”. *Phys. Rev. B* 83.24 (2011), p. 245104.
- [170] Matthias Gohlke et al. “Dynamics of the Kitaev-Heisenberg Model” (2017). arXiv: [1701.04678](https://arxiv.org/abs/1701.04678).
- [171] L. Tagliacozzo et al. “Scaling of entanglement support for matrix product states”. *Phys. Rev. B* 78 (2008), p. 024410.
- [172] Frank Pollmann et al. “Theory of finite-entanglement scaling at one-dimensional quantum critical points”. *Phys. Rev. Lett.* 102.25 (2009), p. 255701.
- [173] B Pirvu et al. “Matrix product states for critical spin chains: Finite-size versus finite-entanglement scaling”. *Phys. Rev. B* 86.7 (2012), p. 075117.
- [174] Roger SK Mong et al. “Parafermionic conformal field theory on the lattice”. *J. Phys. A* 47.45 (2014), p. 452001.
- [175] Vid Stojevic et al. “Conformal data from finite entanglement scaling”. *Phys. Rev. B* 91.3 (2015), p. 035120.
- [176] Stefan Depenbrock, Ian P McCulloch, and Ulrich Schollwöck. “Nature of the spin-liquid ground state of the $s = 1/2$ Heisenberg model on the kagome lattice”. *Phys. Rev. Lett.* 109.6 (2012), p. 067201.
- [177] Fabian Kolley et al. “Phase diagram of the J_1 - J_2 Heisenberg model on the kagome lattice”. *Phys. Rev. B* 91.10 (2015), p. 104418.

- [178] Dániel Varjas, Michael P Zaletel, and Joel E Moore. “Chiral Luttinger liquids and a generalized Luttinger theorem in fractional quantum Hall edges via finite-entanglement scaling”. *Phys. Rev. B* 88.15 (2013), p. 155314.
- [179] Philippe Corboz et al. “Simultaneous Dimerization and SU(4) Symmetry Breaking of 4-Color Fermions on the Square Lattice”. *Phys. Rev. Lett.* 107.21 (2011), p. 215301.
- [180] Ling Wang et al. “Tensor-product state approach to spin- $\frac{1}{2}$ square J_1 - J_2 antiferromagnetic Heisenberg model: Evidence for deconfined quantum criticality”. *Phys. Rev. B* 94 (7 2016), p. 075143.
- [181] Philippe Corboz et al. “Spin-Orbital Quantum Liquid on the Honeycomb Lattice”. *Phys. Rev. X* 2.4 (2012), p. 041013.
- [182] Philippe Corboz and Frédéric Mila. “Tensor network study of the Shastry-Sutherland model in zero magnetic field”. *Phys. Rev. B* 87.11 (2013), p. 115144.
- [183] Z. Y. Xie et al. “Tensor Renormalization of Quantum Many-Body Systems Using Projected Entangled Simplex States”. *Phys. Rev. X* 4.1 (2014), p. 011025.
- [184] Philippe Corboz and Frédéric Mila. “Crystals of bound states in the magnetization plateaus of the Shastry-Sutherland model”. *Phys. Rev. Lett.* 112.14 (2014), p. 147203.
- [185] Thibaut Picot et al. “Spin- S kagome quantum antiferromagnets in a field with tensor networks”. *Phys. Rev. B* 93 (6 2016), p. 060407.
- [186] Thibaut Picot and Didier Poilblanc. “Nematic and supernematic phases in kagome quantum antiferromagnets under the influence of a magnetic field”. *Phys. Rev. B* 91.6 (2015), p. 064415.
- [187] Pierre Nataf et al. “Plaquette order in the SU(6) Heisenberg model on the honeycomb lattice”. *Phys. Rev. B* 93.20 (2016), p. 201113.
- [188] H. J. Liao et al. “Gapless Spin-Liquid Ground State in the $S=1/2$ Kagome Antiferromagnet”. *Phys. Rev. Lett.* 118.13 (2017), p. 137202.
- [189] Ido Niesen and Philippe Corboz. “Emergent Haldane phase in the $S = 1$ bilinear-biquadratic Heisenberg model on the square lattice”. *Phys. Rev. B* 95 (18 2017), p. 180404.
- [190] Shoudan Liang and Hanbin Pang. “Approximate diagonalization using the density matrix renormalization-group method: A two-dimensional-systems perspective”. *Phys. Rev. B* 49.13 (1994), p. 9214.
- [191] Sheng-Hao Li et al. “Tensor network states and ground-state fidelity for quantum spin ladders”. *Phys. Rev. B* 86.6 (2012), p. 064401.
- [192] Sheng-Hao Li et al. “Groundstate fidelity phase diagram of the fully anisotropic two-leg spin-1/2 XXZ ladder” (2017). arXiv: [1704.05484v1](https://arxiv.org/abs/1704.05484v1).

-
- [193] J Ignacio Cirac et al. “Entanglement spectrum and boundary theories with projected entangled-pair states”. *Phys. Rev. B* 83.24 (2011), p. 245134.
- [194] Norbert Schuch et al. “Topological order in the projected entangled-pair states formalism: Transfer operator and boundary hamiltonians”. *Phys. Rev. Lett.* 111.9 (2013), p. 090501.
- [195] Ling Wang, Iztok Piorn, and Frank Verstraete. “Monte Carlo simulation with tensor network states”. *Phys. Rev. B* 83.13 (2011), p. 134421.
- [196] Ling Wang et al. “Constructing a Gapless Spin-Liquid State for the Spin-1/2 J₁-J₂ Heisenberg Model on a Square Lattice”. *Phys. Rev. Lett.* 111.3 (2013), p. 037202.
- [197] RJ Elliott, P Pfeuty, and C Wood. “Ising model with a transverse field”. *Phys. Rev. Lett.* 25.7 (1970), p. 443.
- [198] P Pfeuty and RJ Elliott. “The Ising model with a transverse field. II. Ground state properties”. *J. Phys. Condens. Matter* 4.15 (1971), p. 2370.
- [199] Kazuo Hattori. “The Ising Model with a Transverse Field”. *J. Phys. Soc. Jpn.* 43.1 (1977), pp. 77–81.
- [200] KA Penson, R Jullien, and P Pfeuty. “Zero-temperature renormalization-group method for quantum systems. III. Ising model in a transverse field in two dimensions”. *Phys. Rev. B* 19.9 (1979), p. 4653.
- [201] MSL du Croo de Jongh and JMJ Van Leeuwen. “Critical behavior of the two-dimensional Ising model in a transverse field: A density-matrix renormalization calculation”. *Phys. Rev. B* 57.14 (1998), p. 8494.
- [202] Hong-Chen Jiang, Zhenghan Wang, and Leon Balents. “Identifying topological order by entanglement entropy” (2012). arXiv: [1205.4289](https://arxiv.org/abs/1205.4289).
- [203] Satoshi Nishimoto, Naokazu Shibata, and Chisa Hotta. “Controlling frustrated liquids and solids with an applied field in a kagome Heisenberg antiferromagnet”. *Nat. Commun.* (2013).
- [204] ZY Xie et al. “Tensor renormalization of quantum many-body systems using projected entangled simplex states”. *Phys. Rev. X* 4.1 (2014), p. 011025.
- [205] HJ Liao et al. “Gapless spin-liquid ground state in the S= 1/2 kagome antiferromagnet”. *Phys. Rev. Lett.* 118.13 (2017), p. 137202.
- [206] Anders W Sandvik, Adolfo Avella, and Ferdinando Mancini. “Computational studies of quantum spin systems”. *AIP Conf. Proc.* Vol. 1297. 1. AIP. 2010, pp. 135–338.
- [207] Elbio Dagotto. “Correlated electrons in high-temperature superconductors”. *Rev. Mod. Phys.* 66.3 (1994), p. 763.
- [208] Elliott H Lieb. “The Hubbard model: Some rigorous results and open problems”. *The Hubbard Model*. Springer, 1995, pp. 1–19.

- [209] Antoine Georges et al. “Dynamical mean-field theory of strongly correlated fermion systems and the limit of infinite dimensions”. *Rev. Mod. Phys.* 68.1 (1996), p. 13.
- [210] Elbio Dagotto and TM Rice. “Surprises on the way from one-to two-dimensional quantum magnets: the ladder materials”. *Science* 271.5249 (1996), pp. 618–623.
- [211] G Hager et al. “Stripe formation in doped Hubbard ladders”. *Phys. Rev. B* 71.7 (2005), p. 075108.
- [212] DJ Scalapino. “Numerical studies of the 2D Hubbard model”. *Handbook of High-Temperature Superconductivity*. Springer, 2007, pp. 495–526.
- [213] Olexei I. Motrunich and Matthew P. A. Fisher. “ d -wave correlated critical Bose liquids in two dimensions”. *Phys. Rev. B* 75 (23 2007), p. 235116.
- [214] Ryan V. Mishmash et al. “Bose metals and insulators on multileg ladders with ring exchange”. *Phys. Rev. B* 84 (24 2011), p. 245127.
- [215] G. Evenbly and G. Vidal. “Class of Highly Entangled Many-Body States that can be Efficiently Simulated”. *Phys. Rev. Lett.* 112 (24 2014), p. 240502.
- [216] Jeffrey G Rau, Eric Kin-Ho Lee, and Hae-Young Kee. “Generic spin model for the honeycomb iridates beyond the Kitaev limit”. *Phys. Rev. Lett.* 112.7 (2014), p. 077204.
- [217] Ioannis Rousochatzakis et al. “Phase Diagram and Quantum Order by Disorder in the Kitaev K_1 - K_2 Honeycomb Magnet”. *Phys. Rev. X* 5.4 (2015), p. 041035.
- [218] S-H Baek et al. “Observation of a Field-induced Quantum Spin Liquid in α - RuCl_3 ” (2017). arXiv: [1702.01671](https://arxiv.org/abs/1702.01671).
- [219] Jiacheng Zheng et al. “Gapless Spin Excitations in the Field-Induced Quantum Spin Liquid Phase of α - RuCl_3 ” (2017). arXiv: [1703.08474](https://arxiv.org/abs/1703.08474).

Acknowledgements

As I give this document the finishing touches, I can't help but reflect on the process involved in producing it. It is the result of 5 challenging years in which I was frequently forced to explore my limits not only intellectually but also personally.

I will start off by giving my most sincere thank you to my PhD advisor Matthias Troyer. As I first sent him my application letter I was fully aware that, having very little experience in the field, my chances were slim. He nevertheless decided to take the chance and give me the opportunity to join his group. This is something I most sincerely appreciate. I am also thankful for all the freedom he let me have when carrying out my research, as well as his patience and encouragement, even if things appeared to be coming to a halt at times. I believe these were important ingredients in my process of becoming an independent researcher.

I would also like to thank Manfred Sigrist, somebody I indirectly started learning from as a young undergrad in Colombia when I used some of his slides to prepare my graduation project. As destiny would have it, I would end up having the great opportunity of doing my master's thesis under his supervision. To this day I am convinced that Manfred's input was a key factor in being accepted as a PhD student by Matthias. His passion for science is also something I have always found very inspiring.

Just as important was Philippe Corboz who patiently and kindly guided me during the difficult start intrinsic to working with tensor network algorithms. His contributions were essential in getting me started and even in our latest collaboration I felt like I was permanently learning from his extensive knowledge in the field. His input also played an important role in my visit to Perimeter Institute. Most importantly, I can definitely say that working with him throughout the years has definitely been quite fun.

I also can't let go of the opportunity to thank Guifré Vidal for hosting my visit at Perimeter Institute. Those months were some of the most exciting ones of my PhD and it is because of him that I came into contact with the world of CFTs. Keeping up with his seemingly endless list of ideas was hard work but also really inspiring and fun. Gràcies per tot!

To all the members of the computational physics group, I can hardly thank you enough. Michele, my longest officemate, who repeatedly and patiently shared with me all of his programming experience. Andreas (and Michele!) who patiently allowed me to drag them into discussions about HPC in the hopes of getting every bit of their knowledge out. Jakub for providing all his input during my early C++ years and sharing all of his cool experiences in the great outdoors. Ilia for adding an edge to science and keeping it real. Alexey for being an endless source of fun discussions (scientific and otherwise) and providing a remarkable example of determination. Kiryl for all the entertaining discussions and showing how extreme sports and science can go hand in hand. Ethan for being so chill. Jana and Medha for a lot of fun and interesting discussions and adding a sporty side to our office. Evert for the endless discussions during our joint TA'ing experiences. Jan for being a great officemate and providing the basic template for the thesis. Giuseppe for the really entertaining discussions. Georg, Guglielmo, Dominik, Donjan, Bettina, Mario, Daniel, Damian, Thomas, Juan, Julian, Andres, Markus, etc, thank you for all the great experiences!

Meine liebe Rike, nur du weisst, was dies alle bedeutet. Dafür, dass du mich durch Alles begleitet hast, kann ich dir nicht genug danken. Das hier ist auch dein Verdienst. Ich danke dir unendlich mal unendlich!

Finalmente, a mi familia quisiera agradecerle por brindarme una de las herramientas más valiosas: el ejemplo. Sin ustedes nunca habría encontrado un camino a seguir, y cualquier camino que hubiese escogido hubiese sido terriblemente aburrido. Este logro fué posible gracias a sus enseñanzas, su cariño y su permanente apoyo. Este logro les pertenece a ustedes tanto como a mi. Ma, Pa, y Dudu, (y muñeca!) infinitas gracias!

Curriculum Vitae

Personal data

Name: Juan Camilo Osorio Iregui
Date of birth: 14.02.1985
Place of birth: Barranquilla, Colombia
Nationality: Colombian

Education

2012 (Jun) – 2017 (Aug) Ph.D. Physics (ETH Zurich, Switzerland)
Computational Physics Group (Prof. M. Troyer)
2011 (Feb) – 2011 (May) M.Sc. Thesis (ETH Zurich, Switzerland)
Institute for Theoretical Physics (Prof. M. Sigrist)
2009 (Sep) – 2011 (May) M.Sc. Physics (ETH Zurich, Switzerland)
2004 (Sep) – 2008 (Dec) B.Sc. Physics (Universidad de los Andes, Colombia)

Employment

2012 – 2017 Teaching Assistant (ETH Zurich, Switzerland)
Institute for Theoretical Physics
2011 – 2012 Research Assistant (Max F. Perutz Laboratory, Austria)
Computational Biophysics Group (Prof. Bojan Zagrovic)
2009 Teaching Assistant (Universidad de los Andes, Colombia)

List of publications

- [1] Juan Osorio Iregui, Matthias Troyer, and Philippe Corboz. “Infinite matrix product states versus infinite projected entangled-pair states on the cylinder: A comparative study”. *Phys. Rev. B* 96.11 (2017), p. 115113.
- [2] Matea Hajnic, Juan Osorio Iregui, and Bojan Zagrovic. “Interaction preferences between nucleobase mimetics and amino acids in aqueous solutions”. *Phys. Chem. Chem. Phys.* 17.33 (2015), pp. 21414–21422.
- [3] Matea Hajnic, Juan Osorio Iregui, and Bojan Zagrovic. “Computational analysis of amino acids and their sidechain analogs in crowded solutions of RNA nucleobases with implications for the mRNA–protein complementarity hypothesis”. *Nucleic Acids Res.* 42.21 (2014), pp. 12984–12994.
- [4] Juan Osorio Iregui, Philippe Corboz, and Matthias Troyer. “Probing the stability of the spin-liquid phases in the Kitaev-Heisenberg model using tensor network algorithms”. *Phys. Rev. B* 90.19 (2014), p. 195102.
- [5] Juan Osorio Iregui. “Transport properties of a Rashba metal”. MA thesis. ETH Zürich, 2011.